ABSTRACT

Title of dissertation: PREDICTING FIRE SPRINKLER SPRAYS

Taylor Myers, Doctor of Philosophy, 2018

Dissertation directed by: Professor Andre Marshall
Department of Mechanical Engineering

Accurate representation of fire sprinkler spray enables quantitative engineering analysis of fire suppression performance. Increasingly, fire sprinkler systems are evaluated using computer fire models in which sprinkler spray is simulated with Lagrangian particles. However, limited guidance exists as to how to predict the formation of complex, spatio-stochastic fire sprinkler spray or how to accurately represent the dispersion of spray in terms of Lagrangian particles. The current work predicts the fire sprinkler spray generated by a canonical axisymmetric sprinkler using a Deflection Atomization Dispersion (DAD) framework, developed as a predictive modeling approach generalizable to typical fire sprinklers. In a DAD framework, spray evolution is divided into three stages: deflection of the water jet by the sprinkler deflector, atomization of the resulting thin fluid sheets into an initial spray, and dispersion of the initial spray into far-field spray. Deflection is described as a free-surface flow and is modeled deterministically using a boundary integral method (BIM). Atomization

of the deflected fluid sheet is described by linear-stability theory to develop scaling laws relating sheet characteristics to statistically distributed, spatially resolved initial spray characteristics including breakup radius, volume flux, drop size, and drop velocity. The resulting initial spray is then described by a multivariate probability distribution function that varies over the predicted initialization surface. This function is stochastically sampled to generate Lagrangian particles representative of the near-field spray and the dispersion of these Lagrangian particles is in turn simulated in FireFOAM (an open source computational fluid dynamics fire model) to predict the far-field spray. Modeled results are compared to highly resolved near- and far-field measurements of axisymmetric sprinkler sprays generated by the Spatially-Resolved Spray Scanning System (4S). The end results shows agreement across all three stages of modeling with less than 10% error when compared to experimental measurements. Further, the newly implemented model shows a stronger ability to capture spray induced airflow when compared to a baseline model. This work is the first to predict sprinkler spray dispersion entirely from sprinkler deflector geometry and operating pressure.

PREDICTING FIRE SPRINKLER SPRAYS

by

Taylor Myers

Dissertation submitted to the Faculty of the Graduate School of the
University of Maryland, College Park in partial fulfillment
of the requirements for the degree of
Doctor of Philosophy
2018

Advisory Committee:
Professor Andre Marshall, Chair/Advisor
Professor Arnaud Trouvé
Professor Peter Sunderland
Professor Stanislav Stoliarov
Professor Michael Gollner
Professor Kenneth Yu
Dr. Hong-Zeng Yu

Dedication

To my wife, Lindsay, and to my daughters, Elizabeth and Mary.

Acknowledgments

I would like to acknowledge the contributions of all who made this research possible. First, I would like to thank the sponsoring organizations, NSF, FM Global and UTRC. Next, I am deeply indebted to several members of the FM Global team for their guidance, namely Drs. Karl Meredith, Ning Ren, Yi Wang, and Bert Yu. Your advice and cooperation has allowed this work to grow into what it has now become. I would also like to thank the Fire Protection Engineering department, which has been my home over the last eight years. I would like to thank my friends and peers, particularly Eric Link, Stephen Jordan, James White, and Sebastian Vilfayeu, who worked alongside me on this project. I would like to acknowledge my committee and Prof. Howard Baum, who have provided invaluable advice and guidance. Lastly, I would like to thank Prof. Andre Marshall, for embracing my ideas and encouraging me to become what he believed I could become.

Contents

List of Tables

List of Figures

Chapter 1: Introduction

1.1 Study overview

The goal of this work is to predict the far-field spray of a fire sprinkler entirely from sprinkler geometry and injection pressure. A physics inspired, rigorous framework was developed to harmonize measurements, models, and analyses. This Deflection Atomization Dispersion (DAD) framework is a comprehensive, three-part model for predicting fire sprinkler sprays.

In the DAD framework, the evolution of fire sprinkler spray is divided into three stages: (1) deflection of the water jet by the sprinkler deflector to form thin fluid sheets, (2) atomization of the sheets into an initial or near-field spray, and (3) dispersion of the initial spray into far-field spray, as shown in Fig. 1.1. Each stage is presented as a separate modular model within the framework because each stage requires a different predictive modeling approach. The DAD framework identifies appropriate boundary conditions for each modeling phase along with modeling requirements to predict the spray in a continuous stream from injection through ultimate

dispersion. These boundary conditions and models were developed and assembled to completely predict the spray from two canonical sprinklers and validated against detailed experimental measurements made during all three stages of spray evolution. These models are readily incorporated into high fidelity computational fluid dynamics (CFD) fire models such as FM Global's FireFOAM.

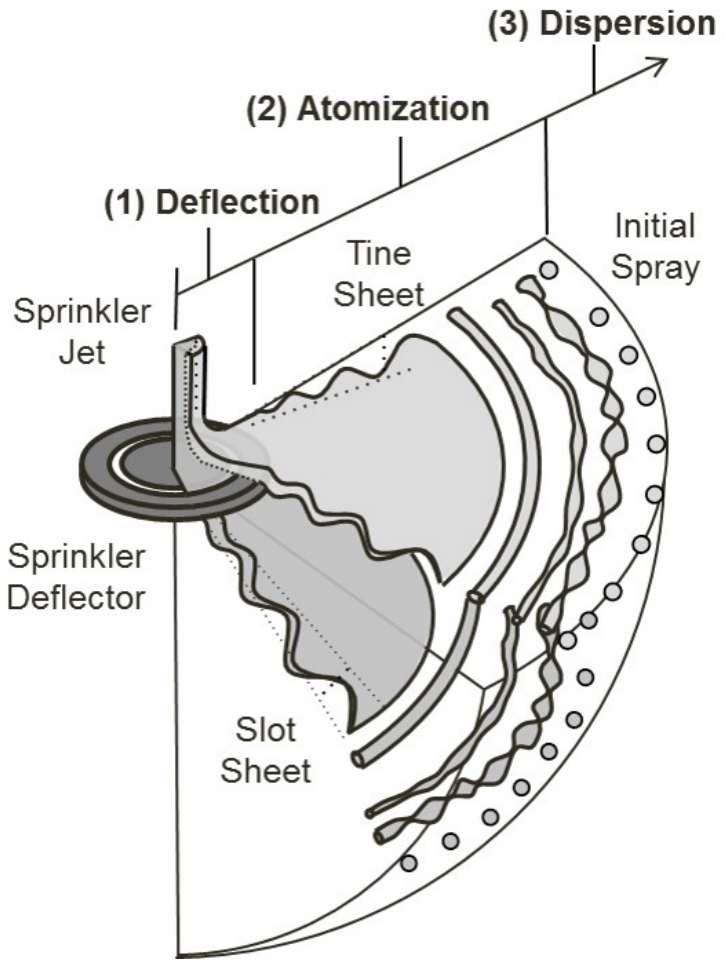

Figure 1.1: The predicted evolution of fire sprinkler spray can be divided into three stages: (1) deflection, (2) atomization, and (3) dispersion.

1.2 Motivation

Fire sprinklers provide a simple and cost-effective spray dispersion method to arrest fire growth [1] and are a critical component of many fire protection systems. Accurately predicting fire sprinkler sprays is essential to advancing the design of these systems.

A typical pendent sprinkler, as seen in Fig. 1.2, consists of a thermal activation element and a collection of spray shaping elements (the orifice, frame arms, boss, and deflector). On activation, a water jet emerging from the orifice strikes the frame arms, boss, and deflector, and the jet is deflected into a complex series of cascading sheets, jets, and drops, as shown in Fig. 1.3 [2]. The sheets and jets move outward, away from the sprinkler, and interact with the surrounding air; as a result of aerodynamic instabilities, the water from these sheets eventually undergoes atomization, breaking into drops. These drops form a dilute spray that flies outward, dispersing through combustion products, plume, flame, and reactants, eventually interacting with surfaces.

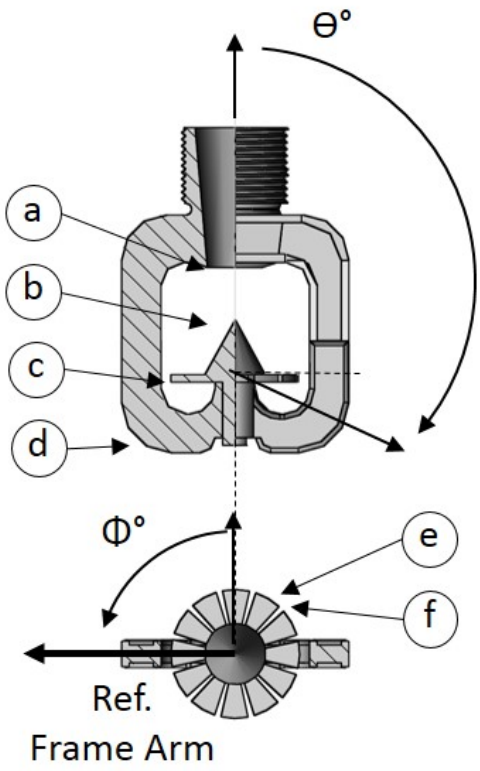

Figure 1.2: Partial cross section of a typical pendent sprinkler consisting of (a) orifice, (b) boss, (c) deflector, and (d) frame arms; detail from the deflector shows (e) the tines and (f) the slots [3].

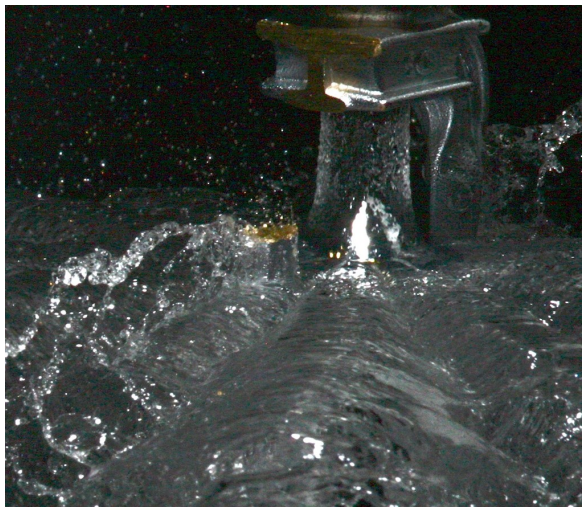

Figure 1.3: Sprinkler jet exiting the orifice and interacting with the frame arms, boss, and deflector to form sheets, jets, and drops [4].

When the initial water jet undergoes both the deflection and the atomization processes, a highly non-uniform spray is produced, consistent with the measurements presented by Sheppard [5, 6]. Characteristics of this atomized spray in turn affect spray dispersion. Recent work by Ren et al. [7] introduces a method that characterizes measurements of the near-field fire sprinkler spray in support of numerical simulation of sprinkler spray dispersion. The measurements in Ref. [7] reveal large spatial variations in the near-field volume flux, drop size, and velocity corresponding to the geometric features of the fire sprinkler head. A typical example of these spatial variations is seen in Fig. 1.4, which shows a measurement of the near-field volume flux of a typical, pendent-type sprinkler head produced in the University of Maryland's spray lab with the Spatially-resolved Spray Scanning System (4S) [3].

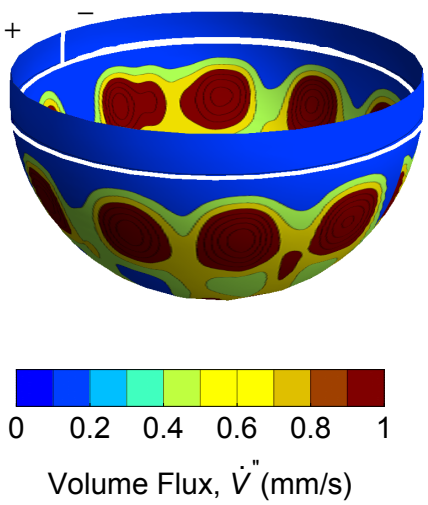

Figure 1.4: The highly non-uniform volume flux of a typical pendent-type sprinkler head, measured at a radius of 0.4 m from the sprinkler head [3].

Increasingly, computational fluid dynamics (CFD) fire models, like the Fire Dynamics Simulator (FDS) and FireFOAM, are used to inform fire protection decisions [8, 9]. In order to provide high fidelity fire protection analysis, these models must capture the highly non-uniform sprinkler spray. Both FDS and FireFOAM use a Eulerian-Lagrangian (EL) approach to describe multiphase flows. In the EL approach, the continuous phase (i.e., the gas phase, including combustion products, plume, flame, and reactants) is represented as an evolving Eulerian field, while the dispersed phase (i.e., the sprinkler spray) is modeled using Lagrangian particle tracking [10]. In these models, Lagrangian particles, which are used to represent the sprinkler spray, are injected into the modeled domain. Particle motion is determined by solving the Lagrangian equations of motion and interaction while the Eulerian

continuous phase is handled through a variety of sub-models (e.g., heat transfer, drop evaporation, turbulent dispersion, etc.).

Limited guidance exists as to how the complex, spatio-stochastic characteristics of the initial fire sprinkler spray can be represented in terms of these Lagrangian particles. Modeling is further complicated by the limited ability of current fire models to predict fire sprinkler deflection or atomization [11]. The Lagrangian particle methods for spray dispersion are very accurate, but highly dependent on initial spray characteristics, necessitating accurate specification of the initial spray either through high-fidelity measurements or through detailed deflection and atomization models.

The lack of an existing comprehensive model for predicting the fire sprinkler spray from sprinkler geometry and injection conditions limits the predictive abilities of the high fidelity CFD fire models used to analyze the effectiveness of fire sprinklers. In turn, the absence of accurate spray modeling in CFD fire models restricts the ability of fire protection engineers to creatively incorporate valuable predictive information in the development process for new sprinkler models, something that would lead to more effective and efficient sprinkler design. The success of fire suppression is sensitive to the form of the spray used for suppression [1]. Better designed sprinkler spray nozzles could result in sprinkler systems capable of more reliably suppressing fires with less inadvertent property damage.

Development of a comprehensive predictive fire sprinkler spray model could

provide a method to accurately incorporate spray within existing high fidelity fire models. Further, a model of this type could provide the means to rapidly and inexpensively explore different sprinkler geometries and their impacts on sprinkler spray, facilitating faster design testing than is possible when relying on expensive physical tests. Thus, the development of a predictive model of fire sprinkler spray evolution will have far-reaching implications for the advancement of suppression technology and fire protection practices.

1.3 Approach

The complex physical phenomena that govern sprinkler spray formation and transport make the development of a single model for complete spray prediction nearly impossible. Each phase has different dominant forces, desired model outputs, and length scales that differ by several orders of magnitude. For example, the millimeter length scales appropriate for measuring a water jet interacting with the deflector dwarf the micrometer length scales appropriate to describing sheet atomization, limiting the ability of a model to capture both in an efficient and accurate manner. The deflection of the water jet is in turn dwarfed by the meter length scales associated with spray transport, and typical techniques for handling the unknown liquid-air interface on the deflector become impractical when applied to tens of millions of individual drops. As a result, a modular approach is used in this study, in which each phase is handled

with a different model but connected to the other phases through shared outputs and inputs.

Figure 1.5 provides a flowchart outlining the DAD framework developed in this work. In the DAD framework, the fire sprinkler spray is decomposed into three physical phases: (1) deflection, (2) atomization, and (3) dispersion, as illustrated in Fig. 1.1. In each stage, the developed model takes measured or predicted inputs then generates predictions which serve as the inputs for subsequent model stages. The deflection model uses sprinkler characteristics (geometry and operating pressure) as its inputs and produces sheet characteristics (thickness and velocity) as its outputs. These sheet characteristics in turn provide the inputs for the atomization model, which produces initial spray characteristics as its outputs. These initial spray characteristics then serve as inputs for the spray dispersion model, which predicts far-field spray and gas phase characteristics.

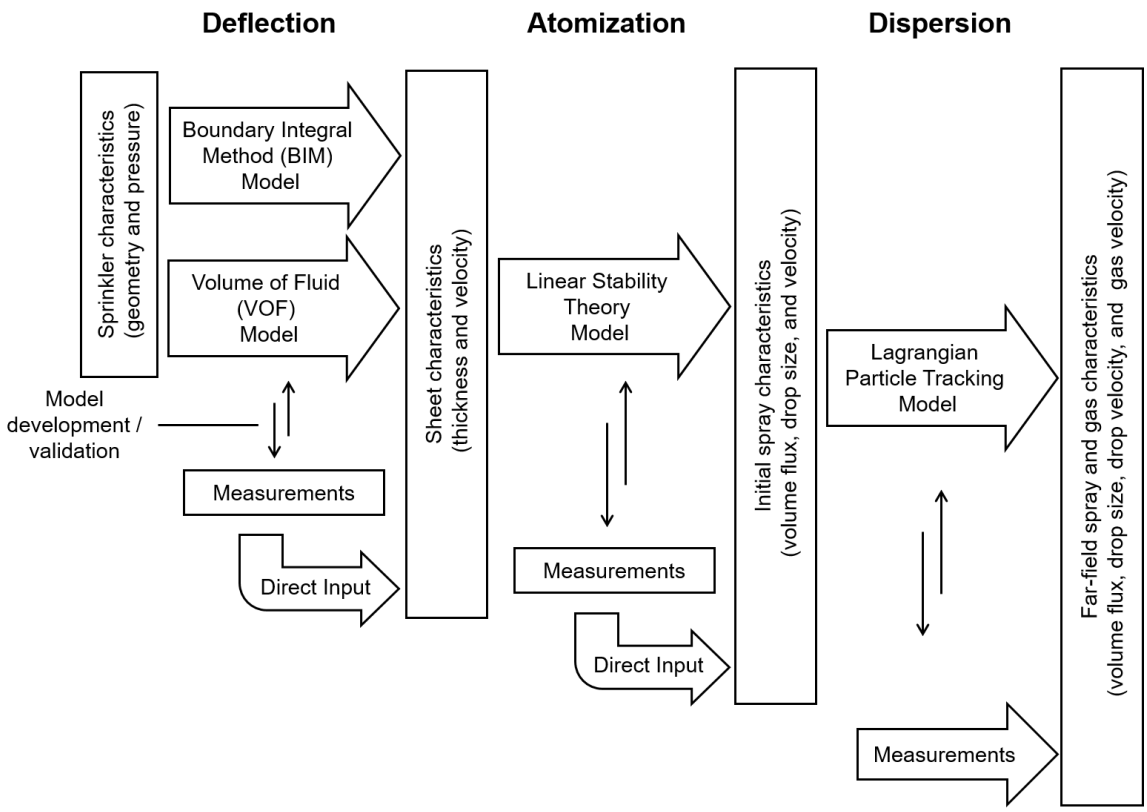

Figure 1.5: The Deflection Atomization Dispersion (DAD) framework is a physics inspired, rigorous framework developed to harmonize measurements, models, and analyses. The framework divides sprinkler spray evolution into a series of three models joined by well defined boundary conditions to allow continuous prediction of the spray from injection to the far-field.

The outputs of each stage of the framework can be reliably compared to, or replaced by, experimental measurements. This approach provides opportunities to develop and validate each stage's model individually. In future work, any particular stage of the framework may be bypassed completely, and boundary conditions provided through experimental measurements.

The physics and the models explored in this study are developed generally,

but applied explicitly to examine axisymmetric sprinklers. The complex workings of a real fire sprinkler obscure the impact of the essential geometric features used in their construction. By assuming that the flow pattern is axially symmetric, some of the geometric effects induced by the specific deflector plate geometry are lost, but the impact of the general sprinkler geometry responsible for uniform distribution of water around the sprinkler head is preserved. The axisymmetric case explored in this study effectively illustrates the impact of essential geometric details of the sprinkler on the flow while simplifying model implementation.

An axisymmetric sprinkler, as seen in Fig. 1.6, is described as follows: an inviscid, vertical jet with radius, R_j, and downward velocity, U_j, impinges on a horizontal deflector plate with diameter, R_d. A ring opening with centroid, R_s, and total area, A_s, is located in the deflector plate. Here deflector radius, R_d, and slot centroid, R_s, are non-dimensionalized by the impinging jet radius, R_j, and slot area A_s is non-dimensionalized by jet area, πR_j^2. The non-dimensional slot width, ΔR, is then provided as $\Delta R = A_s/2R_s$.

In a typical sprinkler head, slot penetrations in the deflector plate have some angular dependence, as seen in Fig. 1.2. In the axisymmetric sprinkler, the discrete openings in the deflector plate are 'smeared' out uniformly with respect to the azimuthal angle ϕ and so can be characterized entirely by radius and area.

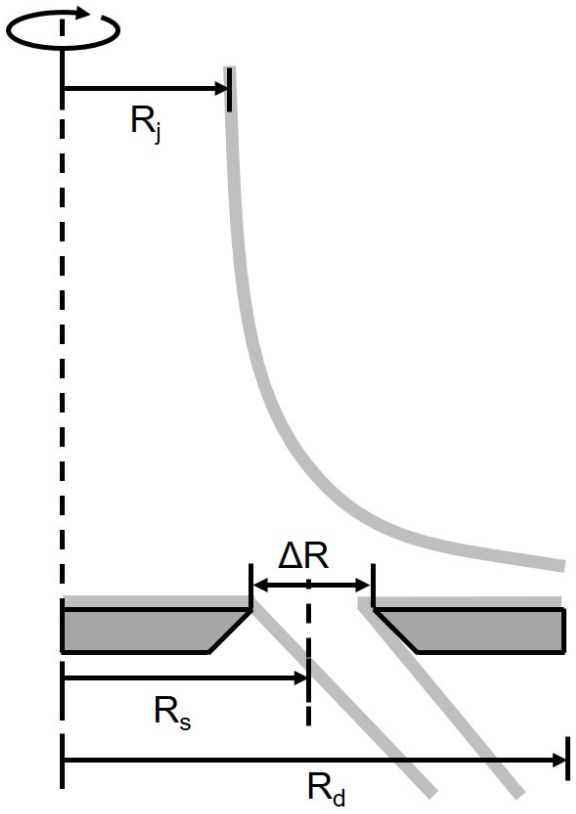

Figure 1.6: An axisymmetric sprinkler cross section (also shown in Fig. 1.7) consisting of a fluid jet of radius, R_j, impinging on a normal circular deflector plate with radius, R_d, containing a single slot with centroid radius, R_s, and total area, A_s.

Two specific axisymmetric sprinkler configurations are studied in this work: the first is a basis nozzle and the second is a two-stream axisymmetric sprinkler. Both sprinklers have a jet radius of 5.2 mm, K-factor of 80.6 $\mathrm{l/min \cdot bar^{1/2}}$, and a non-dimensional deflector radius, $R_d = 2.3$ (12 mm). The basis nozzle has no slot penetration, so all of the water is deflected by the deflector and forms a single sheet. The two-stream axisymmetric sprinkler has a single ring slot with a non-

dimensional slot radius, $R_s = 0.96$ (5 mm), and a non-dimensional slot area, $A_s = 0.92$ (25 mm^2), yielding a non-dimensional slot width, $\Delta R = 0.48$ (2.5 mm). This sprinkler was designed so that approximately 50% of the total water flows through the slot. Both sprinklers were operated at pressures of 1, 2, and 3 bar, yielding inviscid jet velocities, $U_j = 14$, 20, and 24 m/s, and approximate flow rates (based on K-factors) of 80.6 l/min, 114 l/min, and 140 l/min, respectively.

A single experimental sprinkler was constructed to mimic both of the sprinkler configurations described above. This sprinkler is made from a modified D3 spray nozzle where the deflector has been replaced by an axisymmetric deflector, as seen in Fig. 1.7. The circular deflector plate used has a ring slot spanning 120° of the circle. In this way, one quadrant of the sprinkler can be assumed to represent the basis nozzle, as described above, and the other to represents the-two stream axisymmetric sprinkler. For the purpose of this research, the effects of frame arms were neglected, and all measurements were made at a distance from the frame arms.

Measurements of the the two-sided experimental axisymmetric sprinkler were performed with the Spatially-resolved Spray Scanning System (4S) as shown in Fig. 1.8. The 4S provides three primary spray characterizations, as shown in Fig. 1.9, by rotating a sprinkler (1) through a series of diagnostics to provide a 360° [3]. First, mechanical sphere patternation (2) provides a spatially resolved map of near-field volume flux on a hemispheric area surrounding the sprinkler. Second, optical measurements using

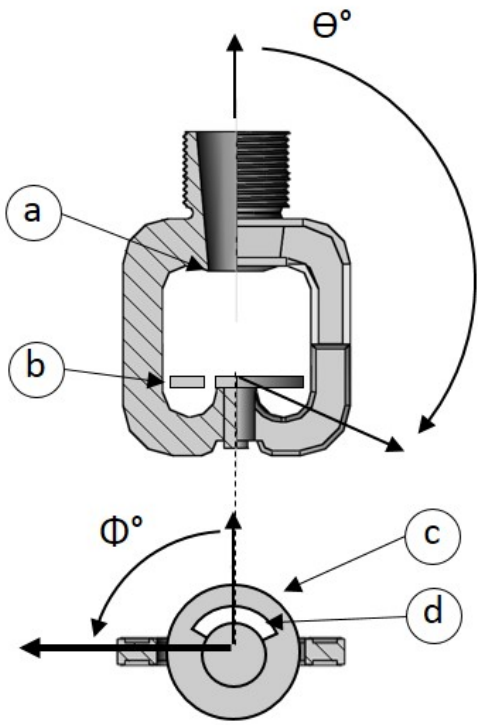

Figure 1.7: Partial cross-section of the sprinkler constructed to represent both axisymmetric configurations consisting of (a) orifice and (b) deflector, with (c) circular deflector plate and (d) ring slot spanning 120°.

a shadowgraphy system (3) provide information on drop size, velocity, and atomization location in the near-field spray. Lastly, integral line patternation (4) provides far-field measurements of spray volume flux in quiescent conditions. Taken together, these quantities provide a complete, spatially-resolved characterization of the initial sprinkler spray, suitable for CFD initialization and models developed herein. Further, far-field line patternation measurements of quiescent spray dispersion provide a source of comparison to high fidelity models.

The development of the DAD framework represents a significant advance over

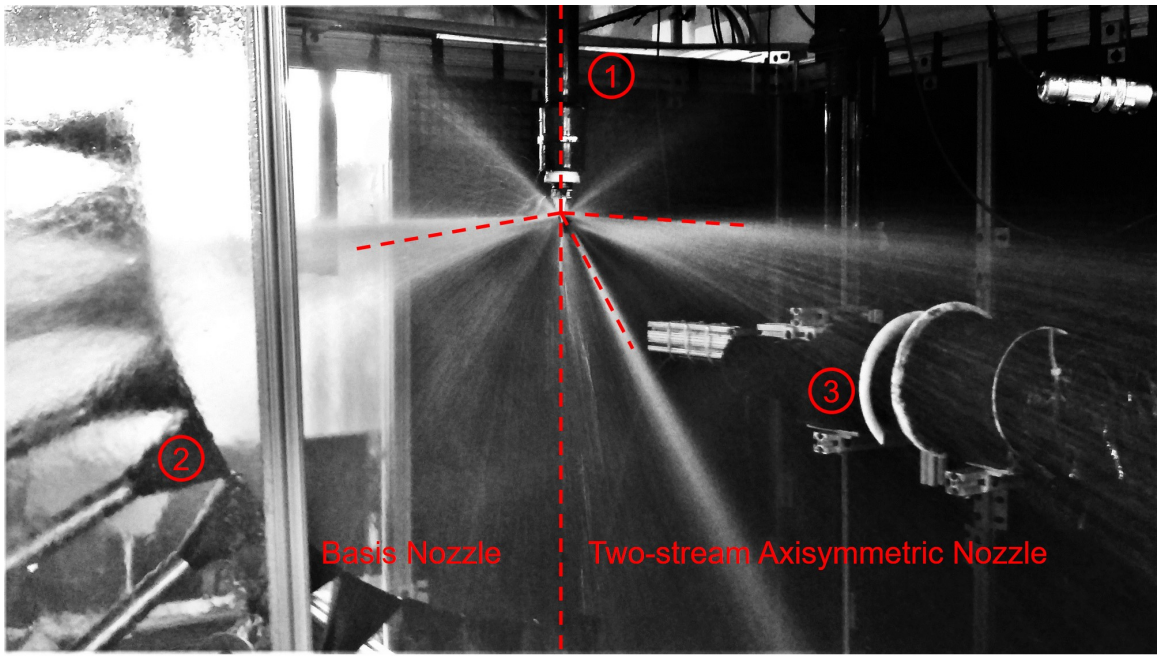

Figure 1.8: The (1) two-sided experimental axisymmetric sprinkler flows water inside the 4S. On the left the basis nozzle sprays into (2) mechanical sphere patternation and on the right the two-stream axisymmetric sprinkler sprays into the (3) optical sphere patternation.

previous predictive models of the fire sprinkler spray because it harmonizes and unifies the three stages of sprinkler spray evolution allowing for prediction in continuous stream from injection on. Research on each individual phase is well established throughout the literature, but does not allow for prediction of the spray in a continuous stream from injection to the far-field. Work by Myers et al. [12] and Meredith et al. [13], provide two distinct ways of predicting deflection but no way to connect these predictions to the resulting initial or far-field spray. Work by Ren et al. [7, 14] provides robust predictions of spray atomization tied to a spray injection framework, but these predictions do not directly connect to the sheets resulting from spray deflec-

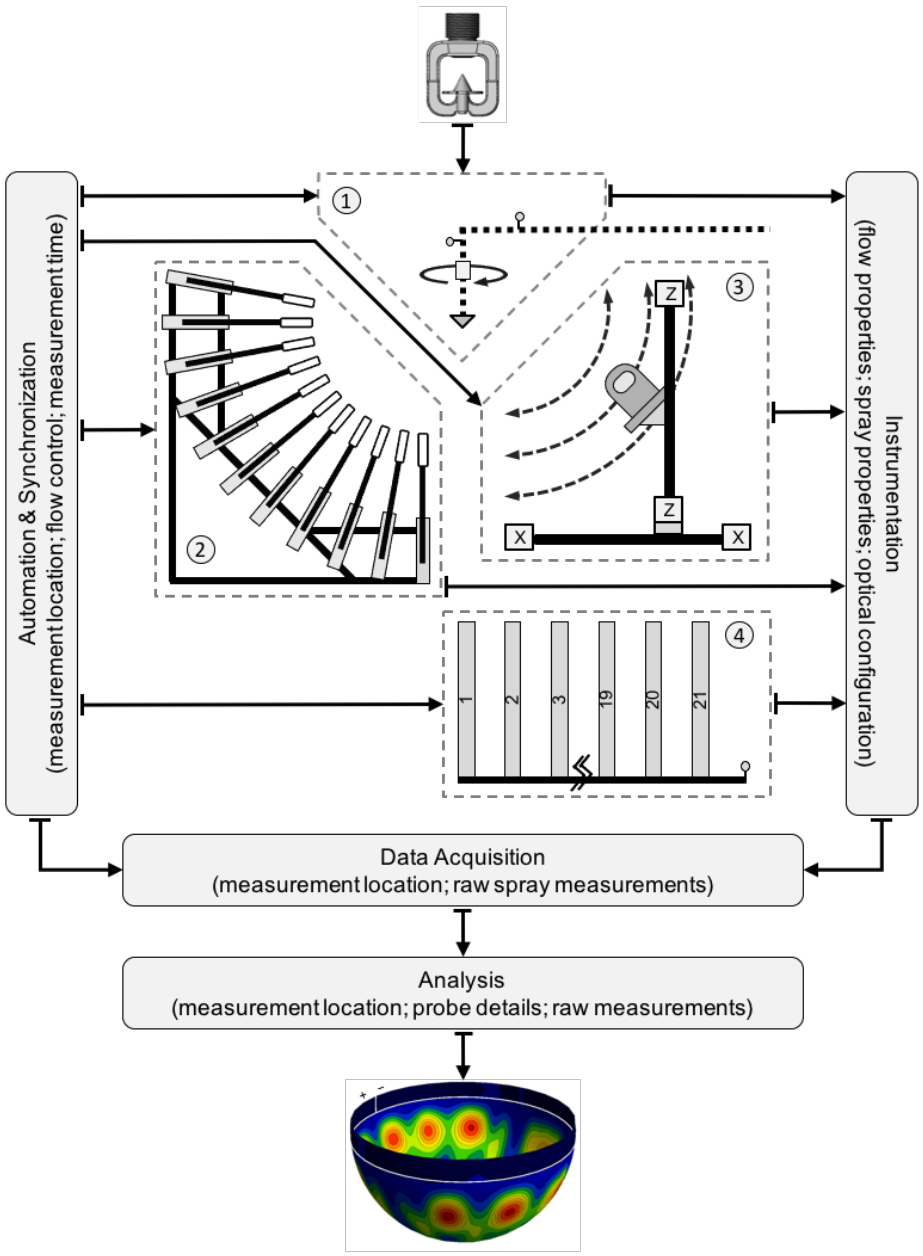

Figure 1.9: Spatially-resolved Spray Scanning System (4S) measurement processes and subsystem elements (dashed regions): (1) flow control and conditioning, (2) mechanical sphere patternation, (3) integral line patternation, (4) optical sphere patternation [3].

tion. Further, previous models of spray injection and dispersion [15] can represent the initial spray, but do not reflect the breakup surface physics suggested by atomization.

In contrast to these previous models, the DAD framework provides boundary conditions for each stage that reflect the physics of the spray, mirror measurement techniques, and join directly to the other stages, as shown in Fig. 1.5 and Tabs. 2.1, 3.1, and 4.1. This harmonization not only allows for comprehensive modeling, as demonstrated in this work, but also facilitates semi-empirical approaches. With the recent development of fast, high fidelity spray measurement systems, like the Spatially-resolved Spray Scanning System (4S), it will be more practical in some cases to simply measure the initial spray and forgo the prediction of deflection and atomization. The measured initial spray properties can then be fed directly into the dispersion model and used to predict the interaction of the fire sprinkler with the space. The novel description mechanism produced in this work [16] has proven useful in describing measurements of the initial spray for better subsequent predictions of dispersion, as seen in Link et al. [17].

This thesis is organized as follows. Each of the subsequent chapters in this work, Chapters 2, 3, and 4, develops one of the three models shown in Fig. 1.5. Chapter 2 describes deflector interaction using a boundary integral method (BIM) model, initially developed by Myers et al. [12] and expanded in this work. Chapter 3 describes atomization of the flapping fluid sheets extending linear stability theory

scaling laws developed by Ren et al. [14] to better harmonize with experimental measurements and a statistical description of the spray [16]. Chapter 4 details a FireFOAM Lagrangian particle injection model based on the statistical description of the spray presented in Chapter 3. Additional guidance on Lagrangian particle tracking model of spray dispersion and resolution requirements introduced by the Lagrangian particles are also provided. Lastly, Chapter 5 provides a summary of the contributions of this research and conclusions about the comprehensive sprinkler spray prediction framework.

Chapter 2: Deflection

2.1 Introduction

The deflection model is the first component of the Deflection Atomization Dispersion (DAD) framework for sprinkler spray prediction shown in Fig. 1.5. The goal of the deflection model presented in this chapter is to predict tine and slot sheet properties based on sprinkler geometry and operating pressure, as shown in Tab. 2.1. The sheet properties predicted by the deflection model inform the atomization model (described in Chapter 3), which in turn predicts the initial spray that disperses throughout the protected space (described in Chapter 4). In this chapter, a boundary integral method (BIM) model of deflection is developed and applied to the axisymmetric sprinklers described in Sec. 1.3. The predicted sheet properties are then compared to experimental measurements of the same axisymmetric sprinklers made using the University of Maryland Spatially-resolved Spray Scanning System (4S).

The deflection portion of fire sprinkler spray evolution can be decomposed into the formation of the initial fluid jet and the interaction of the jet with the deflector.

Table 2.1: Deflection model inputs, parameters, and outputs

Model inputs	Jet radius, R_j Deflector radius, R_d Slot radius, R_s Slot area, A_s Injection Pressure, P_{inj}
Model parameters	Grid cell size, dx
Model outputs	Sheet thickness, T_{sh} Sheet velocity, U_{sh}

When a fire sprinkler activates, the sprinkler orifice (see Fig. 1.2) opens. A water jet flows from this orifice, interacting with the spray-forming elements of the sprinkler: the frame arms, boss, and deflector. Part of the initial water jet is directed along the deflector, forming thin fluid sheets (tine sheets) that flow away from and approximately parallel to the deflector. The remainder of the water passes through the slots of the sprinkler deflector, forming sheets (slot sheets) that are primarily directed downward.

Prahl and Wendt [18] modeled this deflection with a simplified geometry in which the discharge distribution was calculated for a basis nozzle model of a fire sprinkler head. The basis nozzle used consisted of a jet impinging normal to and at the center of a flat disk, creating a single thin sheet. With this simple geometry, mass conservation assumptions allow analytic approximations of sheet thickness and velocity, and allowed Prahl and Wednt to ignore the impacts of sprinkler deflector slots.

For a basis nozzle, the orifice of a sprinkler is circular with a nominal diameter, D_0. This diameter, coupled with the gage pressure, p_0, of the sprinkler, determines the total flow rate of water through a sprinkler. This relationship is characterized by a K-factor, K, a constant relating sprinkler flow rate, $\dot{V}$, to gage pressure by

$$\dot{V} = K\sqrt{p_0}. \tag{2.1}$$

Typical values of the K-factor for different orifice diameters are provided in Table 2.2

Table 2.2: K-factors for various nominal orifice diameters, D_0 [19]

D_0 (mm)	$K-Factor$ (l/(min. bar$^{1/2}$)	$K-Factor$ (gpm/psi$^{1/2}$))
5.2	17.3	1.2
6.4	25.9	1.8
7.1	33.1	2.3
8.3	43.2	3.0
9.5	59.0	4.1
11.1	80.6	5.6
12.7	104	7.2

The velocity of the fluid jet, U_j, is determined from Bernoulli's principle as

$$U_j = \sqrt{\frac{2p_0}{\rho_w}}, \tag{2.2}$$

where ρ_w is the density of water. For typical fire sprinklers operating with a gage pressure between 1 and 4 bar, the resulting jet velocities are between 15 and 30 m/s.

By examining flow rate as dictated by pressure and K-factor and velocity given by pressure, it can be shown that a typical jet has a diameter between 0.8 and 1.0 times the orifice diameter, D_0.

By simple analysis, the sheet properties from this basis nozzle may be calculated as in Sec. 2.2.1. These properties may in turn be used to inform subsequent atomization and dispersion models.

The model presented in Ref. [18] lends insight into deflection's impact on sprinkler spray properties, but is overly simplistic because a basis nozzle does not include deflector plate slots typical of real fire sprinklers. For geometries more complex than the basis nozzle, water distribution cannot be found analytically. A number of researchers have previously attempted to model the fluid motion of a fire sprinkler head. Historically, two different approaches have been used to predict the water deflection of a sprinkler head: a volume of fluid (VOF) approach and a boundary integral method (BIM) approach.

Ren, in unpublished work conducted at the University of Maryland, explored the use of computational fluid dynamics (CFD) in modeling traditional pendent sprinkler heads. In a preliminary study to address the challenge of locating the liquid-gas interface (and the associated sheet thickness and velocity), the VOF method, as outlined by Hirt et al. [20], was applied to simulate deflection of a fluid jet by a sprinkler head. The VOF method tracks the shape and position of the liquid-air

interface during multi-phase CFD simulations. Further work by Meredith et al. [13] also explored VOF simulations of spray deflection for a large orifice sprinkler, which were shown to be in good agreement with experimentally measured volume flux. There are drawbacks to the VOF method, however. The computational burden of this type of method is prohibitive because of the mesh requirements for resolution of the thin sheets (which typically require grid sizes of tens of microns) are of a different order of magnitude than the deflectors that form them (which typically require grid sizes of tens of millimeters).

An alternative to the VOF method is the boundary integration method (BIM). Work by Myers [12], provided the foundations of a BIM model applied to an axisymmetric sprinkler head with a slot. In the BIM, the interior flow is assumed to be purely a function of conditions along the boundaries [21]. Because only information about what is occurring along the surface is necessary to determine the entire flow, the effective spatial dimensions of the problem are reduced by one. In other words, three-dimensional problems become two-dimensional, and two-dimensional problems, like an axisymmetric sprinkler, become one-dimensional. This method allows for a dramatic reduction of computational expense without any loss of accuracy.

The root and applicability of the BIM method can be seen in early work by Schach [22]. Schach characterized the deflection of an axisymmetric water jet on a flat plate perpendicular to the flow direction using the Prandtl hodograph method.

The free surface of the the outer jet was compared with previous experimental measurements of impinging jets [23]. In Ref. [22] work a method for treating the flow using potential flow assumptions is outlined. The method calls for the transformation of a differential equation of the fluid potential into an integral equation for axisymmetric flow by superposition of a ring flow. Ref [22] identifies the chief problem with the formulated solution as the lack of a known shape for the free surface boundary. Schach observes that for a true potential flow where all flow is deflected by the plate, the flow approaches a hyperbola as it approaches an infinite radius. Further along the free surface the fluid has a constant speed equal to the inlet speed.

Work by Lienhard on impinging circular jets demonstrates that the flow field of an impinging jet is independent of Reynolds number and may be represented by a potential flow that scales with the inlet speed and jet diameter [24]. Low levels of turbulence in the incoming jet are likely to only slightly affect the mean velocity distribution outside the wall boundary layer, so the inviscid solutions apply to both laminar or turbulent jets [24]. Additionally, there is no flow normal to the jet boundary and thus the liquid-air boundary is a free streamline. The boundary conditions on the free streamline are well known, namely no shear stress (implying a constant velocity) and a constant, atmospheric pressure (meaning no normal flow).

As a result of the above foundations the deflecting sprinkler jet may be described as a free surface flow where all of the vorticity of the flow is contained within the

free surface and the interior of the water jet is described as a velocity potential. A free surface describes the surface of a fluid that is subject to constant perpendicular normal stress. The boundary between two homogeneous fluids, in this case, the impinging water jet and the surrounding air, can be described as a constant pressure-free surface. There is no flow normal to the jet boundary and the liquid-air boundary is a free streamline. Because this flow may be described as a free-surface flow the BIM may be used.

In the present work, the initial BIM model developed by Myers [12] is expanded to predict the two axisymmetric sprinklers outlined in Sec. 1.3. The initial formulation of Ref. [12] has been improved with new boundary conditions and refined using more robust computational methods. In this study, it is applied to the two axisymmetric nozzles, and compared to experimental measurements of the same equipment.

2.2 Methods

2.2.1 Modeling

The goal of the deflector model presented in this chapter is to use the initial conditions of a sprinkler (sprinkler geometry and operating pressure) to produce a map of the fluid flow leaving the deflector, which will provide the input for the atomization or breakup model. In this work, the fluid flow leaving the sprinkler is assumed to take

the form of fluid sheets analogous to the sheets formed by the basis nozzle explored by Prahl and Wendt [18]. In this axisymmetric nozzle, as shown in Fig. 1.6, with tine and slot sheets both expanding radially from the deflector center, passing above the deflector or through the slots, respectively. This assumption is later validated through experimental measurements of the same, as photographed in Fig. 1.8.

In this investigative approach a boundary integral method (BIM) is used to solve for sheet flow splits and sheet velocity angles, which may be used with injection properties to calculate sheet thickness and sheet velocity. The boundary integral method is particularly suitable for the axisymmetric sprinkler as the low computational costs allow the full range of sprinkler geometry effects to be explored. This modeling approach is based on earlier work in Ref. [12]. Other methods, such as the VOF method, may be more suitable for sprinklers with more complex geometries. However, the outputs of sheet thicknesses and sheet velocity are predicted by both VOF and BIM models.

For a basis nozzle, sheets are defined by the relationship

$$T_{sh} U_{sh} r_{sh} = \frac{D_0^2 U_j}{8}, \tag{2.3}$$

where T_{sh} is the sheet thickness, U_{sh} is the sheet velocity, and r_{sh} is the distance of the sheet from the center of the deflector.

Viscous effects, both the slowing of the flow and the resultant thickening of the

sheet, can be accounted for by using a sheet thickening factor, β. Sheet thickening occurs as a result of viscous interaction between the fluid and the sprinkler deflector, and can be approximated as a function of the jet Reynolds number as

$$\beta = 1 + 0.196\ Re^{-1/5} \left(\frac{R_d}{2R_j} \right)^{9/5}, \tag{2.4}$$

where the jet Reynolds number given by $Re = R_j\ U_j/\nu_l$, R_j is the jet radius, ν_l is kinematic viscosity of the liquid water, and R_d is the deflector radius where $R_0 < 0.366 R_j\ Re^{1/3}$ such that the viscous boundary layer never reaches the free surface [14]. When the sheet thickening factor, $T_{sh} = \beta D_0/8r_{sh}$, is incorporated, the sheet velocity magnitude is given by $U_{sh} = U_j/\beta$.

The initial flow from a sprinkler may be described as a series of N basis nozzle sheets, having an angular location and extent in spherical coordinates and a sheet thickness factor or flow split, α_i, corresponding to the ratio of observed sheet volume flow to basis nozzle sheet volume flow for a nozzle of similar orifice diameter,

$$\sum_{i=1}^{N} \frac{(T_{sh} U_{sh} r_{sh})_i}{D_0^2 U_j/8} = \sum \alpha_i = 1. \tag{2.5}$$

In the axisymmetric sprinklers described here there are two sheets: a tine sheet coming from the edge of the deflector and a slot sheet coming through the slot, as seen in Fig. 1.6. Each sheet moves radially away from the deflector center and because the

sheets are free surfaces the sheet velocity magnitude is simply the initial jet velocity. As a result, each axisymmetric sheet may be totally defined by two quantities: the flow split, α, and an angular location, given by the elevation angle θ. Due to conservation of mass, for an axisymmetric sprinkler, the tine sheet flow split, α_t, and slot sheet flow split, α_s, have the relationship

$$\alpha_t + \alpha_s = 1. \tag{2.6}$$

The boundary integrals describing the fluid flow on the deflector can be formulated by posing the impinging jet velocity field $\vec{u}(\vec{r})$ with a velocity potential $\phi(\vec{r})$ satisfying Laplace's equation,

$$\nabla^2\phi(\vec{r}) = 0 \tag{2.7}$$

and

$$\vec{u}(\vec{r}) = \nabla\phi(\vec{r}), \tag{2.8}$$

where $\vec{r}$ is a spatial vector in cylindrical coordinates corresponding to a field point [12].

The resulting integral allows the velocity potential $\phi(\vec{r})$ at any point within the posed problem domain to be represented using only information regarding the velocity potential and fluid velocity along the boundaries of the domain. The boundary integral method can then be used to generate a numerical solution to the above integral equations, through the successive approximation and reevaluation of the boundary

values of the posed problem [12]. The result is very general, and makes no assumptions about specific boundary conditions or boundary shapes. Any solution obtained is an exact solution to the invicid flow equations and the interior flow is an exact solution to the Navier-Stokes equations. The effective spatial dimension of the boundary integral method is one less than that of a problem computed with the finite volume CFD method, because the solution in only calculated on the boundary instead of within the area. As a result, the total number of computations is drastically reduced.

A boundary integral solution for this interior flow may be developed using a Green's function, where a Green's function of Laplace's equation is defined as the solution to

$$\nabla^2 G\left(\vec{r}, \vec{r_0}\right) = \delta\left(\vec{r} - \vec{r_0}\right), \tag{2.9}$$

where $\vec{r_0}$ is a spatial vector representing a singular point, or pole, and $\delta\left(\vec{r} - \vec{r_0}\right)$ is the Dirac delta function in three dimensions.

An integral describing the velocity potential, $\phi(\vec{r})$, as an integral taken over the entire volume encompassing the problem domain can be written as

$$\phi(\vec{r}) = \int \left[\phi(\vec{r_0})\nabla^2 G\left(\vec{r}, \vec{r_0}\right) - G\left(\vec{r}, \vec{r_0}\right)\nabla^2\phi(\vec{r_0})\right] d^3\vec{r_0}. \tag{2.10}$$

This integral can be rewritten using the Divergence Theorem as

$$\phi(\vec{r}) = \oint \left[\phi(\vec{r_0}) \left(\hat{n}\left(\vec{r_0}\right) \cdot \nabla G\left(\vec{r}, \vec{r_0}\right)\right) - G\left(\vec{r}, \vec{r_0}\right) \left(\hat{n}\left(\vec{r_0}\right) \cdot \nabla \phi\left(\vec{r}, \vec{r_0}\right)\right)\right] d^2 s. \tag{2.11}$$

The computational speed of this method, owing to the dimensional reduction, allows for the computation of sheet formation for a wide variety of sprinkler geometries. For the purposes of this study, investigation is limited to the study of an axisymmetric sprinkler. Three-dimensional complexity, while necessary for capturing real sprinklers, obscures the impact of essential sprinkler geometric features. As a result, while the framework and equations developed in the next section are applicable to a three-dimensional geometry, the boundary conditions are limited exclusively to an axisymmetric sprinkler. The specific details of our axisymmetric sprinklers are fully described in Sec. 1.3.

In this subsection, the boundary conditions necessary for specifying an axisymmetric sprinkler are outlined and detailed. Then, guidance into the numerical implementation of the iterative model is performed. In the next section, model results are used to demonstrate the impact of sprinkler geometry on the fluid sheets formed by the deflector. These sheet properties will be used as initial conditions in the atomization model in Chapter 3.

2.2.1.1 Boundary Conditions

Before proceeding to explore the boundary conditions of the axisymmetric sprinkler, it is useful to introduce several dimensionless variables:

$$\phi = U_j R_j \tilde{\phi}(\tilde{r}, \tilde{z}), \qquad \tilde{r} = r/R_j, \qquad \tilde{z} = z/R_j, \qquad \tilde{u} = \frac{\partial \tilde{\phi}}{\partial \tilde{r}}, \qquad \tilde{v} = \frac{\partial \tilde{\phi}}{\partial \tilde{z}}. \tag{2.12}$$

The tilde notation will be dropped for the remainder of the paper for the convenience of the vector notation. As a result, all radii and velocities, unless explicitly noted, are the non-dimensionalized radii and velocities as described above. Owing to this non-dimensionalization, $R_j = 1$ and $U_j = 1$.

The axially symmetric form of the potential flow equation is given by

$$\frac{1}{r}\frac{\partial}{\partial r}\left(r\frac{\partial \phi}{\partial r}\right) + \frac{\partial^2 \phi}{\partial z^2} = 0. \tag{2.13}$$

In order to outline the boundary conditions it is first necessary to choose a suitable Green's function. The axisymmetric Green's function can be taken by angularly integrating Eq. (2.9). The result takes the form

$$\mathcal{G}\left(\vec{r},\, r_0,\, z_0\right) = -\frac{1}{4\pi}\int_0^{2\pi} \frac{1}{\sqrt{r^2 + r_0^2 - 2rr_0\cos(\theta - \theta_0) + (z - z_0)^2}}\, d\theta_0. \tag{2.14}$$

The quantity, $\mathcal{G}$, represents the flow field given by a ring source of fluid situated at

$r = r_0,\ z = z_0$. Making use of symmetry, this axisymmetric Green's function can then be rewritten as

$$\mathcal{G}\left(\vec{r},\, r_0,\, z_0\right) = -\frac{1}{\pi\sqrt{(r+r_0)^2+(z-z_0)^2}}\int_0^{\pi/2}\left(1-\frac{4rr_0}{(r+r_0)^2+(z-z_0)^2}\,\sin^2(\theta)\right)^{-1/2}\,d\theta. \tag{2.15}$$

This function can be evaluated in terms of the complete elliptic integrals of the first kind, providing a known solution. The complete elliptic integral of the first kind is denoted as $K(m)$ and defined as

$$K(m) = \int_0^{\pi/2}\left(1-m\,\sin^2(\theta)\right)^{-1/2}\,d\theta. \tag{2.16}$$

Substituting in Eq. (2.16) into Eq. (2.15), the Green's function may be rewritten as

$$\mathcal{G}\left(\vec{r},\, r_0,\, z_0\right) = -\frac{1}{\pi\sqrt{(r+r_0)^2+(z-z_0)^2}}\,K\left(m\right) \tag{2.17}$$

where

$$m = \frac{4rr_0}{(r+r_0)^2+(z-z_0)^2}. \tag{2.18}$$

This axisymmetric Green's function can again be refined by posing a "no-penetration condition" at $z = 0$ (the defined location of the deflector surface) as

$$\mathcal{G}_1\left(\vec{r},\, r_0,\, z_0\right) = \mathcal{G}\left(\vec{r},\, r_0,\, z_0\right) + \mathcal{G}\left(\vec{r},\, r_0,\, -z_0\right). \tag{2.19}$$

Similar to $\mathcal{G}$, $\mathcal{G}_1$ represents a ring source situated at $r = r_0$, $z = z_0$ but located in a semi-infinite space bounded above the line $z = 0$.

There are four bounding surfaces in the axisymmetric sprinkler:

1. Jet, an inlet disk of radius R_j located at a given height, Z_j, described in Sec. 2.2.1.2;

2. Free Surface, the bounding free streamline surface. This surface can be divided into three regions. The free surface of the asymptotic jet, the free surface of the asymptotic tine stream, and the turning region which connects the two, described in Sec. 2.2.1.3;

3. Tine Stream, a vertical cylinder of radius R_d and height z_d (the vertical distance between the bounding free streamline and the deflector plate) where the flow that does not pass through the deflector plate exits, described in Sec. 2.2.1.4;

4. Deflector, the horizontal deflector plate where flow passes through the ring opening with centroid R_s and total area A_s, described in Sec. 2.2.1.5.

Each boundary integral may be evaluated individually and summed to construct the entire integral as

$$\phi(\vec{r}) = \phi_j(\vec{r}) + \phi_{fs}(\vec{r}) + \phi_{ts}(\vec{r}) + \phi_d(\vec{r}), \tag{2.20}$$

where $\phi_j(\vec{r})$, $\phi_{fs}(\vec{r})$, $\phi_{ts}(\vec{r})$, and $\phi_d(\vec{r})$ correspond to the integral $\phi(\vec{r})$, as defined in Eq. (2.11), evaluated on the surface of the inlet jet, free stream, tine stream, and deflector plate, respectively. This final summation is detailed in Sec. 2.2.1.6.

2.2.1.2 Jet Boundary

In the region $z \gg 1$, far from the deflector plate, we find the jet boundary. Any jet moving straight down with a non-dimensional velocity $\tilde{u} = 1$ must have the fluid potential $\phi(r, z) = -z$, by Eq. (2.8) [12]. The presence of the plate creates a perturbation that expands this jet flow, deflecting the uniform flow across the boundary. The dimensionless potential at this jet boundary can be represented as

$$\phi_{jet}(r, z) = -z + \Phi(r, z). \tag{2.21}$$

The appropriate boundary conditions for the perturbation potential, $\Phi(r, z)$ are

$$\lim \ \Phi(r, z \to \infty) = 0 \tag{2.22}$$

and

$$\left[\left(-1 + \frac{\partial \Phi}{\partial z}\right)^2 + \left(\frac{\partial \Phi}{\partial r}\right)^2\right] = 1. \tag{2.23}$$

The first condition requires that the perturbation to the jet flow vanish sufficiently far from the plate while the second condition arises from the requirement that the

pressure, and thus the jet speed, be uniform at the jet free surface, regardless of perturbation.

A solution for $\Phi(r, z)$ can be found to be

$$\Phi(r, z) = AJ_0(\lambda_0 r)exp(-\lambda_0 z), \tag{2.24}$$

where A is a constant, J_0 is the Bessel function of the first kind, representing perturbations, of order zero and λ_0 is an eigenvalues corresponding to the Bessel function such that $J_0(\lambda_n) = 0$.

By Eq. (2.8), the jet velocity normal to the jet boundary is given by the derivative of Eq. (2.24) with respect to z as

$$v_{jet}(r, z) = \frac{\partial \Phi(r, z)}{\partial z} = -1 - A_0\lambda_0 J_1(\lambda_0 r)exp(-\lambda_0 z). \tag{2.25}$$

The boundary integral, $\phi_j(\vec{r})$, can now be evaluated at the inlet, a horizontal plane located a non-dimensional distance Z_j above the deflector plate as,

$$\phi_j(r, z) = \int_0^{R_j} r_0(\phi_{jet}(r_0, Z_j)\mathcal{G}_1(\vec{r}, r_0, Z_j) - v_{jet}(r_0, Z_j)\frac{\partial \mathcal{G}_1(\vec{r}, r_0, Z_j)}{\partial z})dr_0. \tag{2.26}$$

2.2.1.3 Free Surface Boundary

The chief problem for the proposed boundary value problem is selecting an appropriate shape for the free-surface boundary [22]. An approximation of the surface as a combination of hyperbolas is reasonable for the axisymmetric case [22, 25]. Using the criteria that the non-dimensional free surface must approach $r = 1$ as $z \to \infty$ (horizontal flow) and $z(r) = \alpha_t/2r$ as $r \to \infty$ (by mass conservation) the free-surface can be approximated as

$$z = f(r) = \frac{A}{1-r} + \frac{B}{r}, \tag{2.27}$$

where A and B are constants chosen for continuity with the jet and tine stream boundaries.

Assessing the boundary integral, $\phi_{fs}(\vec{r})$, is greatly simplified by the requirement that there is no normal flow to the free-surface. As a result, the fluid potential on the surface increases linearly with arc-length because the magnitude of the speed in the tangential direction is always 1. The integral is assessed from $r_0 = 1$ (the radius of the jet) to $r_0 = R_d$ (the arbitrary location of the tine stream boundary) along the curve bounded by the free-surface equation given in Eq. (2.27).The equation for the free surface boundary integral, $\phi_{fs}(\vec{r})$ can be written as

$$\phi_{fs}(\vec{r}) = \int_1^{R_d} r_0 \phi(r_0, f(r_0)) \frac{\partial \mathcal{G}_1(\vec{r}, r_0, f(r_0))}{\partial n} dr_0, \tag{2.28}$$

where $\partial\mathcal{G}_1/\partial n$ is given by

$$\partial\mathcal{G}_1/\partial n = \nabla\mathcal{G}_1 \cdot \hat{n}, \tag{2.29}$$

where $\hat{n}$ is the unit normal to the free-surface at any given r_0, and $\mathcal{G}_1$ is given by Eq. (2.19). There is no analytic solution available for this term, but because the elliptic integral of the first kind, Eq. 2.16, is used, Eq. (2.16), numeric solutions are easily attainable.

2.2.1.4 Tine Stream Boundary

In the region near the plate, as $r \to \infty$, the radially expanding tine sheet thins. Because the speed of the sheet is fixed by the requirement of constant pressure, the limiting form of the solution for large r must be $\phi \to U_j r + C$, by conservation of mass. This does not, however, satisfy the definition of the axisymmetric fluid potential, given in Eq. (2.13). To satisfy Eq. (2.13), the solution to the axisymmetric fluid potential in this region can be posed as a descending series, with the leading term, r. The solution for the velocity potential in this region takes the form of the infinite series

$$\phi_{tine}(r, z) = r + F_1(z)/r + F_2(z)/r^3 + ... \tag{2.30}$$

where $F_1(z)$ and $F_2(z)$ are functions chosen to satisfy Eq. (2.13) and the free surface boundary conditions given above.

It should be noted that this form of the solution restricts its validity to a region

of r greater than the radial location of the slot in the deflector plate. A fraction of the flow is diverted through the slot, meaning that mass flow in the tine sheet is not constant if the boundary is taken to cross the slot. After the slot, the fraction of the total flow contained in the tine sheet is constant, and the mass conservation conditions needed here apply.

To solve for the correct $F_1(z)$ and $F_2(z)$, the tine stream boundary conditions must be enforced. Enforcing the boundary condition that as the tine stream moves radially outward vertical velocity tends to zero, or $v(r, 0) = 0$, gives

$$F_1(z) = -z^2/2! + c \tag{2.31}$$

and

$$F_2(z) = z^4/4! + d. \tag{2.32}$$

The constants c and d can be determined from the requirement that the speed is constant at the free surface. To accomplish this, the equation for the free surface must also be expanded into a descending series in r as the tine sheet surface is

$$z(r) = \alpha_t/2r + b/r^3 + ... \tag{2.33}$$

This introduces another constant, b. The solution for ϕ_{tine} given by Eq. (2.30) must also be made consistent with the shape of the free surface. The results yield that

$b = c = 0$ and $d = -\alpha_t^2/4$. This result holds no matter what fraction of the mass flow passes through the plate, subject to the caveat that the domain of applicability lies outside the opening in the plate, i.e. after the flow passes the slot.

This boundary is evaluated at the radius of the plate, $r_0 = R_d$, with the integral spanning $0 < z_0 < z_d$, where z_d is the height of the sheet above the deflector plate given by $z\left(R_d\right)$ from Eq. (2.33). The resulting integral is given by

$$\phi_{ts}(r,z) = \int_0^{z_d} r_0(\phi_{tine}(R_d,z_0)\mathcal{G}_1(\vec{r},R_{ts},z_0) - v_{jet}(R_{ts},z_0)\frac{\partial \mathcal{G}_1(\vec{r},R_d,z_0)}{\partial z})dz_0. \quad (2.34)$$

2.2.1.5 Deflector Boundary

The final boundary, the deflector, is evaluated at $z_0 = 0$ and spans $0 < r_0 < R_d$. Because of the choice of Green's function, $\partial\mathcal{G}_1/\partial n$ is equal to 0 at all $z = 0$. The term, $\partial\phi/\partial n$ is also equal to 0 at all points where there is no penetration through the boundary. As a result, the integral, $\phi_d(\vec{r})$, can be written as

$$\phi_d(\vec{r}) = \int_0^{R_d} r_0 v(r_0,0)\mathcal{G}_1(\vec{r},r_0,0)dr_0, \quad (2.35)$$

where $v(r_0,0)$ is the velocity through the deflector plate. This velocity is zero at all locations except through the ring opening of the slot. Thus, $v(r_0,0)$ is the profile of flow through the ring opening with centroid R_s and total area A_s. This flow profile can be assessed based upon the typical results of two-dimensional slot flow.

The free surface of the slot stream must have a gage pressure of zero, or a velocity magnitude equal to the velocity magnitude of the jet free surface by free surface theory [26]. The velocity normal to the slot, $v(R_s, 0)$, can then be calculated from the horizontal velocity at the slot, $u(R_s, 0)$, as

$$v(R_s, 0) = \sqrt{1 - u(R_s, 0)^2}. \tag{2.36}$$

Because the exit is not a smooth, well-contoured nozzle, but rather a flat plate, the width of the slot stream will be less than the width of the slot opening. This vena contracta effect is a result of the inability of the fluid to turn the sharp corner of the flow [26]. Because the streamlines in the exit plane are curved, the pressure across them is not constant. We are not interested in the details of this flow pattern, but only the total flow through the slot. The assumption of a uniform velocity with straight streamlines is not valid at the exit plane, but is valid in the plane of the vena contracta [25]. A flow coefficient, C_d, can be used to calculate the ratio between the idealized mass flow, $\dot{m}_i$, given by Bernoulli, and the actual mass flow through a slot, $\dot{m}_a$, as

$$C_d = \frac{\dot{m}_a}{\dot{m}_i}. \tag{2.37}$$

In general a flow coefficient accounts for all of the physics not included in the ideal flow model; for example, contraction, turbulence, and viscous effects. The value

of C_d is well explored for the case of a small slot, as in the case of an orifice plate. In Leinhard [25] this value is given as

$$C_d = \frac{\pi}{\pi + 2} \approx 0.61. \tag{2.38}$$

This is the slot coefficient for small, sharp-edged orifices. For an orifice plate, this requirement is given by $R_0/R_j \ll 1$, where R_0 is the radius of the orifice and R_j is the radius of the flow approaching the orifice [25]. An analogy can be made for a standard sprinkler by requiring that $\theta_{slot}/2\pi \ll 1$, where θ_{slot} is the angular extent of a single slot, and similar to the case of the axisymmetric sprinkler, by requiring $\Delta R/R_s \ll 1$.

This requirement, and the definition of ΔR, limits the choice of sprinkler geometries to any situation where

$$\frac{A_s}{2R_s^2} \ll 1. \tag{2.39}$$

.

Total flow through the slot can than be approximated as flow of a uniform velocity, as given by Eq. (2.36). Ideal mass flow through the slot is simply

$$\dot{m}_i = \rho A_s v(R_s, 0), \tag{2.40}$$

where ρ is the fluid density, A_s is the slot area, and the velocity normal to the

slot opening, $v(R_s, 0)$, as given by Eq. (2.36). Actual flow, as given by Eq. (2.37), is then

$$\dot{m}_a = C_d \rho A_s v(R_s, 0). \tag{2.41}$$

In the non-dimensional formulation, the total mass flow is simply $U_j A_j = 1$. The slot sheet flow split is then given as

$$\alpha_s = C_d A_s v(R_s, 0). \tag{2.42}$$

2.2.1.6 Full Boundary Integral

The boundary integrals for the jet, free surface, tine stream, and deflector can be summed to calculate the full potential, as in Eq. (2.43), as

$$\begin{aligned}
\phi(\vec{r}) = &\int_0^{R_j} r_0(\phi_{jet}(r_0, Z_j)\mathcal{G}_1(\vec{r}, r_0, Z_j) - v_{jet}(r_0, Z_j)\frac{\partial \mathcal{G}_1(\vec{r}, r_0, Z_j)}{\partial z})dr_0 \\
&+ \int_{R_j}^{R_d} r_0 \phi(r_0, f(r_0))\frac{\partial \mathcal{G}_1(\vec{r}, r_0, f(r_0))}{\partial n} dr_0 \\
&+ \int_0^{z_d} r_0(\phi_{tine}(R_d, z_0)\mathcal{G}_1(\vec{r}, R_{ts}, z_0) - v_{jet}(R_{ts}, z_0)\frac{\partial \mathcal{G}_1(\vec{r}, R_d, z_0)}{\partial z})dz_0 \\
&+ \int_0^{R_d} r_0 v(r_0, 0)\mathcal{G}_1(\vec{r}, r_0, 0)dr_0.
\end{aligned} \tag{2.43}$$

This boundary integral has no analytical solution but can be solved numerically to calculate the fluid potential at any interior point in the flow. The implementation of this numerical integration scheme and the iterative process used to converge on

the flow splits, α, are discussed next.

2.2.1.7 Numerical Implementation

The fluid potential, $\phi(\vec{r})$, at any interior location, $\vec{r}$, of the the impinging jet is given by the boundary integral, Eq. (2.43). This boundary integral has no analytic solution, and instead must be solved numerically. This fluid potential can be used to calculate the tine and slot sheet velocity angles, θ_t and θ_s, respectively, and to calculate the tine and slot sheet flow splits, α_t and α_s, respectively. Because of assumptions about sheet geometry and behavior, these values can in turn be used to explicitly calculate sheet thickness and velocity.

In contrast to other discretization methods, the boundary integral method necessitates the integration of singular kernels, which arise in the Green's functions of the corresponding partial differential equations [27]. If the source point is outside of the element of integration (i.e. if the integration element does not fall on the boundary), then the integrals are non-singular [27]. However, from a numerical integration perspective, one must also be wary of evaluation of "nearly singular" integrals, which are potentially singular when the source point is near the element of integration. This is because integrands of nearly singular integrals vary drastically with the distance [28]. Further, for boundary integral methods, improved accuracy is achieved with finer boundary element discretization, but these improved results come at the cost of additional computational expense [29]. Various numerical techniques

have been developed to remove near singularities [28], but traditionally require cumbersome variable transformations to eliminate near singularities and are frequently highly dependent on optimization parameters [27].

In this work, the boundary integral, Eq. (2.43), is evaluated in Mathematica using the built-in NIntegrate function. NIntegrate is a general numerical integrator and can handle a wide range of one-dimensional and multidimensional integrals [30]. In general, NIntegrate estimates the integral through sampling of the integrand value over the integration region. NIntegrate uses algorithms, called integration strategies, that compute integral estimates from a set of integrand values using specific integration rules [30].

For these calculations the Lobatto-Kronrod integration strategy was used. The Lobatto integration rule is a Gauss-type rule with preassigned sampling points. The end points of the integration interval and optimal sampling points inside the interval are used to form a weighted sum of the integrand values. The Kronrod extension of a Lobatto rule adds new sampling points in between the Lobatto rule points and forms a higher-order rule that reuses the Lobatto rule integrand evaluations [30]. Gauss quadratures have been suggested as an effective method for the integration over singular points [27] and the Lobatto polynomial approach has been suggested as an effective transform to "continuous element discretization" [31]. Further, a simple analysis of error for various integration strategies in a test case demonstrated that the

Lobatto-Kronrod rule is the most effective method, and conveniently, has a minimal computational cost per point.

The shape of the free surface and the flow through the deflector boundary are both dependent on the slot sheet flow split, α_s, which cannot be known a priori. As a result, an iterative process must be performed to converge on the true α_s, and thus the true boundary conditions, for a given sprinkler geometry. In these cases, the slot sheet flow split is calculated by Eq. (2.42), which depends on the area of the slot and the normal velocity to the plate at the slot centroid. The normal velocity at the slot centroid is determined by an analysis of the fluid potential at the slot centroid, as shown in Eq. (2.36).

To converge on the flow split the following cycle is performed.

1. Estimate the slot sheet flow split, α_s.

2. Construct the appropriate boundary integral, Eq. (2.43), as a function of the sprinkler geometry and the estimated flow split.

3. Calculate the fluid potential at the slot centroid, R_s, to determine the velocity normal to the slot centroid using Eq. (2.36).

4. Determine a new slot sheet flow split, α_s, using Eq. (2.42).

5. Repeat steps 2-4 until the the flow split converges on the true solution.

This iterative process typically takes on the order of 10 seconds for an axisymmetric case when computed using a single 3.4 GHz processor. While this calculation time would be substantially increased for a dimensional problem, it still represents a substantial cost savings over traditional finite volume CFD methods, which can require days or weeks of computation on dozens of parallel processors.

2.2.2 Experiments

To validate predictions of deflector interactions, very-near-field, spatially-resolved volume flux measurements of the sprinklers detailed in Sec. 1.3 were taken using the University of Maryland 4S. The experimental sprinkler was run at pressures of 1, 2, and 3 bar. In order to assess sheet properties after deflection, mechanical measurements were made at a radius of 0.4 m from the deflector center.

The pressure was verified by pressure transducer measurements upstream of the sprinkler head. This pressure transducer was previously calibrated using flow rate measurements from sprinklers with known K-factors. Further verification of pressure and flow rate were performed using so-called "bucket tests," in which all water flowing from a sprinkler is collected in a bucket for a fixed time period. The mean flow rate over this period is then calculated from the mass of the water in the bucket. The total sprinkler flow rates at 1, 2, and 3 bar were measured in this way as 80.6, 114, and 140 l/min, respectively, and these agreed with the predicted flow rates

based on sprinkler K-factor.

Continuous mechanical volume flux measurements were made on a hemisphere centered on the sprinkler with a radius of 0.4 m. Collection heads continuously sampled water flow as the sprinkler rotated, providing continuous data in the azimuthal direction from eleven elevation angles, which spanned from 80° to 180°. The rate of change in volume collected at each probe location was measured by physically storing all water captured over the duration of one test and continuously monitoring water height through pressure measurements. Water height was measured using Setra 209 pressure transducers attached to each cylinder array and sampling at 4 Hz. These volume flow measurements were used to directly calculate spray volume flux.

Within the 4S, a series of automated linear actuators enable the spray to be probed at a series of radial distances from the deflector, ranging from 0.05 m to 0.6 m. Previous experimental studies by Jordan [3], suggest that a radial measurement location of 0.4 m was appropriate for a sprinkler of similar characteristics.

For each test, the collection cylinder arrays at each elevation angle were sized to optimize the measurement over the full dynamic range of the pressure transducer. Each rotation of the sprinkler lasted 55 minutes, a test duration chosen to provide sufficient azimuthal resolution of the spray.

The sprinkler measured, shown in Fig. 1.7, consists of two effective axisymmetric sprinklers. The basis nozzle spans from $\phi = -60° \rightarrow 60°$ and the two-stream

axisymmetric sprinkler spans from $\phi = 120° \rightarrow 240°$. These angles are chosen such that the impact of the sprinkler frame arms on the flow may be neglected. There are three distinct sheets emerging from this sprinkler, as seen in Fig. 1.8: the tine sheet from the basis nozzle, the tine sheet from the two-stream axisymmetric sprinkler, and the slot sheet from the sprinkler with a slot. For this sprinkler, the slot sheets and the tine sheets form easily distinguished flow structures, with no overlap. The tine sheets sprays into the collector centered at 90° and the slot sheet sprays into the collector centered at 150°. To determine flow from a single sheet, the total volume flow over the angular arc of the sheet is integrated and divided by the total volume flow expected over the same angular arc.

Sheet angle was determined by fitting Gaussian curves to azimuthally averaged volume flux profiles. These Gaussian curves have means corresponding to sheet angle, standard deviations corresponding to sheet spread angle (discussed further in Chapter 3), and amplitudes corresponding to average volume flow contained in the sheet. Additional visual inspection using the 4S shadowgraphy equipment was conducted to verify sheet angle and the results agreed strongly within observational error ($\pm 2°$).

2.3 Results

The model outlined above may be used to rapidly explore the impact of geometry on sprinkler sprays. Recall that the quantities of interest are the sheet thickness

and sheet velocity angle, where sheet velocity magnitude is simply the velocity of the free surface, or the injection velocity. Each property may be a function of the non-dimensional deflector radius R_d, the non-dimensional slot radius R_s, and the non-dimensional slot area A_s.

The flow splits of the axisymmetric sprinkler sheets are only a function of the the non-dimensional slot radius R_s, and the non-dimensional slot area A_s, because the amount of water that leaves through the slot is determined upstream of the deflector radius R_d.

Figures 2.1(a) and (b) show the tine sheet and slot sheet flow splits, respectively. These flow splits, or the fraction of the total flow which passes through either the tine or the slot of an axisymmetric sprinkler, are purely a function of slot geometry. It can be seen that as the area of the slot A_s increases, the fraction of the flow that can pass through the slot also increases. Conversely, as the slot radius R_s increases, the slot sheet flow split decreases. This change can be attributed to a turning of the flow. As the slot centroid moves radially further out, the flow turns increasingly horizontal and so passes over the slot without penetrating through it.

The sheet velocity angles θ are determined by the direction of the flow immediately prior to leaving the deflector. The turning of the flow, from the vertical direction of the jet, $\theta = 180°$, to the horizontal direction of the slot sheet, $\theta = 90°$, is purely a function of non-dimensional radius. Because the flow moves radially away from the

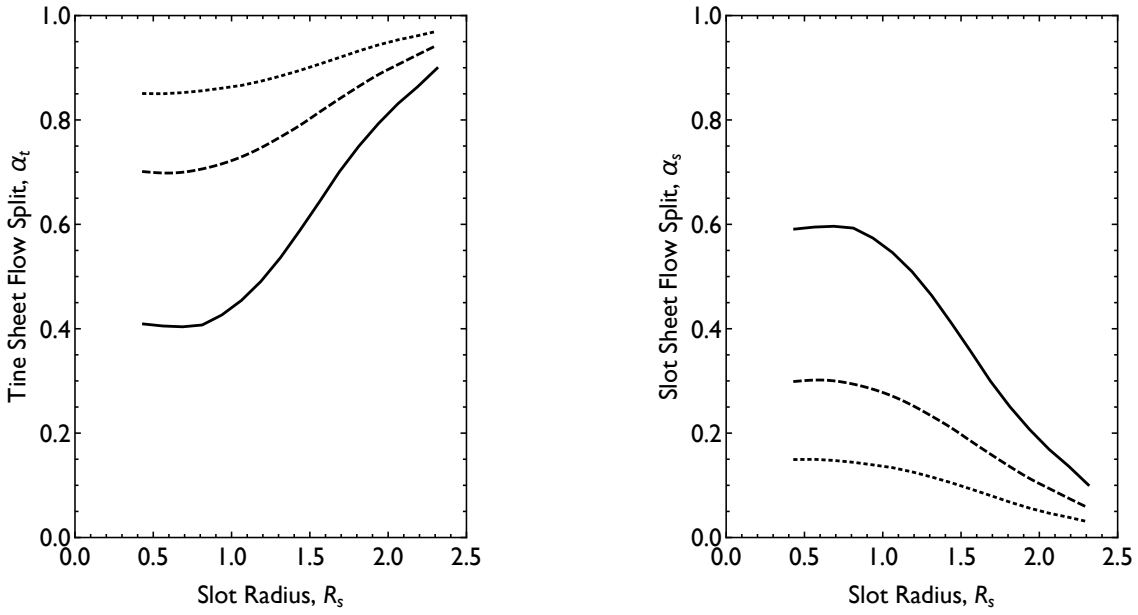

Figure 2.1: The tine sheet flow splits (a) and slot sheet flow splits (b) from an axisymmetric sprinkler as a function of sprinkler geometry. The solid curve, dashed curve, and dotted curve have non-dimensional slot areas $A_s = 0.25$, 0.5, and 1.0, respectively.

center of the deflector, the velocity angle of the tine sheet and the slot sheet can be determined by internal inspection of the flow velocity at the location of the tine sheet and slot sheet boundaries.

Figure 2.2 shows the measured sheet angle, θ, as a function of non-dimensional radius, r. As the deflector radius or slot radius increases, the tine sheet or slot sheet velocity angle approaches the horizontal, 90°.

We now turn our attention to the two axisymmetric sprinklers outlined in Sec. 1.3. Applying the boundary integral model, sheet properties (sheet flow split and angle) can be calculated for both sprinklers under each operating condition, as seen

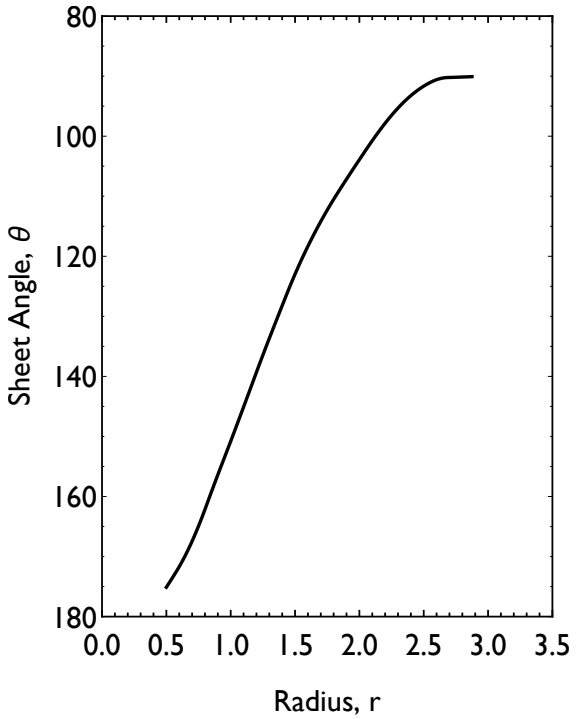

Figure 2.2: The sheet velocity angle, θ, of the tine and slot sheets of an axisymmetric sprinkler as a function of deflector radius, r. This angle is an elevation angle with 0° corresponding to the north pole, (i.e., directly above the sprinkler), and 180° corresponding to the south pole (i.e., directly below the sprinkler).

in Tab. 2.3. It can be seen that sheet thickness is independent of pressure because free surface theory ignores viscous effects. Sheet velocity for both sheets is then determined entirely by the jet velocity, which is in turn determined by the operating pressure, given by Eq. (2.2).

Table 2.3: Model predictions of initial sheet

	Basis Nozzle			Axisymmetric Tine			Axisymmetric Slot		
Injection pressure, $P_{inj}(bar)$	1	2	3	1	2	3	1	2	3
Flow split, α	1.00	1.00	1.00	0.46	0.46	0.46	0.54	0.54	0.54
Sheet trajectory angle, θ_{sh} (°)	93	93	93	93	93	93	153	153	153

The measured flow splits, α, and the measured sheet angles, θ_{sh}, are found in Tab. 2.4, below.

Table 2.4: Experimental measurements of initial sheet

	Basis Nozzle			Axisymmetric Tine			Axisymmetric Slot		
Injection Pressure, $P_{inj}(bar)$	1	2	3	1	2	3	1	2	3
Flow split, α	1.00	1.00	1.00	0.45	0.49	0.45	0.55	0.51	0.55
Sheet trajectory angle, θ_{sh} (°)	94	93	93	93	92	93	152	153	152

These measured values demonstrate a strong agreement between predicted and actual deflection outcomes for the BIM model. A comparison of the predicted and measured values can be seen in Fig. 2.3. The results show an average error in the flow split predictions of approximately 2% and a mean error in sheet angle predictions of approximately 0.4%. These predictions are within experimental error, indicating that the model assumptions are reasonable.

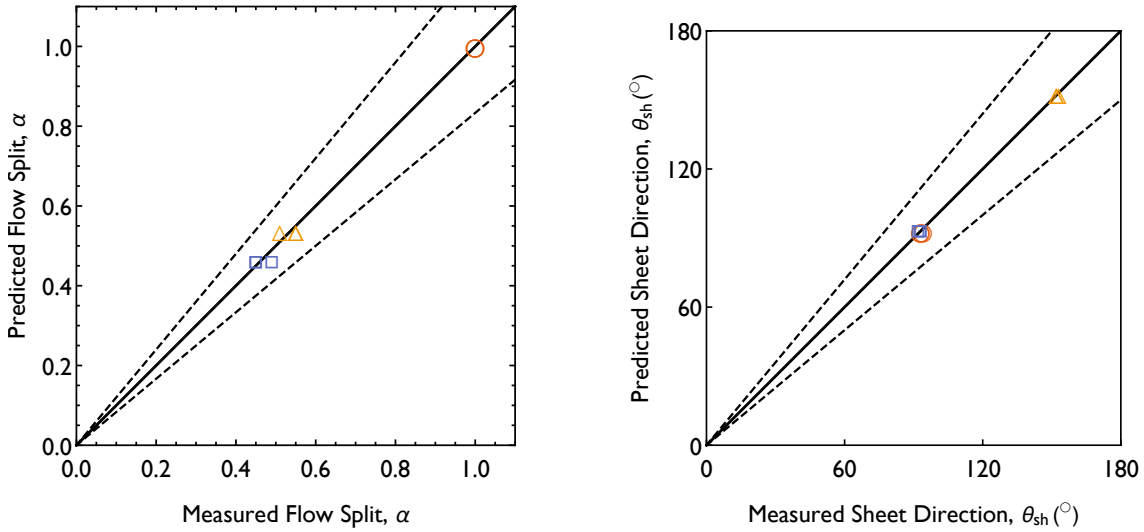

(a) (b)

Figure 2.3: A comparison of the measured and predicted (a) flow splits and (b) sheet velocity angles for the basis nozzle (circles), axisymmetric tine (squares), and axisymmetric slot (triangles), each at three pressures (1, 2 and 3 bar). Dashed lines represent deviations of 15%.

2.4 Summary

In this chapter the boundary integral method (BIM) model originally developed by Myers [12] was refined and used to predict the deflection phase of the Deflection Atomization Dispersion (DAD) framework. In this portion of the work the major contributions consisted of:

1. the formulation was made more general to better fit the inputs and outputs identified by the developed DAD framework;

2. the boundary conditions for the jet and the tine stream were both improved to

more closely approximate the physics;

3. and the numerical procedure was improved to speed computational time by a factor of ten [12].

Comparisons of modeled results to experimental measurements show remarkable agreement. The results show an average error in modeled flow split predictions of approximately 2% and a mean error in modeled sheet velocity angle predictions of approximately 0.4%.

The boundary integral method (BIM) model for calculating jet-deflector interactions offers one approach for predicting the deflection stage of the sprinkler spray. This method is, in principle, capable of capturing all features of even the most complex deflector geometries found in fire sprinklers, at only a fraction of the computational cost of traditional VOF calculations. This being said, the complexity of constructing boundary conditions limits its application.

Several assumptions are made in the modeling of the deflection of the spray. First, the slots of the deflector are assumed to be treated as thin orifices. This assumption is valid for the experimental sprinkler used, but may not hold for all traditional sprinklers. Additionally, all of the fluid flow is assumed to exit the sprinkler in thin fluid sheets. In an actual sprinkler, some of the flow leaves in jets and some atomizes immediately upon impact. These effects are small for our particular configuration, but could be larger in other sprinkler designs.

One strong advantage of the BIM is that it significantly reduces the computational cost for simple configurations.The speed of this model may prove suitable for quickly analyzing other geometric features of sprinkler deflectors as well. Changes to boundary conditions to account for the impact of the boss or of the angled tines require only minor adjustments to deflector and tine sheet boundary conditions. The addition of multiple slots is also possible. While beyond the scope of this work, these investigations could prove valuable in the design of future systems.

The axisymmetric case explored in this study effectively illustrates the impact of essential geometric details of sprinkler design on the flow a particular model is able to generate. The impact of slot area and slot centroid radius on the flow split and sheet velocity angle were explored numerically. These parameters, coupled with injection pressure and orifice diamter, are sufficient to predict sheet thickness and velocity. Sheet thickness and sheet velocity completely characterize the flow leaving the sprinkler deflector, as shown in Fig. 1.5 and given in Tab. 2.1, and are suitable as inputs for the atomization models, as outlined in Chapter 3.

Chapter 3: Atomization

3.1 Introduction

The atomization model is the second component of the Deflection Atomization Dispersion (DAD) framework for sprinkler spray prediction shown in Fig. 1.5. The goal of the atomization model presented in this chapter is to predict initial spray characteristics based on thin fluid sheet characteristics, as shown in Tab. 3.1. Deflection of sprinkler spray produces a set of thin fluid sheets, as discussed in Chapter 2. As these sheets spread and move radially outward, they undergo a flapping aerodynamic instability, breaking into ring-like ligaments and ultimately forming a spatially varying, polydispersed spray [14].

The sheet characteristics predicted by the deflection model (described in Chapter 2) inform the atomization model, which in turn predicts the initial spray that disperses throughout the protected space (described in Chapter 4). In this chapter, a linear stability theory model of thin fluid sheet atomization is developed and applied to the axisymmetric sprinklers described in Sec. 1.3. The atomization model outlined

Table 3.1: Atomization model inputs, parameters, and outputs

Model inputs	Sheet thickness, T_{sh} Sheet velocity, U_{sh}
Model parameters	N/A
Model outputs	Volume flux, $\dot{V}''$ Breakup radius, r_{bu} St. dev. of r_{bu}, σ_{rbu} Median diameter, d_{v50} Diameter distribution width, Γ Breakup velocity, U_{bu}

represents a refinement of the model initially developed by Ren et al. [14] and provides more detailed predictions of the initial spray than the previous global property atomization approach. Further, the atomization model has been leveraged to select atomization model outputs, shown in Tab. 3.1, more representative of the physical atomization process. The predicted initial spray characteristics are then compared to experimental measurements of the same axisymmetric sprinklers made using the University of Maryland Spatially-Resolved Spray Scanning System (4S).

The atomization of liquid sheets, such as those produced by fire sprinklers, was first studied in 1833 by Savart [32]. Savart observed breakup phenomena of radial expanding sheets produced by two co-axial colliding jets, noting that thin liquid sheets generated in the atmosphere formed unstable sinuous waves leading to their atomization. Weber [33] developed a more sophisticated model of this atomization accounting for the effect of liquid viscosity and density of the ambient gas. Hagerty and Shea [34] investigated the prevalence of this flapping sinusoidal instability as

compared to the dilatational instabilities commonly observed in Rayleigh [35] jet atomization. Hagerty found that when sheet thickness is small relative to wavelength, in contrast to jets, the sinusoidal instability dominates atomization.

Dombrowski et al. [36–38] studied the effect of ambient density on atomization in sheet-based fan-spray nozzle experiments. Ref. [38] determined that it was the fastest growing wave (the most unstable) that caused the sheet to break up. For inviscid sheets, the critical wavelength is given by $\lambda_{crit} = 4\pi\sigma/\rho_g U^2$, where σ is the surface tension of liquid, ρ_g is the density of ambient gas, and U is the characteristic velocity of the sheets.

The most comprehensive investigation of sheet atomization was performed by Clanet and Villermaux [39, 40]. Clanet and Villermaux described the atomization of a sheet formed by a jet of velocity U_j and diameter D_j impinging on an axisymmetric deflector. In these works, the authors identify two distinct regimes of atomization dependent on the jet Weber number, $We_j \equiv \rho_l U_j^2 D_j/\sigma$, where ρ_l is liquid density and σ is surface tension:

1. The smooth sheet regime is observed when jet Weber number is less than a critical Weber number on the order of 10^3. In this regime the liquid sheet remains smooth up to its edge, as illustrated in Fig. 3.1 (a).

2. The flapping regime is observed at Weber numbers greater than the critical jet Weber number where the edge of the sheet moves up and down, much like a

flag flapping in the wind (Fig. 3.1 (b)).

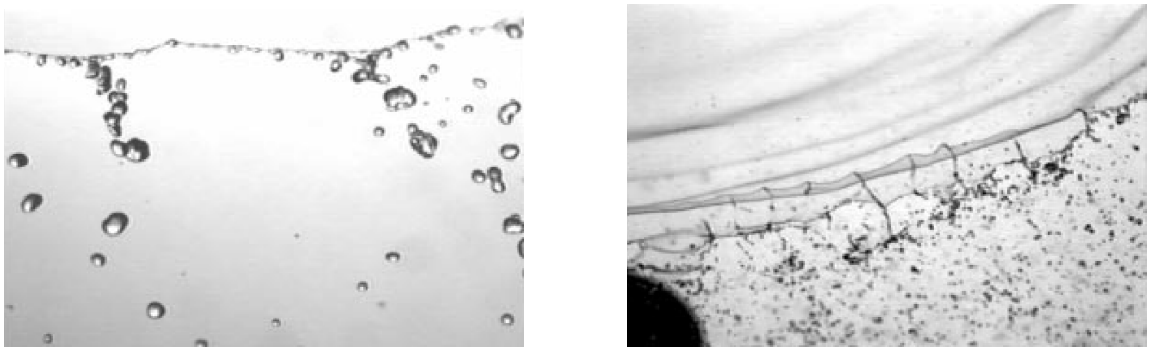

(a) Smooth Sheet (b) Flapping Sheet

Figure 3.1: Clanet and Villermaux observed two regimes of fluid sheet atomization: (a) smooth sheet and (b) flapping sheet, occurring at jet Weber numbers less than and greater than 10^3, respectively [39].

The sheets formed by a sprinkler spray exist exclusively above the critical jet Weber number of 10^3, and so may be treated for atomization as flapping sheets. The flapping sheet theory was applied to fire sprinklers by Ren et al. [14]. Ref. [14] divided the atomization process into a series of instability developments. First sheets leaving the fire sprinkler deflector develop instabilities that grow by Dombrowski's inviscid wave growth equations. These sheets then break apart into ligaments, which in turn develop instabilities, this time through the Rayleigh instability mechanism, and then break apart into droplets. Through this analysis, Ren developed scaling laws relating drop size and break up radius to sprinkler orifice size.

In the model presented by Ref. [14], the instabilities in the sheets are assumed to be sinusoidal in nature. This assumption can be verified by visual inspection of the

Figure 3.2: A shadowgraph image of a sheet from the axisymmetric sprinkler at the moment of atomization. Aerodynamic instabilities in the thin fluid sheet are sinusoidal, growing linearly until breakup.

sheet produced by the experimental sprinkler in this study, as seen in Fig. 3.2. While the amplitude of this disturbance is small relative to its wavelength, the instability of the expanding sheet can be described by linear instability theory. The wave growth rate is given by

$$\left(\frac{\partial f}{\partial t}\right)^2 + \frac{\mu_l}{\rho_l} n^2 \left(\frac{\partial f}{\partial t}\right) - \frac{2\left(\rho_g n U_{sh}^2 - \sigma n^2\right)}{\rho_l T_{sh}} = 0, \tag{3.1}$$

where f is a dimensionless wave growth, defined as $f = ln(A/A0)$, A is the wave amplitude, A_0 is the initial wave amplitude, t is time, μ_l is liquid viscosity, ρ_l is liquid density, n is the wave number defined as $n = 2\pi/\lambda$, λ is wavelength, ρ_g is

gas density, U_{sh} is the velocity of the sheet, assumed to be uniform, σ is the surface tension between the liquid and the gas, and T_{sh} is the thickness of the sheet. The first term in Eq. (3.1) is related to the inertial force, the second to the viscous force, and the third to the pressure and surface tension forces.

Sheet thickness, T_{sh}, and sheet velocity, U_{sh}, can be seen to govern wave growth rate. As shown in Chapter 2, these parameters are strongly dependent on sprinkler geometry and operating conditions and vary from sheet to sheet.

In Ref. [14] atomization characteristics are related to sprinkler orifice characteristics, providing scaling laws for global spray characteristics. Fire sprinkler sprays however, show tremendous spatial variation in spray properties, as other work by Ren et al. shows [7]. As a consequence of this, some spray detail is lost when spray properties are calculated globally. In this work, the scaling law approach is adapted to relate atomization to local sheet characteristics, rather than orifice characteristics, thus predicting local variations in spray characteristics. Further, a rigorous approach for the statistical description of the initial spay is developed and related to initial spray properties, shown in Tab. 3.1, reflective of the physical atomization process.

3.2 Methods

3.2.1 Modeling

The goal of a sprinkler atomization model is to determine spray characteristics just after atomization based on sheet characteristics determined either from experimental measurements or a deflection model, as detailed in Chapter 2. In the present work, a statistical description of the initial spray is derived based on the drop distribution function as presented in Ref. [16]. This formulation describes the initial spray in terms of spatially varying atomization radius, volume flux, drop size, and velocity. A linear instability analysis is then used to develop analytic scaling laws that predict these initial spray characteristics based on local sheet characteristics, sheet thickness and velocity. The resulting scaling laws are applicable to both the initial sheet description detailed in Chapter 2 and to more detailed VOF predictions of sprinkler spray formation. This analytic model is then applied to simulate the axisymmetric sprinkler described in Sec. 1.3 and compared to experimental measurements of the same.

3.2.1.1 A Statistical Description of the Initial Spray

To describe the complex and stochastic nature of fire sprinkler sprays, a statistical approach is needed. First proposed by Williams, the drop distribution function

characterizes the statistical characteristics of the spray [41].

A dilute spray is stochastic and locally unsteady. Despite this behavior, at sufficiently large spatial and temporal scales, a spray may be statistically described by a probability distribution function, f^*, called the drop distribution function [41]. This distribution function is defined such that the number of drops, N, in a phase space is assumed to be quasi-steady with time and is given as

$$\int_{[\vec{x},\vec{u},d]} f^*\left(\vec{x},\vec{u},d\right)\ d\vec{x}\ d\vec{u}\ dd = N, \tag{3.2}$$

where the phase space spans the volume space, $\vec{x}$, the velocity space, $\vec{u}$, and the drop diameter space, d. For convenience, the phase space over which the drop distribution function exists may vary, and is denoted by the variables in parentheses. As a result, the dimensions of f^* may vary depending on the defined phase space.

The drop distribution function description of a spray has the advantage of being conceptually consistent with the manner in which dilute sprays are measured, where the statistical characteristics of the spray are determined by measuring the spray in a limited volume of space over a sufficiently long period of time.

The evolution equation for the drop distribution function, called the spray equation, is given as

$$\frac{\partial f^*}{\partial t} = -\frac{\partial}{\partial d}\left(Df^*\right) - \overrightarrow{\nabla}_x \cdot \left(\vec{u}f^*\right) - \overrightarrow{\nabla}_u \cdot \left(\vec{a}f^*\right) + Q, \tag{3.3}$$

where

$$\vec{u} \equiv \frac{d\vec{x}}{dt}, \tag{3.4}$$

$$\vec{a} \equiv \frac{d\vec{u}}{dt}, \tag{3.5}$$

$$D \equiv \frac{dd}{dt}, \tag{3.6}$$

and Q accounts for the formation of new particles in a non-colliding spray.

The direct solution of the spray equation, Eq. (3.3), is non-trivial and computationally expensive with traditional finite-volume or finite difference techniques [42,43]. Instead, an alternative solution based on Lagrangian particle methods is commonly used to approximate the solution to Eq. (3.3). Lagrangian particle evolution methods are well developed and well understood [42,43]. The challenge for fire sprinkler sprays is describing the strong spatial variations measured in the initial spray and initializing Lagrangian particles to accurately represent these measurements. The injection of Lagrangian particles and their subsequent evolution is described in Chapter 4.

Initial sprays are generally described through a set of measured spray characteristics: volume flux, drop size, and velocity. Further, because strong spatial variations exist in typical sprinkler sprays, these spray characteristics must be measured locally.

These local spray characteristics can be related to the probability density function, f, to completely describe the spray.

The probability density function is directly related to the drop distribution function, Eq. (3.2), by

$$f_N\left(\vec{x},\vec{u},d\right) = f^*\left(\vec{x},\vec{u},d\right)/N, \tag{3.7}$$

where f_N describes the number fraction of drops in the multivariate phase space. The drop number probability density function, f_N, has the property

$$\int_{[\vec{x},\vec{u},d]} f_N\left(\vec{x},\vec{u},d\right)\ d\vec{x}\ d\vec{u}\ dd = 1. \tag{3.8}$$

The drop number probability density function, f_N, can be stochastically sampled to assemble a set of Lagrangian particles which is representative of local measurements.

3.2.1.2 Relationship to Measurement Topology

To facilitate conversion between measurements and modeling, the probability density function should reflect measurement topology and be directly related to measured characteristics.

To minimize the influence of the gas phase on the spray, the spray is measured as close to the sprinkler head as possible. However, the spray can only be measured

after complete atomization. Atomization occurs at a radius from the sprinkler head of between 0.1 and 0.4 m for most sprinklers [14]. Further, experimental observations have shown that the spray, when very near the sprinkler head, tends to move radially outwards from the sprinkler head [7]. As a result, measurements are generally made along a spherical surface with its origin on the sprinkler head.

The probability density function, f_N, given in Eq. (3.8), may be redefined in spherical coordinates as

$$\int_{[\vec{r},\vec{u},d]} f_N\left(\vec{r},\theta,\phi,\vec{u},d\right) r^2 \; dr \; d\Omega \; d\vec{u} \; dd = 1, \tag{3.9}$$

where $\vec{r}$ is the radial coordinate with an origin on the sprinkler head, θ is elevation angle, and ϕ is azimuthal angle, and where $d\Omega$ is the differential solid angle defined as

$$d\Omega = sin\left(\theta\right) \; d\theta \; d\phi. \tag{3.10}$$

For sprinkler sprays it is generally not the number of drops per unit volume but the volume flux at surfaces that governs sprinkler performance [1]. In keeping with this flux perspective, the drop distribution can be described in terms of a drop volume flux through a given surface (instead of a drop number in a volume) given by

$$\int_{[r,\theta,\phi,\vec{u},d]} f_V\left(r,\theta,\phi,\vec{u},d\right)\ r\left(\theta,\phi\right)^2\ dr\ d\Omega\ d\vec{u}\ dd = 1, \tag{3.11}$$

where

$$f_V\left(r,\theta,\phi,\vec{u},d\right) = f_N\left(r,\theta,\phi,\vec{u},d\right)\ \left(\vec{u}\cdot\hat{n}\right)\left(\pi/6\right)d^3/\dot{V}, \tag{3.12}$$

$\hat{n}$ is the vector normal to the surface, and

$$\dot{V} = \dot{N}(\pi d^3/6). \tag{3.13}$$

This function describes the density of water volume flux passing through a given angular position on the surface $r\left(\theta,\phi\right)$. While Eq. (3.11) is valid in general, the surface-flux-based formulation is especially well suited for describing the near-field spray characteristics on the surface where the measurements are made, $r_m\left(\theta,\phi\right)$, and correspondingly where Lagrangian particles may be initialized with known characteristics.

3.2.1.3 Relationship to Measured Properties

The volume-flux-based probability density function, f_V, is chosen to represent the initial spray because it conveniently reflects measurement methods. What remains is to relate the measured characteristics to the probability density function.

As previously mentioned, a spherical coordinate system was chosen to describe the spray because observation of the spray reveals that all drops in the initial spray tend to move radially away from the sprinkler head [7]. Because the velocity vector of the initial spray is assumed to be directed approximately radially out of the sprinkler head, it may be seen that

$$\vec{u} \cdot \hat{n} \approx |\vec{u}|, \tag{3.14}$$

where $\hat{n}$ is aligned with $\vec{r}$ at any given angular location. Additionally, drops of the same size tend to move at the same velocity, as seen in Fig. 3.16, which shows the drop size-velocity correlation for drops measured from the basis nozzle. As a result, drop velocity can be described as a characteristic velocity, $U_0(\theta, \psi, d)$.

If all drops are assumed to emerge from the surface $r_0(\theta, \psi)$ with an initial velocity, $U_0(\theta, \psi, d)$, the phase space of the volume flux probability density function, f_V, from Eq. (3.11), may be further restricted to vary only with angular location, (θ, ϕ), and drop size, d, as

$$\int_{[\theta,\phi,d]} f_V\left(\theta, \phi, d\right)\ r_0\left(\theta, \phi\right)^2\ d\Omega\ dd = 1. \tag{3.15}$$

This probability density function may be decomposed into the conditional probabilities

$$f_V(\theta,\phi,d) = f_{V,\Omega}(\theta,\phi)\ \ f_{V,d}(d|\theta,\phi), \tag{3.16}$$

where $f_{V,\Omega}(\theta,\phi)$ is the probability of finding volume flux from *any* drops emerging from the angular coordinates (θ,ϕ), and $f_{V,d}(d|\theta,\phi)$ is the probability of finding volume flux from drops of size d given an angular location (θ,ϕ).

To match the literature descriptions of drop size distributions and for convenience in initializing Lagrangian particles, the spray may also be described by a cumulative distribution function. The volume flux cumulative distribution function corresponding to the volume flux probability density function, f_V, is defined as

$$F_V(\theta,\phi,d) = \int_0^d \int_0^\phi \int_0^\theta f_V(\theta,\phi,d)\ \ r_0(\theta,\phi)^2\ \ d\Omega\ dd, \tag{3.17}$$

and may similarly be decomposed into conditional probabilities

$$F_V(\theta,\phi,d) = F_{V,\Omega}(\theta,\phi)\ \ F_{V,d}(d|\theta,\phi), \tag{3.18}$$

where $F_{V,\Omega}$ is the cumulative volume flow angular distribution, corresponding to the probability distribution function $f_{V,\Omega}$, and $F_{V,d}$ is the cumulative volume flow drop size distribution, corresponding to the probability distribution function $f_{V,d}$. The volume flow cumulative distribution function, $F_V(\theta,\phi,d)$, is constructed such that every phase space coordinate, (θ,ϕ,d), corresponds to a unique value of F_V between

0 and 1, which enables its later sampling to generate Lagrangian particles.

Both $F_{V,\Omega}$ and $F_{V,d}$ may be related to the measured volume flux and drop size, respectively, and then multiplied to provide a complete description of the flow, as per Eq. (3.18).

The cumulative volume flow angular distribution, $F_{V,\Omega}$, is related to the measured local volume flux normal to the initialization surface, $\dot{V}''(\theta,\phi)$, by Eq. (3.17) and

$$f_{V,\Omega}(\theta,\phi) = \frac{\dot{V}''(\theta,\phi)}{\dot{V}}.. \tag{3.19}$$

The cumulative drop size distribution, $F_{V,d}$, has been well explored in the literature and, for a typical fire sprinkler, can be well represented by a combination of log-normal and Rosin-Rammler distributions [44]. The cumulative volume fraction may be fit with two spatially varying parameters, median drop size, d_{v50}, and drop size distribution width, Γ. This distribution may be written as

$$F_{V,d}(d|\theta,\psi) = \begin{cases} \frac{1}{\sqrt{2\pi}} \int_0^d \frac{\Gamma}{1.15d'} e^{\left(\frac{-\ln\left(\frac{d'}{d_{v50}}\right)^2}{2\left(\frac{1.15}{\Gamma}\right)^2} \right)} dd' & d < d_{v50}, \\ 1 - e^{-0.693\left(\frac{d}{d_{v50}}\right)^{\Gamma}} & d \geq d_{v50} \end{cases} \tag{3.20}$$

For typical sprinklers, d_{v50} varies between 0.5 and 3 mm and Γ is between 2 and 3. Figure 3.3 shows $F_{V,d}$ and $f_{v,d}$ for the spray measured from the basis nozzle at 1 bar.

In this particular example, $d_{v50} = 1.7$mm and $\Gamma = 2.3$.

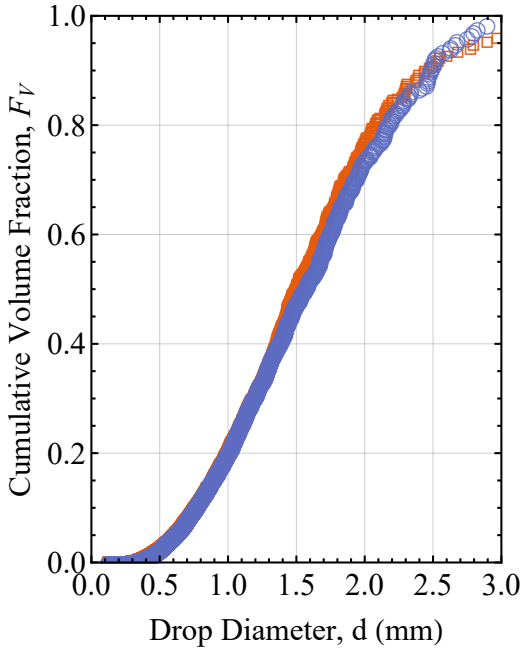

Figure 3.3: Cumulative volume fraction vs. drop diameter for drops from the basis nozzle sheet at 1 bar, measured (red squares) and predicted (blue circles).

Using the measured values of volume flux, drop size, and drop velocity for any sprinkler, initial spray particles may be generated. It is impractical to directly specify the drop velocity-size correlation reflected in Fig. 3.4. One traditional approach to simplifying this distribution is to assume that all drops emerge at a single characteristic velocity, $U_m(\theta, \phi)$, usually given as some fraction of the Bernoulli velocity, and are initialized along the measurement surface, $r_m(\theta, \phi)$. Figure 3.5 shows 2,000 drops generated with this assumption.

A weakness of this assumption is that it fails to capture the initial decelera-

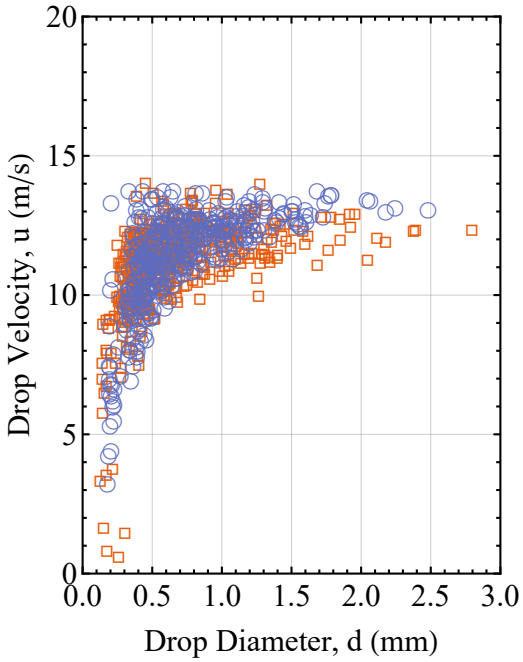

Figure 3.4: Drop velocity magnitude vs. drop diameter for drops from the basis nozzle sheet at 1 bar, measured (red squares) and predicted (blue circles).

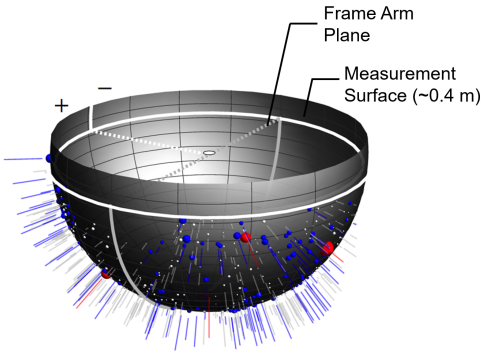

Figure 3.5: Drops representing the initial spray; red $d > 1.5$mm, blue $0.5 < d < 1.5$mm, and white $d < 0.5$mm; rays are scaled with velocity.

tion of the drops responsible for much of the transfer of spray momentum to the gas phase. An examination of atomization theory and local drop size-velocity correlations

suggests that immediately after atomization all local drops are moving at identical velocities. The measured drop size-velocity correlation may be fit to a breakup radius and initial velocity magnitude, where the drops are assumed to slow purely due to air drag. In Fig. 3.6, the calculated breakup radius, $r_{bu}(\theta, \phi)$, and breakup velocity, $U_{bu}(\theta, \phi)$, are used to initialize 2,000 drops. This alternative assumption both captures drop size-velocity correlation and allows for a more accurate simulation of the coupling between the initial spray and the gas phase.

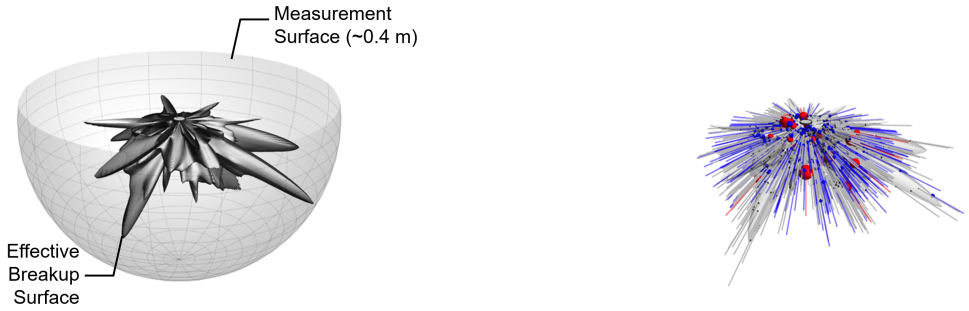

(a) (b)

Figure 3.6: Effective sheet breakup surface (a) without drops and (b) with drops; red $d > 1.5$mm, blue $0.5 < d < 1.5$mm, and white $d < 0.5$mm; rays are scaled with velocity.

The initial spray may thus be described by the volume flow cumulative volume fraction, $F_V(\theta, \phi, d)$, where F_V is given, as in Eq. (3.16), by the product of $F_{V,\Omega}$ and $F_{V,d}$, given by Eqs. (3.19) and 3.20, respectively, where all drops at a given angular location are assumed to originate from an initial breakup radius $r_b u(\theta, \phi)$, with a velocity magnitude, $U_b u(\theta, \psi, d)$, and a velocity angle aligned with the radial direction at a given angular location. $F_V(\theta, \phi, d)$ provides a detailed description of the

spray grounded in spray theory and measurements, and can be used for initializing Lagrangian particles for the numerical simulation of spray dispersion, as discussed in Chapter 4.

3.2.1.4 Atomization Scaling Laws

The initial spray characteristics described in Sec. 3.2.1.1 may be predicted from an analysis of the behavior of the flapping sheet that produces them. As the sheet undergoes its flapping atomization, it continues to move radially outward but begins to spread, as seen in Fig. 3.7 [14]. This flapping motion occurs as a result of the growth of instabilities, as described in Eq. (3.1).

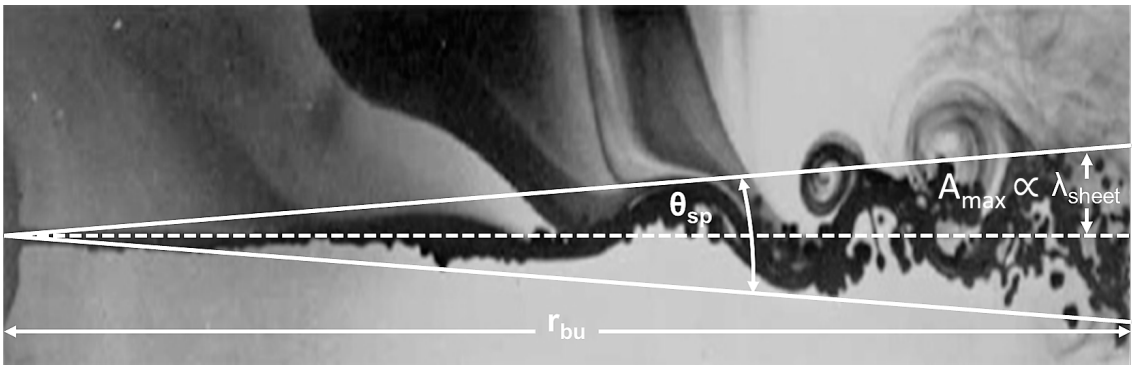

Figure 3.7: After leaving the deflector, thin fluid sheets undergo aerodynamic instabilities, spread, and break up into fragments [38].

All initial spray characteristics are determined by sheet characteristics at the location of breakup. To predict the initial spray, the breakup radius, r_{bu}, must first be determined.

3.2.1.5 Breakup Radius

To simplify analysis, the invicid form of Eq. (3.1) is

$$\frac{\partial f}{\partial t} = \left(\frac{2\left(\rho_g n U_{sh}^2 - \sigma n^2\right)}{\rho_l T_{sh}} \right)^{\frac{1}{2}}. \tag{3.21}$$

The wave with the maximum growth rate can be determined as

$$n_{crit} = \frac{2\pi}{\lambda_{sh}} = \frac{\rho_g U_{sh}^2}{2\sigma} = \frac{\rho_g}{\rho_l} \frac{We_{sh}}{2T_{sh}}, \tag{3.22}$$

where the sheet Weber number is defined as

$$We_{sh} = \rho_l U_{sh}^2 T_{sh} / \sigma. \tag{3.23}$$

The wave growth rate is then given by

$$\frac{\partial f}{\partial t} = \frac{\rho_g}{\rho_l} \frac{U_{sh}}{T_{sh}} We_{sh}^{1/2}. \tag{3.24}$$

Recognizing that the instantaneous radial growth of the wave is $dr = U_{sh} dt$ we find

$$\frac{\partial f}{\partial r} = \frac{\rho_g}{\rho_l} \frac{1}{T_{sh}} We_{sh}^{1/2}. \tag{3.25}$$

The instability grows according to Eq. (3.25) until the dimensionless wave amplitude reaches some critical value, f_0, at which point the sheet breaks apart into ligaments [14]. The radius at which the sheet reaches this critical value is called the breakup radius, and Eq. (3.25) can be solved to show

$$\frac{r_{bu}}{T_{bu}} = C_{rbu}\left(\frac{\rho_l}{\rho_g}\right) f_0 \left(We_{sh}\right)_{bu}^{-1/2}, \tag{3.26}$$

where C_{rbu} is a constant, and T_{bu} is the sheet thickness, T_{sh}, at the breakup radius, r_{bu}. In the present work, it was observed that $C_{rbu} \approx 0.475$. This value was calculated based on correlations for sheet thickness, as sheet thickness was not directly available in the current experimental data. This value may need to be tuned to particular definitions of sheet thickness for other models.

A critical observation is that the breakup radius scales as $We_{sh}^{-1/2}$, unlike the work presented by Ren et al., where the breakup radius scales as $We_0^{-1/3}$ [14]. This result is due to a different definition of the Weber number. In the analysis of Ref. [14], the Weber number is the orifice Weber number, or the Weber number of the initial impinging jet, given by $We_0 = \rho_l U_j^2 D_0/\sigma$, where U_j and D_0 are the velocity and the diameter of the impinging jet, respectively. In the current analysis, the Weber number is the sheet Weber number given in Eq. (3.23).

The breakup radius defined in Eq. (3.26) can be related to the sheet Weber number by recognizing that sheet thickness and velocity can be related to the jet

diameter and velocity from Eq. (2.3) with the inclusion of the flow split, α. The new equation for sheet thickness is given as $T_{sh} = \alpha\beta D_0/8r_{sh}$, and the sheet velocity magnitude is given by $U_{sh} = U_j/\beta$, where α is the flow split, or the fraction of the total flow expected in a sheet from the total flow of a basis nozzle, and where β is the sheet thickening factor.

Using the above analysis, the breakup radius may be related to the orifice characteristics and the flow split by

$$\frac{r_{bu}}{D_0} = \left(\frac{3\rho_l}{2\rho_a} f_0\right)^{2/3} \left(\beta^2\alpha\right)^{1/3} We_0^{-1/3}, \tag{3.27}$$

which agrees with the scaling identified in previous work by Ren [14].

Work by Wu et al. [45] suggests that the magnitude of the critical wave amplitude, represented by f_0, is not a single value but rather a distribution of values. Experimental evidence collected in this work suggests that this fluctuation can be captured by assuming that f_0 is normally distributed, with mean value, μ_{f0}, and standard deviation, σ_{f0}.

This critical wave amplitude, f_0, is difficult to determine from first principles. Instead it must be calculated from experiments. The normal distribution of f_0 can be observed by examining the mean and standard deviation of the breakup radius, r_{bu}, coupled with observations of drop size. The standard deviation of drop size, σ_{rbu}, may be related to the standard deviation of f_0 by the proportionality

$$\frac{\sigma_{rbu}}{r_{bu}} = \left(\frac{\sigma_{f0}}{\mu_{f0}}\right)^{2/3}, \tag{3.28}$$

following from Eq. (3.27).

Depending on the fidelity of the sheet dispersion information available, either Eq. (3.26) or Eq. (3.27) may be used. With a detailed sheet dispersion model, such as a VOF model, Eq. (3.26) can be used to determine the point of breakup. In the case of a lower fidelity description for the sheets, such as the sheet predictions from the boundary integral method (BIM) deflection model outlined in Chapter 2, Eq. (3.27) must be used.

The above sheet breakup analysis may be used to derive the remaining information to quantify the spray: volume flow, spatial variation, drop size, and velocity.

3.2.1.6 Volume Flow

Volume is conserved during atomization, and the spray volume flow from a single sheet is the same as the volume flow of the sheet. For an axisymmetric sheet

$$\dot{V}_{sh} = 2\pi T_{sh} U_{sh} \tag{3.29}$$

or, using the flow split description in Sec. 2.1,

$$\dot{V}_{sh} = \alpha \ \pi U_j D_0^2/8. \tag{3.30}$$

Volume flow is typically given by a volume flux, $\dot{V}^{"}$, generally as a function of the elevation and azimuthal angles, θ and ϕ, respectively, defined in a spherical coordinate system with the sprinkler at the origin. This volume flux is related to the total volume flow by

$$\dot{V}^{"}(\theta,\phi) = \frac{\dot{V}_{sh}\ f_{V,\Omega}(\theta,\phi)}{r(\theta,\phi)^2\ sin(\theta)}, \tag{3.31}$$

where $f_{V,\Omega}(\theta,\phi)$ is the volume flux probability density function describing the spatial distribution of volume flux.

The spatial distribution of the volume flux is dependent on the trajectory of the sheets and the spread of the spray due to the flapping motion and subsequent atomization. Over the short length scales of atomization, the impact of gravity can be neglected. As a result, the core of the spray forms and is directed radially outward from the sprinkler deflector in the direction the sheet left the sprinkler deflector, θ_{sh}. For the axisymmetric sprinkler, this angle has no azimuthal dependence, and sheet direction can be described purely by elevation angle. This elevation angle is the same as the velocity angle for the tine and slot sheets in Chapter 2.

As a result of the flapping motion of the sheets, a certain spreading occurs, distributing the volume flux over a given angular region, θ_{sp}. The size of this spread angle, as seen in Fig. 3.7, is related to the ratio of the maximum instability amplitude A_{max}, over instantaneous breakup radius, r_{bu}. In research by Crapper, Dombrowski,

and Pyott [46] the maximum amplitude of the wave is proportional to the critical wavelength of the sheet, λ_{sh}. Drops are assumed to initially proceed in a straight line following atomization. As a result, the width of a drop volume flux packet, which may be thought of as a single broken ligament, is proportional to λ_{sh}/r_{bu}, where r_{bu} is the instantaneous atomization radius. When the flapping sheet breaks up at small radii, the volume flux is compressed to a small region. At large breakup radii, the flapping instabilities have grown further, and the volume flux is spread over a wider region. As a result, the spread angle reflects not only the magnitude of the instantaneous breakup, but also the spread resulting from variations in breakup radius. The spread angle is thus given by

$$\theta_{sp} \propto A_{max}/\sigma_{rbu} \approx C_{\theta sp}\lambda_{sh}/\sigma_{rbu}, \tag{3.32}$$

where $C_{\theta sp} \approx 28$ from experimental data when θ_{sp} is given in degrees, and $C_{\theta sp} \approx 0.5$ when θ_{sp} is given in radians.

This spread angle may be taken as a characteristic angle over which the spray is distributed. The volume flux probability density function, $f_{V,\Omega}(\theta, \phi)$, for an axisymmetric sprinkler may assumed to be independent of the azimuthal angle, ϕ, and to be a normal distribution with respect to elevation angle, θ, with a mean value of the sheet velocity angle, θ_{sh}, and a standard deviation of the sheet spread angle, θ_{sp}, written as

$$f_{V,\Omega}(\theta) = \frac{1}{\theta_{sp}\sqrt{2\pi}} e^{-\frac{(\theta-\theta_{sh})^2}{2\theta_{sp}^2}}. \tag{3.33}$$

The volume flux from a sheet may then be calculated from Eq. (3.31) and Eq. (3.33), where breakup radius, r_{bu}, is calculated from Eq. (3.27), the sheet velocity angle, θ_{sh}, is taken from the deflection model, and sheet spread angle, θ_{sp}, is calculated from Eq. (3.32). The volume flux from the total spray is simply the sum of the volume flux from all sheets.

3.2.1.7 Drop Size

The atomizing sheet breaks up, first into ring-like ligaments which then quickly break up into drops. Drop size may be assumed to be proportional to the ligament diameter, d_{lig}, which is in turn related to breakup distance and sheet thickness [14]. The characteristic non-dimensional drop diameter, d/D_0, as given by Ren, is

$$\frac{d}{D_0} \propto (f_0\ We_0)^{-1/3}. \tag{3.34}$$

Equation 3.34 may be related to the breakup radius, Eq. (3.27), to find that

$$\frac{d}{r_{bu}} \approx C_d f_0^{-1}, \tag{3.35}$$

where C_d is a constant corresponding to various definitions of the characteristic drop

size. For the d_{v50}, $C_d \approx 0.08$.

Fire sprinkler sprays are highly polydispersed (i.e., they consist of drops having a wide range of diameters). This variation in diameter influences sprinkler spray transport and interaction with the continuous phase, and must be accounted for to accurately model sprinkler spray behavior. Spray drop size distributions are typically measured through laser diffraction or shadowgraph methods, and described by a cumulative volume fraction [7, 11].

The cumulative drop size distribution function, $F_{V,d}$, is a function of diameter whose value at a given diameter corresponds to the fraction of the total spray volume flux contained in drops with a diameter less than or equal to the given diameter passing through a surface. For a typical fire sprinkler, the cumulative drop size distribution function can be well represented by a combination of log-normal and Rosin-Rammler distributions, as shown in Eq. (3.20) [44]. The cumulative volume fraction may be fit with two parameters, median drop size, d_{v50}, and drop size distribution width, Γ. For typical sprinklers, d_{v50} varies from 0.5 to 3 mm, and Γ is between 2 and 3.

In this formulation, Eq. (3.35) corresponds to a median drop size, d_{v50}, and is assumed to be uniform for the spray from any particular sheet. The distribution width, Γ, is determined by fluctuations in the initial disturbances of the sheet. As a result, Γ may be related to the normal distribution of f_0 as

$$\frac{1}{\Gamma} = \left(\frac{\sigma_{f0}}{\mu_{f0}}\right)^{2/3}. \tag{3.36}$$

This relationship can be seen to follow the same scaling as σ_{rbu}, given in Eq. (3.28), which follows from the scaling for atomization distance, Eq. (3.27).

3.2.1.8 Drop Velocity

Observation of the initial spray reveals that all drops in the initial spray move radially away from the sprinkler head [7]. Further, it is reasonable to assume that the atomization process has only a minimal impact on momentum. With this in mind, at the breakup radius, r_{bu}, all drops, regardless of size, move radially outward with velocity magnitude given by the sheet velocity, $U_{sh} = U_{bu}$, and velocity angle given as radially outward from the sprinkler.

The initial velocity of all water is the jet velocity, U_j, which is subsequently slowed by the drag effects produced while interacting with the air and the deflector. Experimental observations suggest that the initial slowing of the sheet can be completely accounted for by the sheet thickening factor applied across the deflector, so that $U_{bu} = U_j/\beta$.

The spray characteristics predicted above are sufficient to completely describe the initial spray, as demonstrated in Sec. 3.2.1.1. Further, the only information necessary to predict these spray characteristics are the characteristics of the thin

fluid sheets produced by deflection.

3.2.2 Experiments

Optical measurements of the near-field spray were made using the 4S optical patternation system; a laser shadowgraphy system that provides information on drop size, velocity, and atomization location in the near-field of the spray. Approximately 30,000 images of the spray were recorded at a radius of 0.4 m from the sprinkler head and at the approximate elevation angles of each sheet, $\theta \approx 95^\circ$ and $\theta \approx 155^\circ$). These images were then analyzed to provide statistical information on drop size, drop velocity, and breakup radius. The model predictions of volume flux were verified through mechanical measurements, as described in Sec. 2.2.2. Additionally, breakup radius was also measured through visual inspection of the sheet using the shadowgraphy system.

The LaVision shadowgraph system consists of a jointly controlled laser and camera, and was used to conduct two-dimensional particle tracking velocimetry (PTV) measurements. For these measurements, a diffuse laser back light is flashed to "freeze" the drops in an image. An ImagePro X camera was used and fitted with a Nikon AF DC-Nikkor 50 mm f/2D lens. The camera lens and 56 mm diameter laser diffuser were positioned with a separation distance of 0.1 m. The circular field of view was approximately 26 mm in diameter and the depth of field was approximately 25

mm, yielding a cylindrical measurement volume. The 4-megapixel camera provided resolution sufficient to measure drops as small as 0.08 mm in diameter.

In shadowgraph PTV measurements, a pair of images is taken, separated by a known time delay, as seen in Fig. 3.8. Drops located in both frames of the image pair are recorded with described drop diameter and velocity calculated from the change in position of the drop between the two images. Over a sufficiently large number of image pairs, statistics for drop size and velocity distributions can be calculated for any given location.

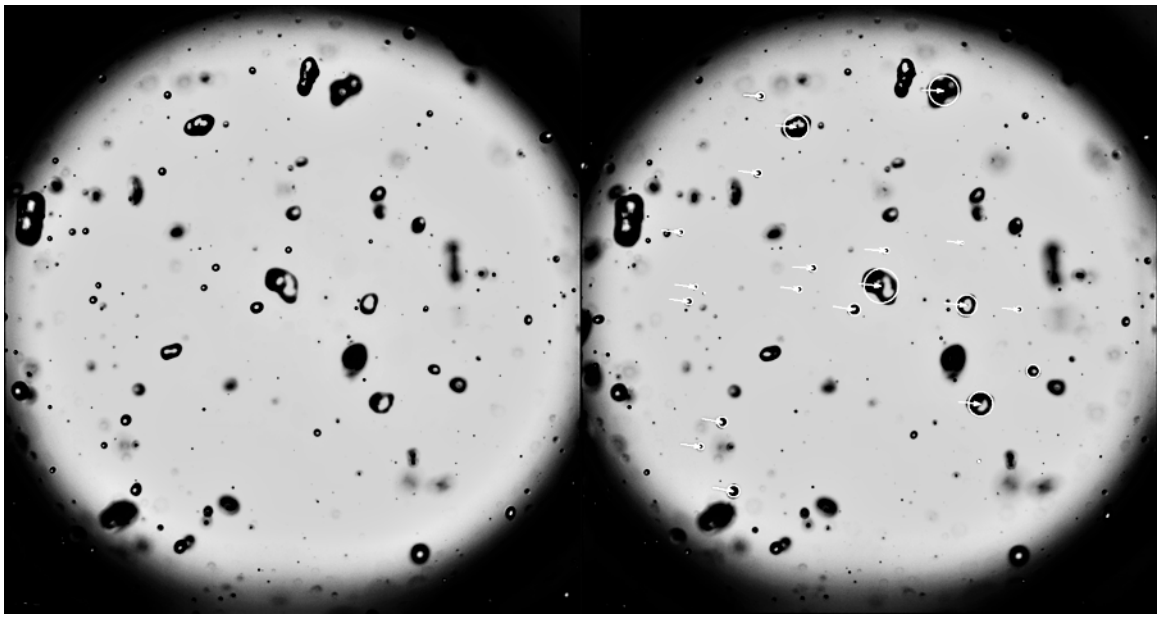

Figure 3.8: A pair of successive images is captured with only a brief delay in the shadowgraph system. A comparison of the images yields a list of drops along with their diameters and velocities, which may in turn be used to calculate initial spray statistics. Yellow circles and arrows in the image on the right show identified drops and their velocities.

In the current experimental setup, the sprinkler slowly rotates as the camera photographs large numbers of drops. The LaVison processing system exports a list of drops (with their diameters and velocities) and the angular location in which these drops were measured. A script was then used to bin sets of drops based on angular location. A collection of drops from the basis nozzle sheet, at 1, 2, and 3 bar pressure, is shown in Fig. 3.9.

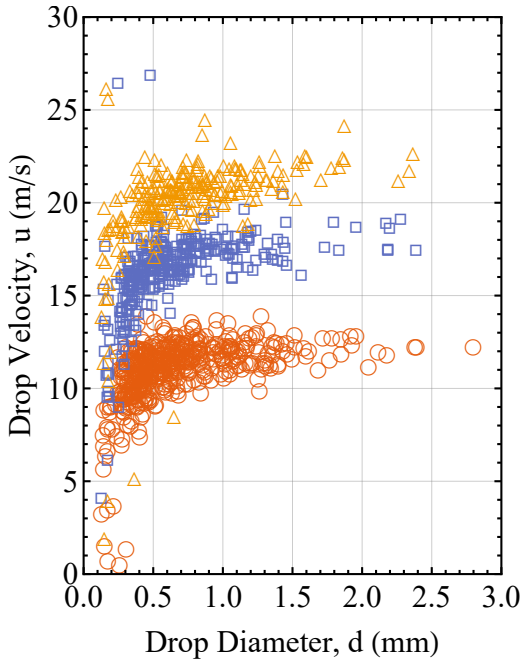

Figure 3.9: Drop velocity magnitude vs. drop diameter for drops from the basis nozzle sheet at 1 bar (red circles), 2 bar (blue squares), and 3 bar (yellow triangles).

Figure 3.9 shows that drops with larger diameters are consistently measured with a larger velocity magnitude than those with smaller diameters. Atomization theory suggests that all drops from a given sheet, upon atomization, should have

the same velocity magnitude. However, it is important to recall that drops are not experimentally measured at the atomization location, but rather at some remote radial distance. This velocity difference can then be attributed to the preferential slowing of smaller drops by drag interactions with the air.

The drop size-velocity distribution seen for each pressure in Fig. 3.9 may be fitted to an initial drop velocity, U_{bu}, and a distance traveled, which is a function of measurement radius. To verify the calculated breakup radius, r_{bu}, the sheets were also visually inspected with the shadowgraphy system as seen in Fig. 3.10. The local breakup radius varies and can be characterized as a normal distribution with a mean and standard deviation, r_{bu} and σ_{rbu}, respectively. The mean value of r_{bu} was approximated as the location at which the sheet could be seen to be intact in approximately 50% of the examined frames.

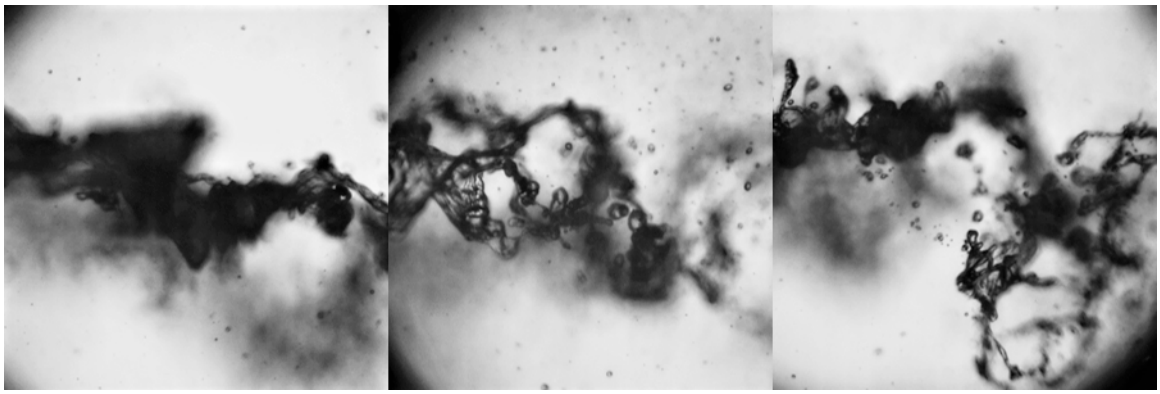

Figure 3.10: To verify the calculated breakup radius, r_{bu}, the sheets were visually inspected with the shadowgraph system. In the left frame the sheet appears intact; in the center frame, it is in the process of atomizing; and in the right frame, atomization has already occured.

The drop diameter distribution may also be determined from shadowgraphy images. At each angular location, the statistical median drop diameter, d_{v50}, and distribution width, Γ, for the measured drops were fitted to the log-normal/Rosin-Rammler distribution (Eq. (3.20)), as shown in Fig. 3.11. The results of these statistical analyses are shown in Sec. 3.3.

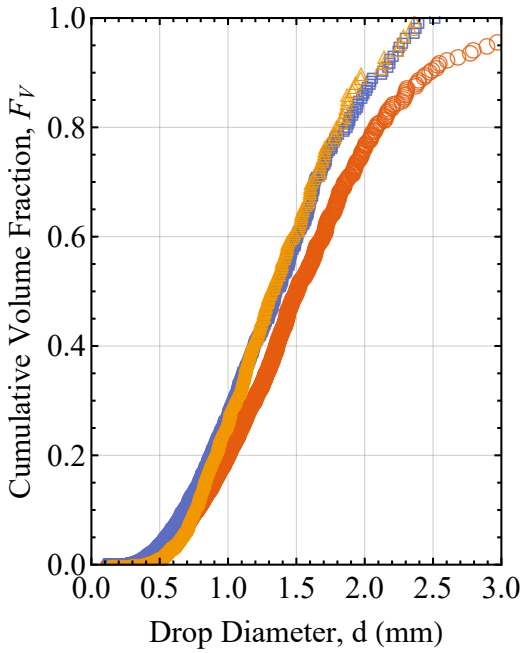

Figure 3.11: Cumulative volume fraction vs. drop diameter for drops from the basis nozzle sheet at 1 bar (red circles), 2 bar (blue squares), and 3 bar (yellow triangles).

3.3 Results

The scaling laws derived in Sec. 3.2 provide a complete description of the initial fire sprinkler spray. These scaling laws were applied to the results of the boundary

integral method (BIM) deflection model outlined in Chapter 2 in order to make predictions of initial spray produced by the axisymmetric sprinklers described in Sec. 1.3. These results are then compared to experimental measurements of made with the University of Maryland Spatially-resolved Spray Scanning System (4S) optical patternation.

Table 3.2 shows the results from the atomization scaling law predictions along with model predictions of flow split, α, and sheet trajectory angle, θ_{sh}, from Chapter 2 (also shown for the reader's convenience). The results of the experimental measurements are presented in Tab. 3.3.

Table 3.2: Model predictions of initial spray characteristics

	Basis Nozzle			Axisymmetric Tine			Axisymmetric Slot		
Injection pressure, P_{inj} (bar)	1	2	3	1	2	3	1	2	3
Flow split, α	1.0	1.0	1.0	0.46	0.46	0.46	0.54	0.54	0.54
Sheet trajectory angle, θ_{sh} (°)	93	93	93	93	93	93	153	153	153
Spread angle, θ_{sp} (°)	6.0	3.8	2.9	7.1	4.3	3.4	6.6	4.2	3.2
Breakup radius, r_{bu} (m)	0.19	0.15	0.13	0.15	0.12	0.10	0.16	0.12	0.11
St. dev. of r_{bu}, σ_{rbu} (m)	0.07	0.06	0.05	0.06	0.05	0.04	0.07	0.05	0.05
Median diameter, d_{v50} (mm)	1.7	1.5	1.3	1.5	1.2	1.0	1.6	1.2	1.1
Diameter distribution width, Γ	2.7	2.7	2.7	2.4	2.4	2.4	2.4	2.4	2.4
Breakup velocity, U_{bu} (m/s)	13.8	19.5	23.9	13.8	19.5	23.9	13.8	19.5	23.9

Based on these results, the critical wave amplitude, f_0, can be calculated from Eq. (3.26) with a mean value of 9.5 for the basis nozzle, axisymmetric tine, and axisymmetric slot sprays. The standard deviation of the critical wave amplitude, σ_{f0}, is calculated by Eq. (3.28) as 2.2 for the basis nozzle spray and 2.6 for the axisymmetric

Table 3.3: Experimental measurements of initial spray characteristics

	Basis Nozzle			Axisymmetric Tine			Axisymmetric Slot		
Injection pressure, P_{inj} (bar)	1	2	3	1	2	3	1	2	3
Flow split, α	1.0	1.0	1.0	0.45	0.49	0.45	0.55	0.51	0.55
Sheet trajectory angle, θ_{sh} (°)	94	93	93	93	93	92	152	153	152
Spread angle, θ_{sp} (°)	5.7	4.1	3.6	6.5	4.0	3.0	6.0	4.2	3.8
Breakup radius, r_{bu} (m)	0.19	0.15	0.14	0.15	0.11	0.1	0.17	0.13	0.11
St. dev. of r_{bu}, (m)	0.07	0.06	0.05	0.06	0.05	0.04	0.07	0.05	0.04
Median diameter, d_{v50} (mm)	1.7	1.4	1.3	1.5	1.4	1.2	1.5	1.4	1.1
Diameter distribution width, Γ	2.3	2.3	2.6	2.4	2.3	2.7	2.3	2.2	2.5
Breakup velocity, U_{bu} (m/s)	13.8	19.9	23.9	13.4	19.2	22.9	14.1	20.0	22.3

tine and axisymmetric slot sprays.

These measured results show strong agreement with scaling law predictions. Figure 3.4 shows drop velocity magnitude vs. drop diameter for the basis nozzle spray at 1 bar for measured drops and drops stochastically generated from the scaling law predictions. A similar comparison may be performed with the same data, as seen in Fig. 3.3, comparing the measured predicted cumulative volume flux for the basis nozzle spray.

To best examine the results, comparisons between predicted statistical spray characteristics (Tab. 3.2) and measured spray characteristics (Tab. 3.3) were performed. The comparisons are presented in the same order as the models were outlined above.

3.3.0.1 Breakup Radius

The predictions and experimental measurements of mean breakup radius, r_{bu}, and the standard deviation of the breakup radius, σ_{rbu}, are compared in Fig. 3.12 (a) and (b), respectively. For both, average error is approximately 4%.

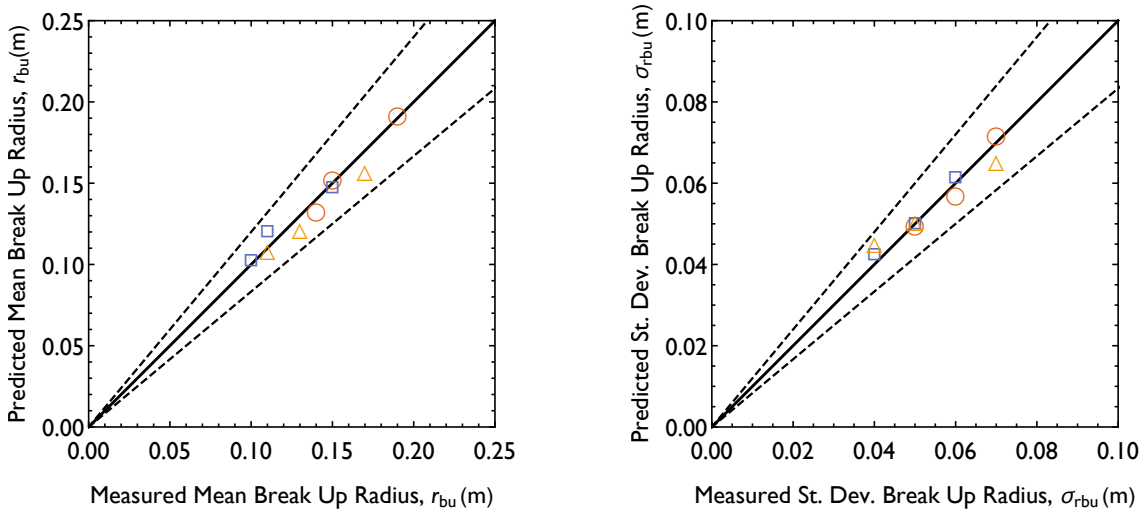

(a) (b)

Figure 3.12: A comparison of the measured and predicted mean breakup radius (a) and standard deviation of the breakup radius (b) for the basis nozzle (red circles), axisymmetric tine (blue squares), and axisymmetric slot (yellow triangles), each determined at three pressures (1, 2 and 3 bar).

3.3.0.2 Volume Flow

The total volume contained in the each sheet is dependent on the flow split, α, while the spatial distribution of this volume flow, or the near-field volume flux of the spray, is determined by the sheet trajectory angle, θ_{sh}, and the sheet spread angle,

θ_{sp}. Both flow split and sheet trajectory angle measurements and predictions were examined in Chapter 2, with predictions found to deviate from measured results by 2% and 0.5% respectively.

The predictions and experimental measurements of sheet spread angle are compared in Fig. 3.13. The average error is approximately 9%. Sheet spread angle has values ranging from approximately 2° to 7°. It is difficult to measure this sheet spread angle with a precision finer than 1°. As a result, it is difficult to assess whether the apparent accuracy of the model is real, or merely the result of measurement error.

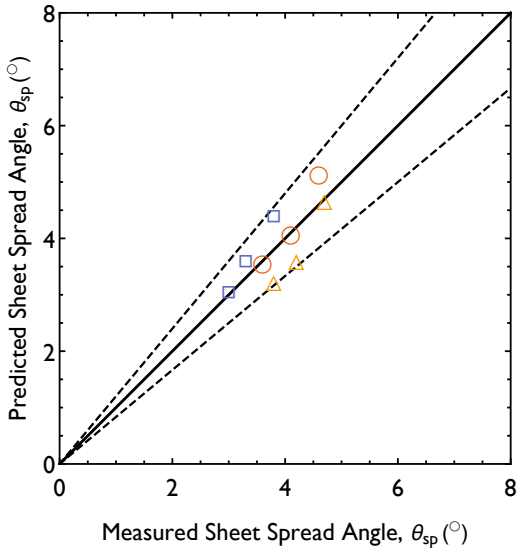

Figure 3.13: A comparison of measured and predicted sheet spread angle, θ_{sp}, for the basis nozzle (red circles), axisymmetric tine (blue squares), and axisymmetric slot (yellow triangles), each determined at three pressures (1, 2 and 3 bar).

3.3.0.3 Drop Size

The predictions and experimental measurements of median drop diameter, d_{v50}, and the drop distribution width, Γ, are compared in Fig. 3.14 (a) and (b), respectively. For both, average error is approximately 8%.

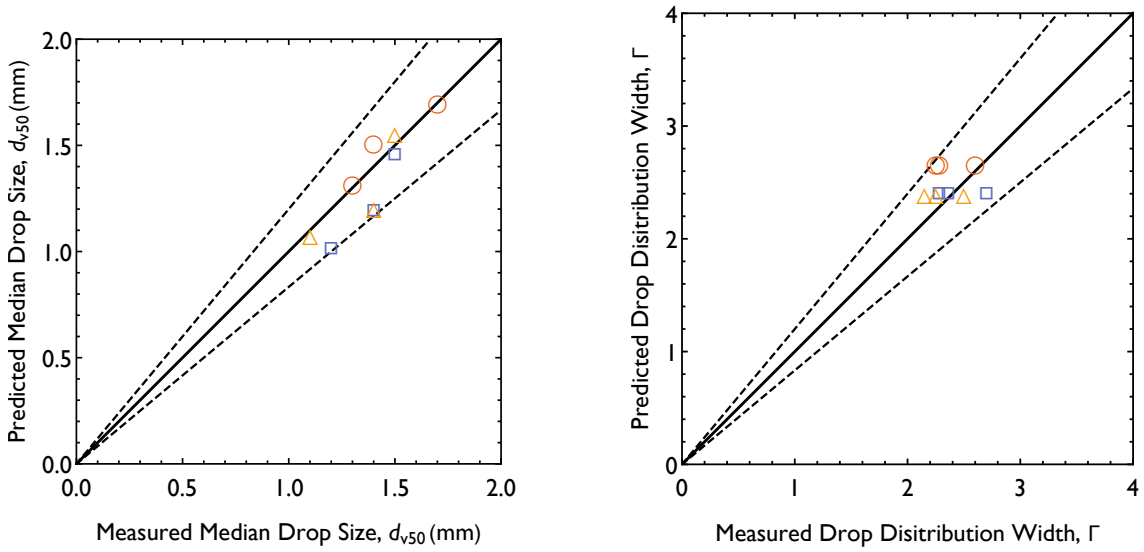

(a) (b)

Figure 3.14: A comparison of the measured and predicted median drop diameter (a) and drop distribution width (b) for the basis nozzle (red circles), axisymmetric tine (blue squares), and axisymmetric slot (yellow triangles), each determined at three pressures (1, 2 and 3 bar).

It can be observed that the drop distribution width, Γ, is very insensitive to sprinkler configuration, with all pressures and sheet thicknesses taking on values of approximately 2.4. This result is consistent with earlier work [7].

In previous work by Ren [4], the median drop diameter, d_{v50}, was carefully measured for several basis nozzles of varying orifice diameters, as well as the tine

and slot sheets from two standard nozzles with different orifice diameters. In all cases, measurements were conducted at various pressures. Because orifice diameter, operating pressure, flow split, and critical wave amplitude, f_0, were recorded, the scaling laws developed in this work (Eqs. (3.27) and (3.35)) may also be used to predict these historical results. A comparison between the predicted and measured d_{v50} from the current work, as well as from Ref. [4], is shown in Fig. 3.15.

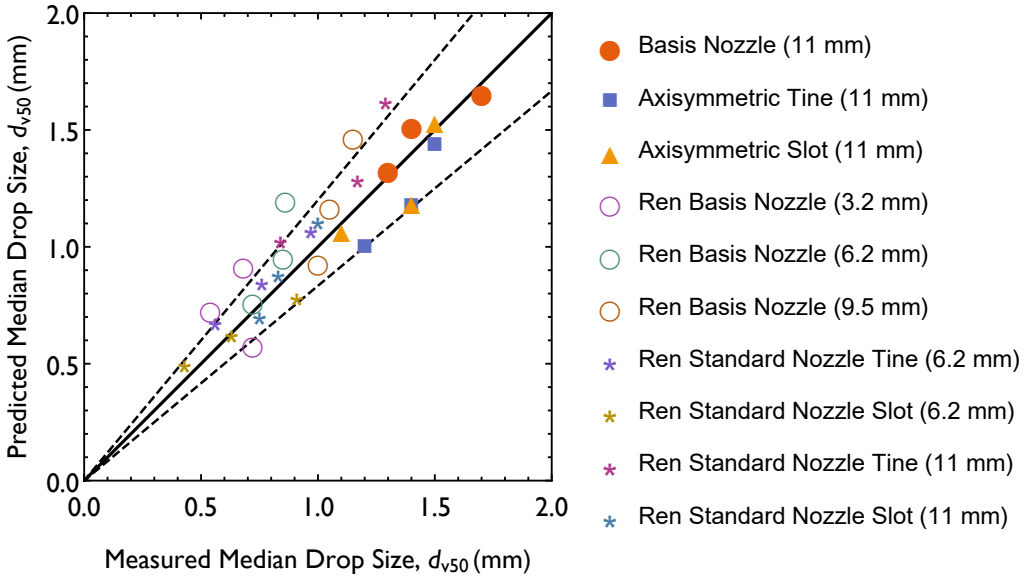

Figure 3.15: A comparison of the measured and predicted median drop size, d_{v50}, from current and historical measurements [4].

Ref. [4] noted that basis nozzles measured at low Reynolds numbers seemed to produce drops with diameters that scale with $We^{-1/6}$, in contrast to those measured at higher Reynolds numbers or standard nozzles, which scale with $We^{-1/3}$, as shown in Eq. (3.27) and (3.35). This discrepancy from predicted values may be seen

in Fig. 3.15, where Ren's basis nozzles are over-predicted at higher Weber numbers (corresponding to larger drop diameters). This $We^{-1/6}$ scaling is not seen in the current measurements, but this is likely because the current measurements were taken at larger Reynolds numbers as both orifice size and operating pressure were larger than Ren's small basis nozzle measurements.

Despite this discrepancy in scaling, the new drop diameter scaling laws appear to accurately predict historical data. This agreement suggests that the scaling laws developed for the axisymmetric configuration may also be applied to standard nozzles.

3.3.0.4 Drop Velocity

The predictions and experimental measurements of drop velocity are compared in Fig. 3.16. The average error is approximately 3%. The model does appear to slightly over-predict sheet velocity at higher pressures. This discrepancy may have occurred because the model does not account for drag on the sheet after the it leaves the deflector, but before atomization occurs. Work by Ibrahim et al. [47] provides equations for fluid sheet trajectories that could be used to improve predictions. However, because the error is so small with the simpler deflector-based sheet thickening factor, β (calculated with Eq. (2.4)), these refinements have not been made in the current work.

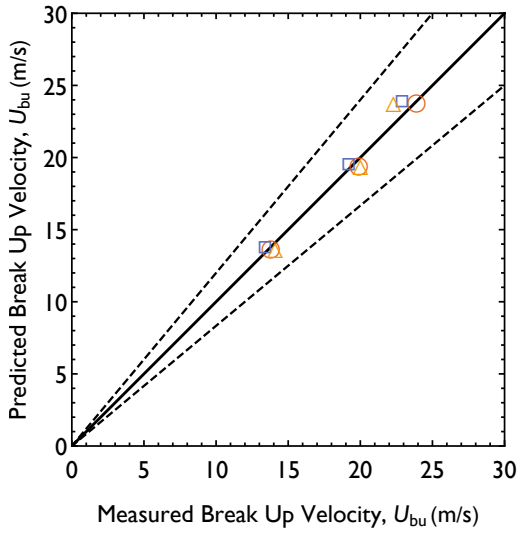

Figure 3.16: A comparison of measured and predicted drop velocity, U_{bu}, for the basis nozzle (red circles), axisymmetric tine (blue squares), and axisymmetric slot (yellow triangles), each determined at three pressures (1, 2 and 3 bar).

3.4 Summary

In this chapter linear instability theory scaling laws were developed and used to predict the atomization phase of the the Deflection Atomization Dispersion (DAD) framework. In this portion of the work the major contributions consisted of:

1. the development of a novel statistical description of the initial sprinkler spray based on a drop distribution function approach [16] harmonizing models and measurements;

2. the development of a linear instability model for sprinkler sheet atomization based on work by Ren [14], refined to predict newly identified initial spray

characteristics based on local sheet characteristics, such as those predicted by the boundary integral method (BIM) model described in Chapter 2;

3. and the identification of the importance of spread angle, θ_{sp}, in predicting initial spray volume flux as well as the significance of the statistical distribution of the critical wave amplitude, f_0, first identified by Wu et al. [45].

The predictions of the model presented above display remarkable agreement with experimental measurements of the initial spray characteristics from two axisymmetric sprinklers, with less than 10% error for every initial spray characteristic. Additionally, the scaling law atomization model shows great promise for the general prediction of initial sprinkler spray characteristics, accurately predicting historically measured drop size as shown in Fig. 3.15.

An important insight gained by the new scaling law analysis is the importance of the critical wave amplitude, f_0. The critical wave amplitude is the non-dimensional amplitude that instabilities in the sheet must reach before atomization. Previous work by Dombrowski et al. [38] established the significance of this amplitude and suggested that it should always have a value of approximately 12. More recent analysis by Ren [4] suggests that this critical amplitude might take on a range of values, and his experiments demonstrated that it is in fact configuration dependent.

The current analysis shows that this critical amplitude is not a fixed value, but rather a distribution. The critical wave amplitude appears to take the form of

a normal distribution, defined by a mean value, f_0, and a standard deviation, σ_{f0}. This critical wave amplitude distribution predicts the mean drop size and breakup radius, as well as the distribution width of drop size and breakup radius. Further, the variance in breakup radius is responsible for the spatial distribution of volume flux. As a result, with the scaling laws outlined above, all initial spray characteristics can be determined with knowledge of only the sheet velocity, sheet thickness, and the mean and standard deviation of the critical wave amplitude.

An unfortunate caveat to the above result, is that there does not currently appear to be a way to determine the critical wave amplitude from first principles. In this work the critical wave amplitude distribution was calculated based on measured break up radii per Eqs. (3.26) and (3.28). Because spray characteristics are so strongly dependent on this critical wave amplitude, it is difficult to predict a spray completely a priori. As a result, the critical wave amplitude must be measured. All measured critical wave amplitudes in the present work and work by Ren take on similar values, $7 < f_0 < 15$, but their variance is enough that an assumed value introduces significant error into a priori spray predictions.

Several assumptions are made in the modeling of the atomization of the spray. First, the spray is assumed to originate entirely from the thin fluid sheets emanating from the deflector. This assumption appears to hold for the axisymmetric sprinklers studied in this design, but may not be applicable for other designs. These sheets are

assumed to undergo flapping aerodynamic instabilities and then atomize first into ligaments and into drops. Investigation by Ren et al. [14] shows that most typical fire sprinklers follow this atomization pattern, but more laminar flows could result in different characteristic breakup mechanisms. Additionally, drops are all assumed to initialize on the breakup surface at the sheet velocity. Further investigation into this assumption is necessary, however initial results suggest it accurately captures the observed physical processes.

The predictions made by the scaling law atomization model outlined above are in a form suitable to incorporate into a Lagrangian particle tracking dispersion model. The development of this dispersion model is the focus of Chapter 4.

Chapter 4: Dispersion

4.1 Introduction

The dispersion model is the last component of the Deflection Atomization Dispersion (DAD) framework for sprinkler spray prediction shown in Fig. 1.5. The goal of the dispersion model presented in this chapter is to predict the far-field spray based on initial spray characteristics, as shown in Tab. 4.1. The sheet characteristics predicted by the deflection model (described in Chapter 2) inform the atomization model (described in Chapter 3), which in turn predicts the characteristics of the initial spray (volume flux, breakup radius, drop size, and drop velocity) that disperses throughout the protected space.

In this chapter, these initial spray characteristics are used as inputs in a Lagrangian particle tracking model of dispersion developed in FireFOAM and applied to the axisymmetric sprinklers described in Sec. 1.3. The resulting dispersed spray consists of a set of N Lagrangian particles, $N\{x_i, y_i, z_i, u_i, v_i, w_i, d_i, W_i\}$, all with unique locations (x_i, y_i, z_i), velocities (u_i, v_i, w_i), diameters (d_i), and particle weighting fac-

Table 4.1: Dispersion model inputs, parameters, and outputs

Model inputs	Volume flux, $\dot{V}''$ Breakup radius, r_{bu} St. dev. of r_{bu}, σ_{rbu} Median diameter, d_{v50} Diameter distribution width, Γ Breakup velocity, U_{bu}
Model parameters	Grid cell size, dx Time step, dt Particle injection rate, $\dot{N}$
Model outputs	Far-field spray, $N\{x_i, y_i, z_i, u_i, v_i, w_i, d_i, W_i\}$

tors (W_i). These particles can be related to integral properties of interest like far-field volume flux, $\dot{V}''(\vec{x})$, and median drop diameter, d_{v50}. The predicted far-field spray for the axisymmetric sprinklers is compared to experimental measurements of the far-field volume flux from the same sprinklers made using the University of Maryland Spatially-Resolved Spray Scanning System (4S) line patternation.

Following atomization, the newly formed fire sprinkler spray flies outward, dispersing through combustion products, plume, flame, and reactants, and interacting with surfaces. The purpose of this spray is to suppress a fire. To simulate this suppression, and thus better implement fire protection strategies, fire protection engineers and researchers are increasingly turning to high-fidelity computational fluid dynamics (CFD) fire models, such as FireFOAM.

FireFOAM [9] is based on OpenFOAM, a free, open-source, general purpose, CFD software. OpenFOAM is an object-oriented, C++-based, second order accurate,

finite-volume solver with implicit time integration and massively parallel computing capability. FireFOAM is a large eddy simulation (LES) fire dynamics solver capable of treating gas phase turbulence and combustion [48]. In addition to the main gas phase CFD solver, FireFOAM is packaged with numerous sub-models in the form of object libraries, treating pyrolysis, turbulence, combustion, radiation, soot, wall boundary layers, surface water films, and Lagrangian particle tracking.

In FireFOAM, the sprinkler spray is represented by Lagrangian particles in an Eulerian-Lagrangian (EL) approach. In the EL approach, the continuous phase (i.e., the gas phase, including combustion products, plume, flame, and reactants) is represented as an evolving Eulerian field, while the dispersed phase (i.e., the sprinkler spray) is modeled using Lagrangian particle tracking [10]. In these models, Lagrangian particles are injected into the modeled domain. Particle motion is determined by solving the Lagrangian equations of motion and interaction while the Eulerian continuous phase is handled through a variety of sub-models (e.g., heat transfer, drop evaporation, turbulent dispersion, etc.).

Drop evolution by Lagrangian particle tracking is well developed and a number of works have used Lagrangian particles to simulate fire sprinkler sprays. Alpert [49] used a Lagrangian particle treatment to simulate the interaction between fire sprinkler sprays and a fire plume, predicting spray penetration and cooling. Later work by Nam [50] simulated a similar configuration, but with higher fidelity gas phase and

particle models. In both of these works, Lagrangian particles of a fixed diameter are injected along a limited number of trajectories. In fact, the assumption that drops are injected from finite nodes is used as recently as 2014 in FireFOAM spray simulations conducted by Wang et al. [15].

This nodal, limited trajectory assumption, however, does not accurately reflect the behavior of the sprinkler spray. It is well known that CFD sprinkler spray predictions are highly sensitive to the input spray characteristics [51, 52]. This is a problem not merely for sprinkler sprays, but also for fuel injection in gas turbine and diesel sprays and even solid particle flows [53–55]. When limited trajectories and limited drop sizes are used, far-field spray resolution is in turn limited and gaps in the predicted spray arise [10].

Limited spray resolution can also lead to inaccurate predictions of gas phase velocity, which impacts predictions of spray penetration and can have effects on spray trajectory. Work by Boivin et al. [55] on a turbulent flow with solid particles emphasized the importance of effective two-way coupling in Lagrangian-Eulerian simulations. Importantly, simulations of a spray laden turbulent jet by Alemeida et al. [56] noted that the most accurate spray models tested were those that incorporated both particle size distributions and stochastic particle injection. The importance of this gas phase coupling has long been a focus in the CFD modeling of fuel injection sprays but has not been well addressed by fire sprinkler spray injection models. This

is, in part, because fire sprinkler sprays are less strongly coupled to the gas phase owing to their large average particle diameter and consequent long particle relaxation time. Despite this, fire sprinkler sprays are sufficiently coupled to the gas phase to necessitate accurate modeling of the spray induced flow.

To accurately capture the sprinkler spray a statistical approach to representing the spray should be used [10]. The true sprinkler spray is stochastic and thus the location of all drops within the spray cannot be known explicitly. Section 3.2.1.1 introduces a method that characterizes the near-field fire sprinkler spray by a drop distribution function. This drop distribution function describes the complex spatio-stochastic characteristics of the sprinkler spray and relates them to experimentally obtainable initial spray characteristics, including the break-up radius, near-field volume flux, drop size, and velocity.

The stochastic nature of the spray makes it impossible to precisely simulate every drop [16]. Instead, the initial spray is specified by a drop distribution function statistically describing the spray. Lagrangian particles may be generated and injected stochastically at a specified rate, effectively statistically sampling the drop distribution function and accurately representing the statistics of the initial spray. These Lagrangian particles then evolve as surrogates for the spray, interacting with the fire, fire induced flow, and the surfaces.

In this chapter, a novel algorithm for injection of the initial spray in FireFOAM

is developed. This spray injection algorithm, `DetailedSprinklerInjectionTwo`, is based on the statistical treatment developed in Sec. 3.2.1.1. In the algorithm, the initial spray is specified using spatially varying volume flux, mean and standard deviation of the breakup radius, median drop diameter, drop diameter distribution width, and initial drop velocity. Lagrangian particles are injected stochastically at a specified rate, effectively statistically sampling the drop distribution function and accurately representing the initial spray. This model represents an improvement on other recent models by Wang et al. [15]. Guidance on resolution requirements for Lagrangian particle tracking in FireFOAM are also provided. FireFOAM simulations for the first time were then used to predict the quiescent dispersion of the axisymmetric sprinklers. These predictions are compared to predictions of induced airflow and far-field spray characteristics predicted by the baseline injection model used in Ref. [15] and further compared to measurements of far-field volumetric flux of the same axisymmetric sprinklers using the University of Maryland Spatially-Resolved Spray Scanning System (4S).

4.2 Methods

4.2.1 Modeling

The goal of a dispersion model is to take the characteristics of the initial spray produced by a sprinkler (volume flux, breakup radius, drop size, and velocity) and accurately represent the far-field spray for the purpose of CFD fire protection simulations. In FireFOAM, the particular CFD fire model used in this study, the fire sprinkler spray is represented by Lagrangian particles which disperse through an Eulerian gas phase.

The sprinkler spray may be described analytically by the drop distribution function, Eq. (3.2), and evolves according to the spray equation, Eq. (3.3), as detailed in Sec. 3.2.1.1. The spray equation completely describes the evolution of the spray; however, its solution as an evolving Eulerian field is unwieldy, thus necessitating its indirect solution using representative Lagrangian particles [10]. This approach is the basis of the Eulerian-Lagrangian (EL) description in the popular KIVA code, primarily used in internal combustion engine models, and provides a theoretical basis for the spray dispersion models used in popular CFD fire models [57].

The stochastic nature of the spray makes it impossible to precisely simulate every drop [16]. Instead, Lagrangian particles that reflect the statistical characteristics of the spray are chosen. To capture measured characteristics, the volume flow cumu-

lative distribution function, $F_V(\theta, \phi, d)$, as defined in Eq. (3.17), is sampled. Every phase space coordinate, (θ, ϕ, d), corresponds to a unique value of the volume flow cumulative distribution function, F_V, between 0 and 1.

Because F_V is strictly increasing and continuous, an inverse distribution function or quantile function, G_V, may be defined as

$$G_V(p) = (F_V)^{-1}(\theta, \psi, d), \tag{4.1}$$

where p spans 0 to 1 and each value of p corresponds to a unique value of θ, ψ, and d. No analytic solution is available for the volume flow cumulative distribution function, F_V, and so numerical methods must be used to calculate its inverse, G_V [16].

To initialize N_p Lagrangian particles, N_p values of p are selected randomly between 0 and 1. Each p is used with the numerical solution to Eq. (4.1) to determine the particle's angular location, θ and ψ, and drop size, d. This numerical particle is then initialized at the breakup radius $r_{bu}(\theta, \psi)$ from the sprinkler head with the breakup velocity $U_{bu}(\theta, \psi, d)$. Each phase space location will be sampled with a frequency proportional to its volume flow, and thus each Lagrangian particle chosen in this manner must carry an equal volume of water. To conserve volume at each time step, a particle weighting factor, W, corresponding to the number of physical drops contained in each Lagrangian particle is given by

$$W = \frac{\dot{V}/\dot{N}}{\pi d^3/6}, \tag{4.2}$$

where the drops are assumed to be spherical.

In this way, Lagrangian particles are preferentially injected at the locations in phase space corresponding to the fraction of the total spray volume flow they carry. This method may be used with any particle injection rate, $\dot{N}$. Limited computational resources make it impractical to simulate the motion of every drop in the sprinkler spray, but improved accuracy is seen with increasing particle injection rate, $\dot{N}$. This is because the selection of particles amounts to statistical sampling of the specified mean characteristics of the spray, represented by F_V. The standard error of the sampled mean from the true mean is proportional to $1/\sqrt{N}$ for normal distributions, and is thus a reasonable approximation for error introduced by the representation of a spray by limited Lagrangian particles [16, 52]. Further guidance on how particle injection rate impacts simulation accuracy is found in the discussion of resolution later in this section.

4.2.1.1 Novel Spray Injection Method

The above statistics-based method for injecting sprinkler spray has been implemented in FireFOAM as `DetailedSprinklerInjectionTwo`. This model allows for any number of sprinklers to be specified within a FireFOAM Lagrangian particle

tracking file. Each sprinkler is given a specific location, orientation, and operating pressure, which are specified in the sprinkler input file. Additionally, each sprinkler input file specifies a particle injection rate and a file containing spray characteristics. Examples of sprinkler input file and spray characteristic input file can be found in Appendix A and B, respectively.

The specified spray characteristics file serves as a lookup table for specified initial sprinkler spray characteristics across elevation and azimuthal angles. At each angular location the user must specify the initial spray volume flux, $\dot{V}''$, mean breakup radius, r_{bu}, standard deviation of breakup radius, σ_{rbu}, median drop size, d_{v50}, drop size distribution width, Γ, and drop velocity, U_{bu}. These spray characteristics reflect the initial spray characteristics predicted in Chapter 3, and can be specified either from atomization model predictions or initial spray measurements.

During sprinkler simulations, N Lagrangian particles are generated each second, evenly divided among each numerical time step, dt. Each Lagrangian particle carries a fixed volume and is created at a random angular location selected probabilistically based on specified volume flow. The total volume flow carried by all particles is given by the specified operating pressure and K-factor. Each particle is then assigned a random breakup radius based on a normal distribution and specified local mean and standard deviations of the breakup radii. A drop size is selected at random from a log-normal/Rosin-Rammler distribution with specified local drop size parameters.

Lastly, each particle is assigned a velocity directed radially away from the sprinkler with the specified local velocity magnitude. A two dimensional visualization of this injection method can be seen in Fig. 4.1. A three dimensional visualization of the same injection scan be seen in Fig. 4.2, a larger version of Fig. 3.6 (b).

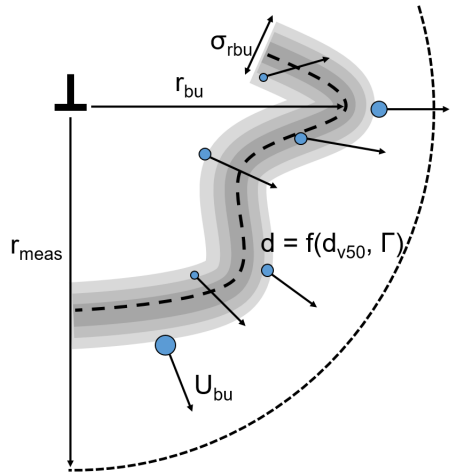

Figure 4.1: `DetailedSprinklerInjectionTwo` injects $\dot{N}$ Lagrangian particles each second, with individual particles properties probabilistically chosen based on the drop distribution function. Each particle is injected at a random angular location at a random radius from the sprinkler governed by the probability distribution, r_{bu}. Each particle is assigned a velocity magintude, U_{bu}, a velocity direction corresponding to angular location, and a diameter, d, selected at random from a log-normal/Rosin-Rammler distribution.

The use of detailed spatially resolved spray characteristics was introduced by Ren et al. [7], who developed spatially resolved maps for volume flux ($\dot{V}''$), median drop diameter (d_{v50}), and diameter distribution width, (Γ), specified and injected on a measurement surface. No provision was included in Ren's modeling approach to generate local velocity distributions or to predict a local drop size/velocity correlation. These deficiencies are noted in Ref. [15] where a novel spray injection model based

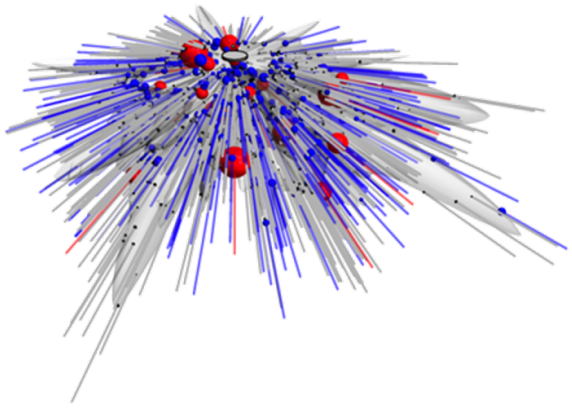

Figure 4.2: Effective sheet breakup surface; red $d > 1.5$mm, blue $0.5 < d < 1.5$mm, and white $d < 0.5$mm; rays are scaled with velocity.

on work by Ren et al. is used to simulate sprinkler suppression of a rack storage fire in FireFOAM. In Wang's work the empirical correlations for volume flux, droplet diameter distribution, and velocity are calculated from experimental data and fitted to functions of elevation angle, with varying coefficients for each azimuthal angle. In the model used in Ref. [15], drops are again specified on a measurement surface, rather than a breakup surface, with drops being injected uniformly from a finite number of nodes at each time step.

Our new model is an improvement on these previous models in four respects. First, the new model shifts the empirical boundary from the measurement surface to

the breakup surface, at r_{bu} [16]. As a result, this new model can capture the drop size/velocity correlation discussed by Ren et al. [7] and Wang et al. [15]. Second, this change allows the initial acceleration of the gas phase induced by sprinkler injection to be captured, adding model fidelity. Third, the injection model allows injection to take place on a continuous surface, instead of on nodes. This removes errors introduced by the unnecessary discretization of spray injection, and captures more of the natural stochastic behavior of the spray. Lastly, rather than injecting uniformly across all locations, in the new model drops are injected at random locations weighted by the local volume flux. This has the result that very few Lagrangian particles are injected at areas of low local volume flux and many drops are injected at areas of high volume flux, reflecting the behavior of the actual sprinkler spray.

After their injection in FireFOAM by the spray injection model, each Lagrangian particle evolves by a Lagrangian particle tracking method. Lagrangian particle tracking calculates the position and state vector (mass, momentum and energy) of individual droplets. The particles injected are subject to the same physics as a real sprinkler spray: gravity, drag, collision, evaporation, heat transfer, and turbulence. Each of these operations is handled by various FireFOAM sub-models. For the purposes of modeling a sprinkler spray, only gravity, drag, and evaporation are treated, while the remaining forces may be neglected due to minimal impact.

The new model was used to good effect in Link et al. [17]. In this work, this

spray injection model was used to simulate two D3 type spray nozzles opposed by an air jet. The initial spray was specified based on detailed spray measurements made in the 4S system [58]. The predicted far-field spray was compared to detailed optical measurements of the spray from the two nozzles within the air jet. Modeled results showed strong agreement with experimental results throughout the jet (15%), with particularly good agreement in areas with high spray volume flux.

After their injection in FireFOAM by `DetailedSprinklerInjectionTwo`, each Lagrangian particle evolves by a Lagrangian particle tracking method. Lagrangian particle tracking follows a particle then computes its state vector, including variables such as its position over time, conserving mass, momentum, and energy. The particles injected are subject to the same forces as a real sprinkler spray: gravity, drag, collision, evaporation, heat transfer, and turbulence. Each of these operations is handled by various FireFOAM submodels. For the purposes of modeling a sprinkler spray, only gravity, drag, and evaporation are treated, and the remaining changes are neglected due to minimal impact. Details on the Lagrangian particle tracking model in FireFOAM can be found in Appendix C.

4.2.1.2 Resolution

Resolution is of critical importance to CFD modeling, but little attention has been given to the resolution requirements for simulating sprinkler sprays. The following section introduces a framework developed to assess resolution requirements for

CFD simulations of sprinkler sprays.

The literature presents some guidance as to the basis of resolution requirements for CFD fire models [48, 51], but the additional complexities introduced by a Lagrangian particle simulation of the fire sprinkler spray have received less attention. The introduction of a spray introduces additional length scales and time scales that must be resolved, and the approximation of a polydispersed spray by finite Lagrangian particles introduces further numerical errors.

To accurately predict spray dispersion the motion of the spray along with the spray's interaction with the gas phase must be resolved. To do this, the smallest length scales and the fastest motions must be resolved and a representative set of Lagrangian particles must be provided in every volume of interest. A user may control numerical resolution by adjusting the grid cell size, dx, the time step, dt, and the particle injection rate, $\dot{N}$. As resolution increases, numerical error decreases, but computational expense increases. An intelligent choice of resolution is necessary to reduce numerical error to acceptable levels without unduly increasing computational expense.

Despite this, most work on simulating the sprinkler spray gives only cursory mention on the impact of spray on grid resolution requirements or guidance as to particle injection rate. Wang et al. [15], presented a detailed simulation of spray injection in FireFOAM, and carefully treated resolution requirements, but does not

directly account for the spray within these requirements. This deficiency is noted in the work. Iannutoni et. al. [59] conducted simulations of water mist injection in OpenFOAM with a varying particle injection rates between $\dot{N} = 50,000$ to $500,000$ particles per second, but does not provide explicit guidance as to how these injection rates should be chosen. The Fire Dynamics Simulator (FDS) User Guide [51] provides guidance on resolution in fire models with Lagrangian particles, detailing a "particle CFL" number and noting the importance of particle injection rate, but does not provide explicit scaling. In this section, guidance is given on choosing the relevant length and time scales in CFD simulations of sprays with Lagrangian particles based on a particle CFL number and guidance on choosing a particle injection rate is given based on statistical arguments outlined by Myers [16].

Space and time may be related by velocity. In the absence of spray, this connection is typically recognized by the Courant or CFL number [48]. To specify spatial and temporal discretization, the smallest characteristic length scale of interest, x_c, is identified and resolved such that the ratio of grid cell size, dx, to length scale, $dx/x_x << 1$. The maximum expected velocity, U_c, is then identified, and the time step, dt, specified such that $U_c\ dt/dx << 1$.

A similar method is applied in simulations with sprays, but both length scale, x_c, and velocity, U_c, may arise in either the continuous phase gas or the dispersed phase spray. Fig. 4.3 shows the variety of length scales that can be found in the

interaction of a plume and sprinkler spray. In addition to the typical gas phase length scales (such as plume diameter, D_{plume}, or height, H), there are also dispersed phase length scales. One example of this is a drop relaxation distance, given as the product of drop velocity, U_{spray}, and drop relaxation time, t_d. These smaller length scales are of some interest, as are turbulent length scale, L_{turb}, or drop diameters, d, but can likely be neglected as unimportant in most spray simulations. Additional length scales could be introduced by the desire to resolve spray volume flux in small areas distant from the sprinkler for evaluation of suppression potential or adequacy of the level of protection..

Simulation accuracy centers on the resolution of all objects of interest. As a result, numerical resolution requirements may be stated in relation to the smallest characteristic length scale and time scale of interest, as these provide the strictest resolution requirements. A simple procedure may be followed to identify these scales and specify resolution:

1. Select the smallest length scale of interest, x_c. This length scale may come from the gas phase (e.g., a plume diameter or height), or the dispersed phase (e.g., a drop relaxation distance).

2. Identify the largest velocity of interest, U_c. This velocity may also come from the gas phase, e.g. a plume velocity, or from the dispersed phase, e.g. an initial drop velocity. This velocity will not necessarily come from the same phase as

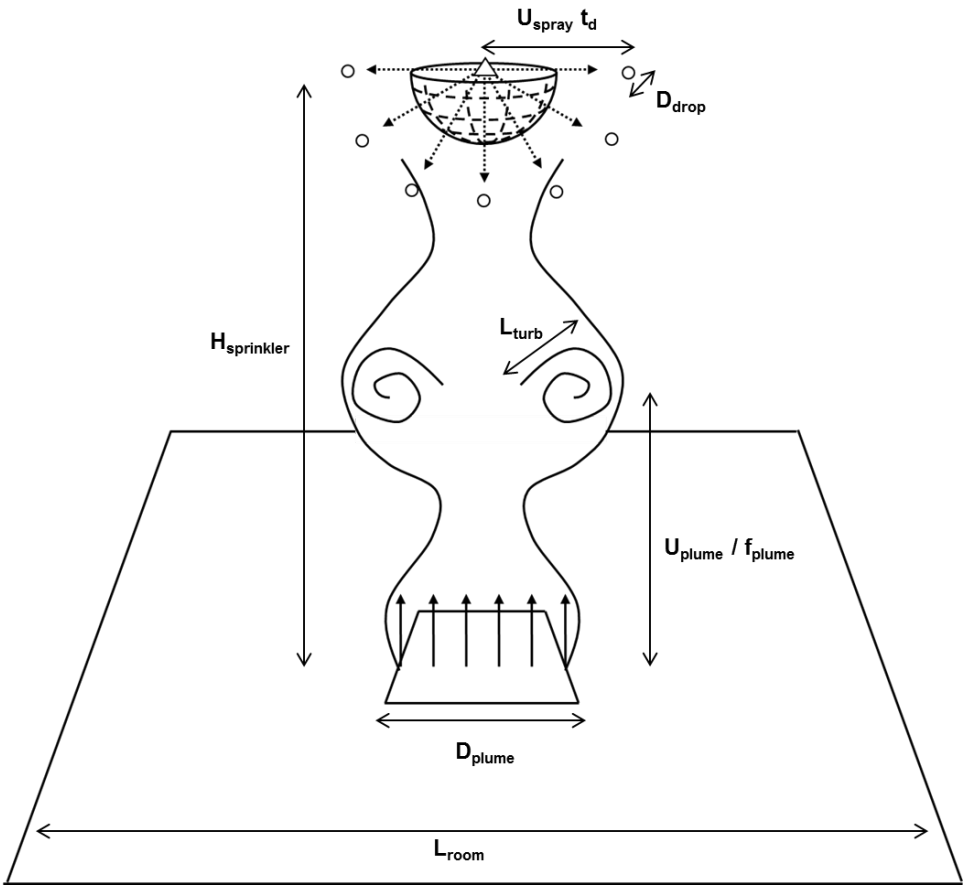

Figure 4.3: A variety of length scales of interest are found in the interaction of a sprinkler spray and a fire induced flow.

the length scale. This is because accurate simulation necessitates the modeling of not only the gas phase and the dispersed phase, but also the interaction of the two.

3. Calculate the smallest time scale of interest, t_c, by relating it to the characteristic length and velocity by $t_c = x_c/U_c$.

4. Specify grid cell size such that $dx/x_c << 1$. For a Eulerian numerical solution

scheme (not to be confused with the Eulerian description of the gas phase), global error will be first-order accurate with dx.

5. Specify time step such that $dt/t_c << 1$. For a Eulerian numerical solution scheme, global error will be first-order accurate with dt. This time step may need to be further reduced to fulfill the stability requirements represented by the Courant number.

6. Inject Lagrangian particles such that the particles injected per time of interest per volume of interest is much larger than one. In other words,

$$\frac{\dot{N}\ t_c}{V_{spray}/x_c^3} >> 1,$$

where $\dot{N}$ is particle injection rate and V_{spray} is the total volume where the spray may be expected to exist. Here the smallest volume of interest is defined as the cube of the length scale of interest, x_c. The total number of volumes of interest are defined as the total volume divided by the characteristic volume of interest. This is such that a diverse and representative sample of the polydispersed spray will be injected into each volume of interest during each time of interest. Each Lagrangian particle may represent drops of only one size and velocity. Because the spray at any given location consists of drops of a variety of sizes and velocities, many Lagrangian particles must be present to approximate the non-linear

spray interactions. Because this Lagrangian particle injection is equivalent to a statistical sampling of the true spray characteristics, global error will behave in the same way as a statistical standard error, and scale as $1/\sqrt{N}$.

In this way grid cell size, dx, the time step, dt, and the particle injection rate, $\dot{N}$, may be selected. The order of accuracy with respect to grid cell size, dx, and the time step, dt, will vary with solution scheme, but in all cases these must be significantly smaller than the length scale and time scale of interest.

This procedure for finding the appropriate resolution parameters is similar to that used in typical CFD models. In a typical CFD fire model the smallest length scale and time scale of interest are identified within the gas phase. The grid cell and time step are then set with special care taken that the CFL number requirement for measurement stability is met [51]. In simulations involving particles, the procedure above may be followed, which explicitly accounts for particle induced length and time scales as well as particle injection rate.

To demonstrate the above procedure the resolution was tested on the 3 bar basis nozzle case, as it was the most restrictive. For this case smallest length scale may be approximated as $x_c = 1.5$ m (the distance from the sprinkler to the collectors) and the smallest time scale as $t_c = 0.1$ s (the time for the fastest drop to reach the floor), and the volume of the domain where spray is expected is approximately 50 m^3.

Following a grid convergence study, a well resolved case was run with resolution

parameters were set at $dx = 0.1$ m, $dt = 0.002$ s, and $\dot{N} = 1,000,000$ particles per second for all simulations. From this reference base case, an exploration of the impact of resolution was conducted. In each simulation, a single resolution parameter was made progressively more coarse, decreasing resolution, while the other parameters remained fixed. Error was assessed for each case by taking the average normalized deviation from the well resolved base case.

Figure 4.4 shows the error induced by spatial resolution compared to the well resolved base case. Three test cases are represented by red circles while the dashed line shows predicted first order scaling. The model error can be seen to closely hold to the predicted first order scaling. The well-resolved base case has a spatial resolution of $dx/x_c = 0.067$, suggesting an error induced by spatial resolution of approximately 6%.

Figure 4.5 shows the error induced by temporal resolution compared to the well resolved base case. Three test cases are represented by red circles while the dashed line shows predicted first order scaling. The model error can be seen to closely hold to the predicted first order scaling. The well-resolved base case has a temporal resolution of $dt/t_c = 0.02$, suggesting an error induced by spatial resolution of approximately 2%.

Figure 4.6 shows the error induced by particle resolution compared to the well resolved base case. Three test cases are represented by red circles while the dashed

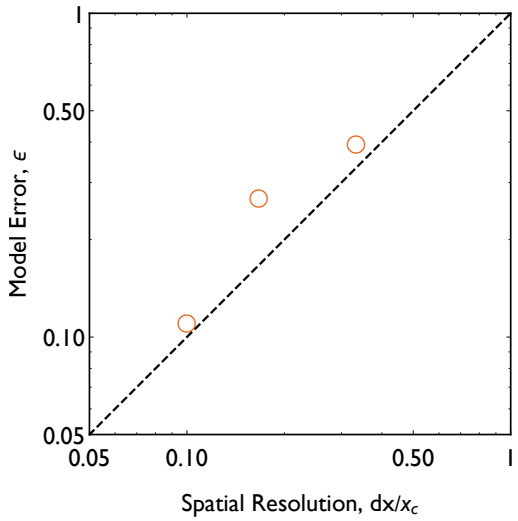

Figure 4.4: Modeling error induced by spatial resolution compared to a well resolved base case. Three test cases are represented by red circles while the dashed line shows predicted first order scaling.

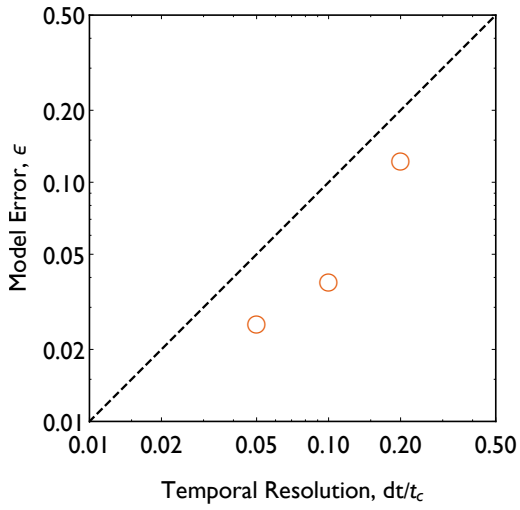

Figure 4.5: Modeling error induced by temporal resolution compared to a well resolved base case. Three test cases are represented by red circles while the dashed line shows predicted first order scaling.

line shows predicted $1/\sqrt{\dot{N}}$ scaling. The model error can be seen to closely hold to the predicted statistical scaling. The well-resolved base case has a particle resolution of $\dot{N}\ t_c/V_{spray}\ x_c^3 = 6,667$, suggesting an error induced by spatial resolution of approximately 1%.

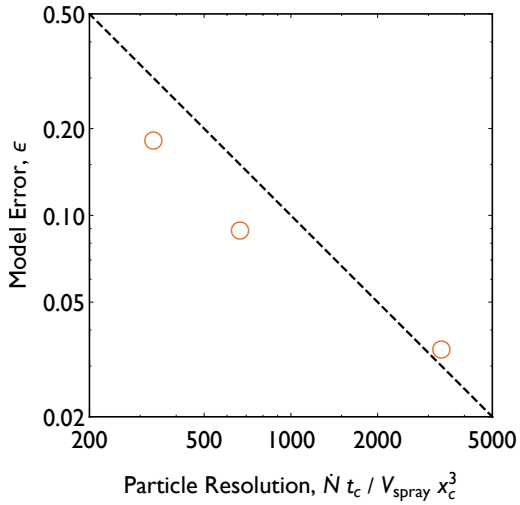

Figure 4.6: Modeling error induced by particle resolution compared to a well resolved base case. Three test cases are represented by red circles while the dashed line shows predicted first order scaling.

In all cases there is some deviation from the predicted scaling. While the error introduced by resolution can be anticipated, the results do not always reliably deviate. Further, some errors, for example particle error, can be offset in steady state cases by extended simulation times. The resolution parameters described in the above section are not necessarily exact representations of the resolution necessary for simulations, but are instead intended to be used to facilitate engineering judgment, in conjunction with engineering insights as to the vital physical scales in any given simulation.

4.2.1.3 FireFOAM Simulations

In total, six well-resolved simulations were conducted in FireFOAM to simulate spray dispersion of the two axisymmetric sprinklers at operating pressures of 1, 2, and 3 bar. In each simulation, the axisymmetric sprinkler sprayed water into a quiescent domain for 60 seconds. Far-field volume flux was measured 1.5 m below the sprinkler, with collection bins located from 0 to 5.5 m radially from the sprinkler head, spaced 0.1 m on center. Each simulation was conducted in a 6 m x 1 m x 2 m computational domain, with $dx = 0.05$ m, $dt = 0.002$ s, and $\dot{N} = 1,000,000$ particles per second set for all simulations, following a grid convergence study.

The spray characteristics used in spray initialization are from predictions of the atomization model, and can be found in Tab. 3.2. The spray was injected using `DetailedSprinklerInjectionTwo`. The evaporation model was disabled during these simulations because the cool, high humidity environment of the University of Maryland spray lab allows for only minimal spray evaporation. Additional simulations were run with a less detailed baseline model corresponding to the model used in Ref. [15]. In these additional simulations all other parameters were held constant.

4.2.2 Experiments

Measurements of far-field volume flux were taken along a radial line from the sprinkler center-line in a line patternation method from the experimental sprinklers

described in Sec. 1.3 using the University of Maryland Spatially-resolved Spray Scanning System (4S). Water is supplied to this system by an underground storage tank and pump. Flow rate is regulated with a valve coupled to an electronic controller monitoring the total pressure immediately upstream of each sprinkler.

The collection tubes were arrayed radially away from the sprinkler, and small collection cups with diameter $d = 0.076$ m were placed in each collection tube. A total of 54 collection cups were used for each sprinkler, spaced 0.1 m apart on center and spanning 0 to 5.3 m radially from the sprinkler head. Each collection cup was located 1.5 m below the sprinkler head.

Volume flux measurements below the sprinkler were obtained over a series of tests. At the beginning of each test, all collection cups were covered as the water flow-rate stabilized at the specified steady-state operating pressure. After stabilization, the collection cups were uncovered and collected water for between 3 and 5 minutes, depending on the flow rate. The mass of the water in each cup was then recorded and related to the volume flux experienced at each point. Errors in initial collection cup weight, area, collection time, and pressure were approximately 10% for all data.

4.3 Results

Observation of the distribution of Lagrangian particles shown in Fig. 4.7 (a) and (b) reveals the characteristic umbrella shape of a fire sprinkler spray. Figure 4.7

(a) shows 2000 Lagrangian particles in the FireFOAM simulation of the basis nozzle operating at 1 bar. Particles are shown 25 times their normal diameter d with the largest drops representing $d > 1.5$ mm, the medium drops representing $0.5 < d < 1.5$ mm, and the smallest representing $d < 0.5$ mm. In the basis nozzle, all drops emerge from approximately the same elevation angle traveling at similar velocities. Larger diameter drops can be seen to travel further, while smaller drops travel only shorter distances, staying on the interior of the umbrella.

Figure 4.7 (b) shows particles from the two-stream axisymmetric nozzle. Here only approximately half of the particles are contained in the umbrella, with the remainder existing in the slot-stream cone on the interior of the spray. It can be observed that there are also fewer larger particles in the two-stream axisymmetric nozzle, a consequence of a smaller median drop size, as seen in Tab. 3.3.

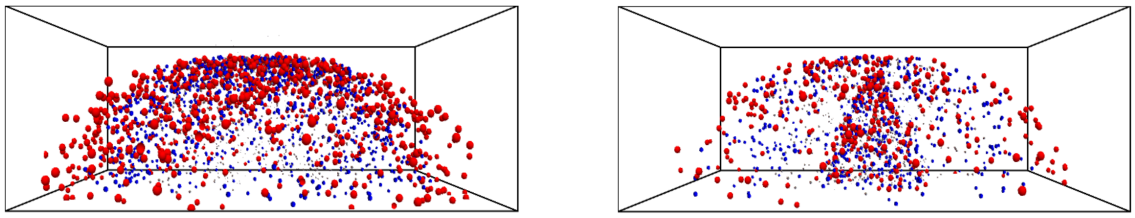

(a) (b)

Figure 4.7: Lagrangian particles generated in FireFOAM for the (a) basis nozzle and (b) two-stream axisymmetric nozzle at 1 bar, shown 25 times normal size and colored by diameter, as in Fig. 4.2.

A more detailed inspection of the spray can be obtained by examining the air flow induced by the spray as well as by looking at the spray characteristics at a hori-

zontal target surface below the sprinkler. Because both sprinklers are axisymmetric, the resulting flow is also axisymmetric, and plots with respect to radius are sufficient to capture all information.

4.3.1 Induced air flow

When the spray is injected into a space, the drops slow due to the influence of air drag. This drag force in turn induces the air in the space to flow. The magnitude of the drag force is positively related to drop velocity. As a result, the initial portion of a sprays trajectory, where the spray is fastest, plays a large role in the overall induced air flow.

In the new model developed in this work, spray is injected at the Bernoulli velocity, or the velocity of the fluid sheets prior to atomization. In the baseline model, the spray is injected at the measured velocity – approximately 70% of the Bernoulli velocity. This slowing all occurs in the approximately 0.2 m between sheet atomization and spray measurement. In the new model this initial slowing and the induced airflow are modeled. In the baseline model, the spray is simply injected as measured and the induced airflow neglected, meaning that 50% of the kinetic energy of the spray is neglected.

Figure 4.8 shows vertical profiles of induced vertical air velocity beneath the sprinkler for the (a) basis nozzle and (b) two-stream axisymmetric nozzle. The lines

represent the sprinklers operated at pressures of 1 bar (solid), 2 bar (dashed) and 3 bar (dotted) for the new model (black lines) and the baseline model (gray lines). Dramatically more airflow is induced with the new model than with the baseline model. In simulations where the spray is combating a fire induced plume, such as the work done in Ref. [17], this additional airflow aids in helping the spray to overcome the plume's substantial momentum.

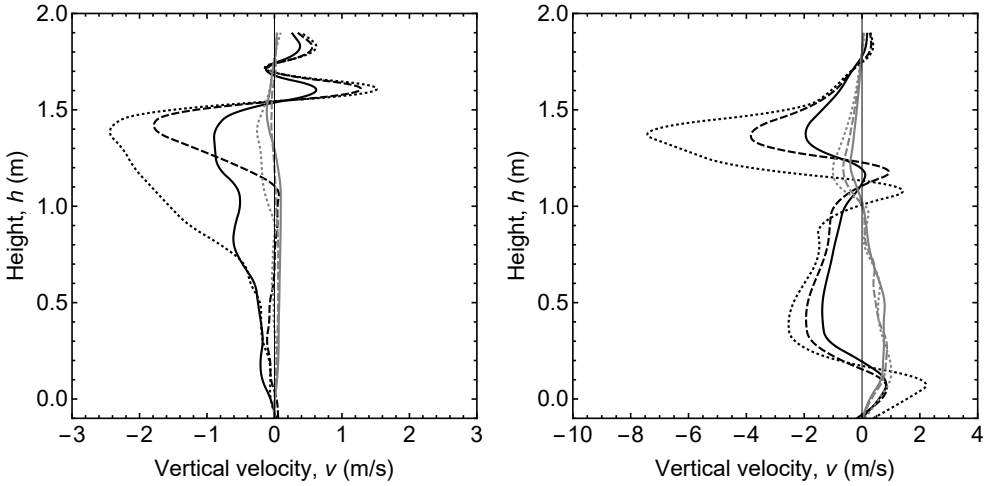

Figure 4.8: Vertical profiles of induced vertical air velocity beneath the sprinkler ($h = 1.5$ m) for the (a) basis nozzle and (b) two-stream axisymmetric nozzle operated at pressures of 1 bar (solid), 2 bar (dashed) and 3 bar (dotted) for the new model (black lines) and the baseline model (gray lines). In all cases, more airflow is induced with the new model, suggesting that the new model could better capture spray-plume interactions.

Figure 4.9 shows horizontal profiles of induced vertical air velocity at sprinkler height ($h = 1.5$ m) for the (a) basis nozzle and (b) two-stream axisymmetric nozzle. The lines are styled for varying sprinkler pressures and injection models as in Fig. 4.8.

These plots show plainly the way in which each model induces airflow. Both models show similar induced air flow at radii greater than $r = 0.4$ m, where the baseline model injects the spray. Inside of this radius the large induced airflow of the initial spray, captured by the new model, is missed by the baseline model.

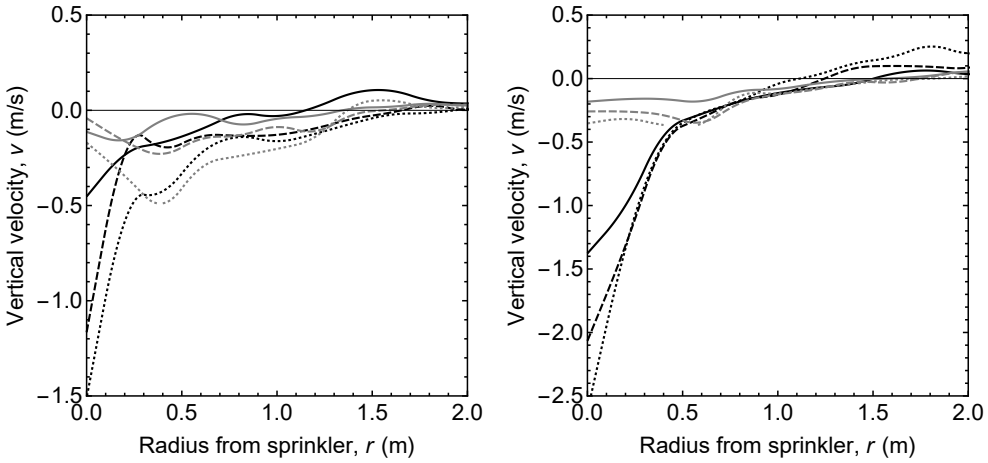

Figure 4.9: Horizontal profiles of induced vertical air velocity radially away from the sprinkler at sprinkler height ($h = 1.5$ m) for the (a) basis nozzle and (b) two-stream axisymmetric nozzle colored and styled as in Fig. 4.8. The new model is capable of capturing the large spike in velocity near the sprinkler which is neglected by the baseline model.

Figure 4.10 shows vertical profiles of vertical air entrainment beneath the sprinkler in a circular column 1 m in diameter for the (a) basis nozzle and (b) two-stream axisymmetric nozzle, colored and styled as in Fig. 4.8. The results are less dramatic than those shown in the individual velocity profiles, because the velocity differences drop dramatically as the spray moves away from the sprinkler. Nonetheless, there is significantly more air entrained with the new model than with the baseline model.

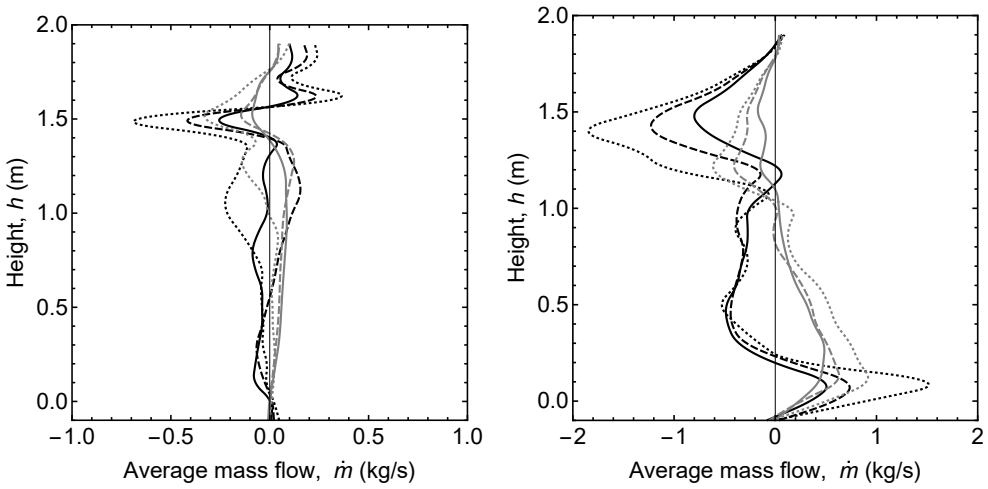

Figure 4.10: Vertical profiles of induced vertical air entrainment beneath the sprinkler ($h = 1.5$ m) in a circular column 1 m in diameter for the (a) basis nozzle and (b) two-stream axisymmetric nozzle, colored and styled as in Fig. 4.8. While the impact on air entrainment averaged over 1 m is less dramatic than immediately beneath the sprinkler, there is still a noticeable difference in induced air flow.

The result of this more accurate coupling between the spray and the gas phase does not only effect the gas phase. The differences in air velocity induced by the spray in turn alters spray trajectories, changing the far-field spray.

4.3.2 Far-field spray characteristics

It is informative to examine the far-field spray predicted by the new model to gain an understanding of the six different sprinkler cases simulated. Figure 4.11 shows the far-field volume flux predicted by FireFOAM from the basis nozzle 1.5 m below the sprinkler at 1 bar (solid line), 2 bar (dashed line), and 3 bar (dotted line).

An integration of the collected volume flux shows that the range of the collectors (extending 5.5 m radially from the nozzle) was insufficient to capture all of the flow from the basis nozzle operating at 2 and 3 bar. At 1, 2, and 3 bar, 91%, 80%, and 70% of the expected volume flux was collected, respectively.

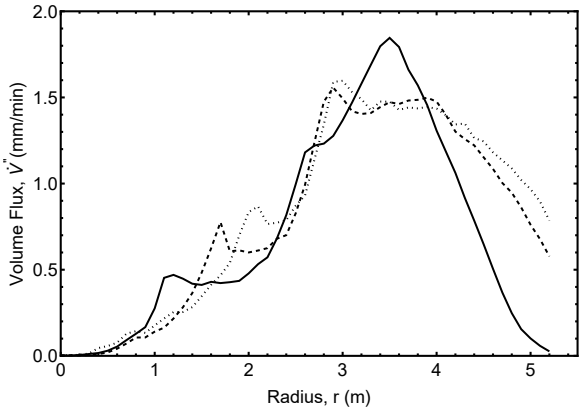

Figure 4.11: Volume flux from the basis nozzle measured 1.5 m below the sprinkler at 1 bar (solid line), 2 bar (dashed line), and 3 bar (dotted line).

Interestingly, the modeled peak volume flux is highest in the lowest pressure case. While more water flows at 2 and 3 bar (1.4 times and 1.7 times, respectively), the throw of the spray is increased, as evidenced by the decreasing fraction of the total volume collected. This increase in spray throw can be attributed to increasing initial spray velocity (also 1.4 times and 1.7 times in the 2 and 3 bar cases), which carries the drops farther.

For a given injection velocity, drop trajectory is entirely determined by drop diameter. This can be clearly seen in Fig. 4.12, which shows distributions of the modeled median drop size, d_{v50}, from the basis nozzle 1.5 m below the sprinkler

with different pressures styled as in Fig. 4.11. For the basis nozzle, volume flux is concentrated near the equator of the injection surface, with volume flux decreasing sharply as it approaches the south pole. For all three pressures, the medium drop size is small ($d_{v50} < 0.2$ mm) near the sprinkler. This is because small drops, regardless of their injection angle or velocity, cannot travel far within the spray, due to drag influences. The drop size (but not the volume flux) is quasi-uniform over the next few meters of spray, but in the far field, it begins to linearly increase. This is a kind of "drop size filtering", which was first suggested by Do [60]. In the far-field spray, drops have self-sorted by drop size, with the larger drops traveling farther.

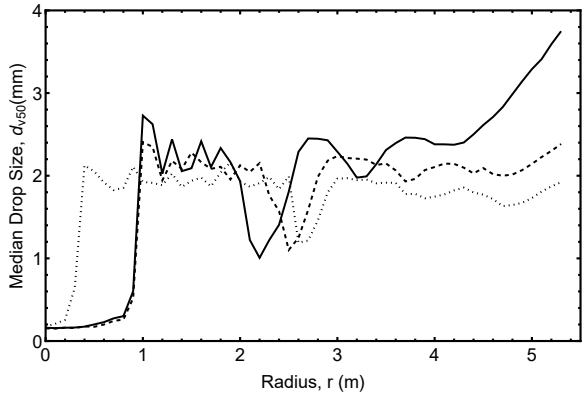

Figure 4.12: Median drop size, d_{v50}, from the basis nozzle measured 1.5 m below the sprinkler at 1 bar (solid line), 2 bar (dashed line), and 3 bar (dotted line), as in Fig. 4.11.

Figure 4.13 shows the modeled volume flux from the two-stream axisymmetric nozzle 1.5 m below the sprinkler at the three operating pressures, as in Fig. 4.11. An integration of the collected volume flux shows that the range of collectors (extending

5.5 m radially from the nozzle) captured almost all of the flow from the two-stream axisymmetric nozzle operating at 2 and 3 bar. At 1, 2, and 3 bar, 100%, 99%, and 98% of the expected volume flux was collected, respectively.

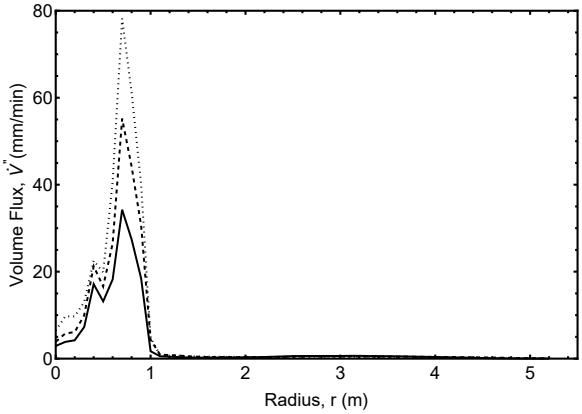

Figure 4.13: Volume flux from the two-stream axisymmetric nozzle measured 1.5 m below the sprinkler at 1 bar (solid line), 2 bar (dashed line), and 3 bar (dotted line).

The volume flow from the slot stream of the two-stream axisymmetric nozzle can be seen in the sharp spike in volume flux in Fig. 4.13, which can be observed between 0 and 1 m radially from the sprinkler head. All three spikes occur at the same radial location, and the peak volume flux in these spikes increases proportionately to the total volume flow through the spikes. The peak volume flux in these cases is nearly 40 times higher than the peak volume flux seen from the basis nozzle in Fig. 4.11, making it difficult to observe the long tail of volume flux from the tine stream. This volume flux can be seen more clearly in Fig. 4.14, which presents the same data as Fig. 4.13, but with the vertical axis rescaled.

The modeled volume flux from the tine stream of the two-stream axisymmetric

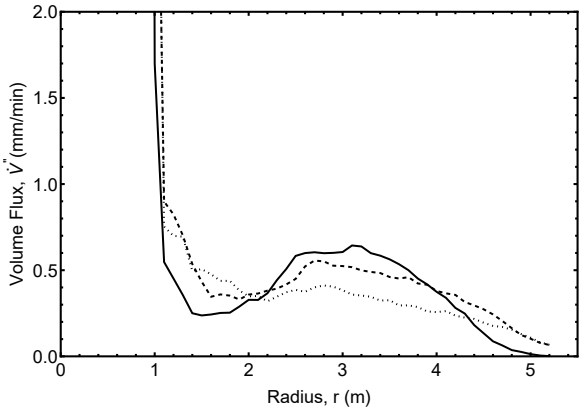

Figure 4.14: Volume flux from the two-stream axisymmetric nozzle measured 1.5 m below the sprinkler at three pressures, as in Fig. 4.11. Rescaled to emphasize volume flux from the tine stream.

nozzle, as seen in Fig. 4.14, closely resembles the volume flux from the basis nozzle, as seen in Fig. 4.13, but shows approximately half of the volume flow. This resemblance is logical, as both the tine stream and the basis nozzle are injected with the same velocity magnitude and direction, and only the thickness of the sheets differs.

Figure 4.15 shows modeled distributions of the median drop size, d_{v50}, from the two-stream axisymmetric nozzle measured 1.5 m below the sprinkler as in Fig. 4.12. In the axisymmetric case, the effect of the aforementioned "drop-size filtering" can be more clearly seen. The first 2 m of the spray is dominated by the slot stream, and has a quasi-uniform drop size. Beyond 2 m, the spray consists entirely of drops from the tine stream. The median drop size can be seen to increase with increasing radius, as only larger drops have trajectories which carry them to the more remote locations. The difference in median drop size at a given location is attributable to differences in

initial velocity, with drops of the same size traveling farther with increased injection velocity.

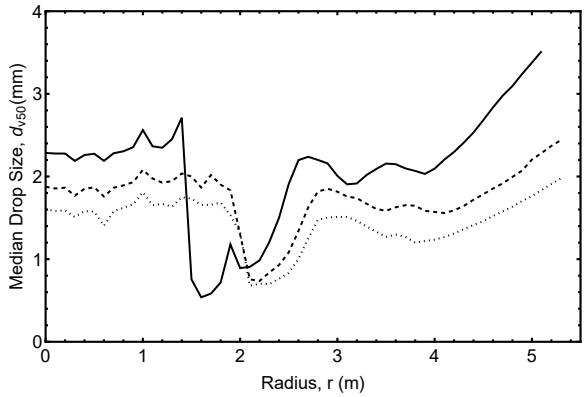

Figure 4.15: Median drop size, d_{v50}, from the two-stream axisymmetric nozzle measured 1.5 m below the sprinkler as in Fig. 4.11.

4.3.3 Comparison to experimental results

The modeled volume flux predictions for the baseline and new models can be compared to experimental measurements made of the same sprinklers at the same operating pressures. While model predictions include far-field drop size distributions, no experimental drop size data was collected and no comparisons can be presented. Similarly, no gas phase measurements were performed and thus no comparisons can be made of induced air velocities. Each sprinkler and each operating pressure are shown separately, so that the comparisons are clear.

Figures 4.16, 4.17, and 4.18 show the far-field volume flux from the basis nozzle operating at pressures of 1, 2, and 3 bar, respectively. Experimental results are

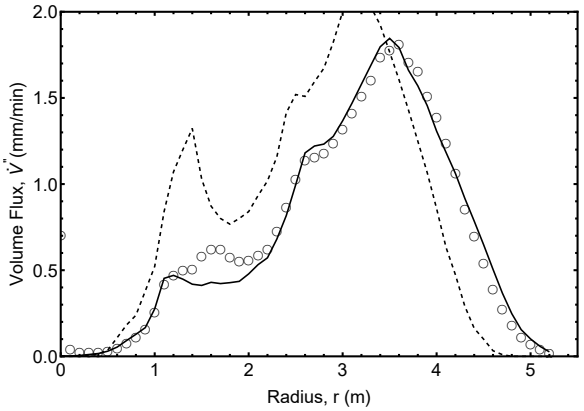

Figure 4.16: Volume flux from the basis nozzle measured 1.5 m below the sprinkler at 1 bar from experimental measurements (black circles) and new model predictions (solid line), and baseline model predictions (dashed line).

shown as black circles, new model results as a solid line and baseline model results as a dashed line. In all cases there is strong agreement between the experimental data and the model, with both the general spatial trends and peak volume flux well captured.

The average difference between the new model and experimental results is 0.07, 0.12, and 0.14 mm/min, for the 1, 2, and 3 bar cases, respectively, or approximately 10% of the peak volume flux. The baseline model performs worse, with average differences of 0.34, 0.23, and 0.23 mm/min, for the 1, 2, and 3 bar cases, respectively, or approximately 25% of the peak volume flux. Notably, the baseline model appears to under-predict spray throw, or the distance traveled by the spray. This difference is likely due to the baseline model failing to capture the initial air velocity which helps to propel the spray further.

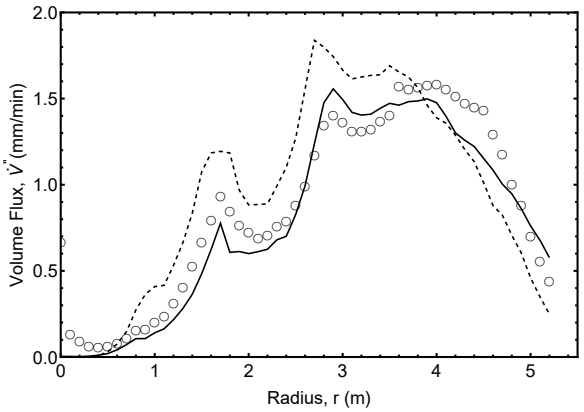

Figure 4.17: Volume flux from the basis nozzle measured 1.5 m below the sprinkler at 2 bar with experimental and model results styled as in Fig. 4.16.

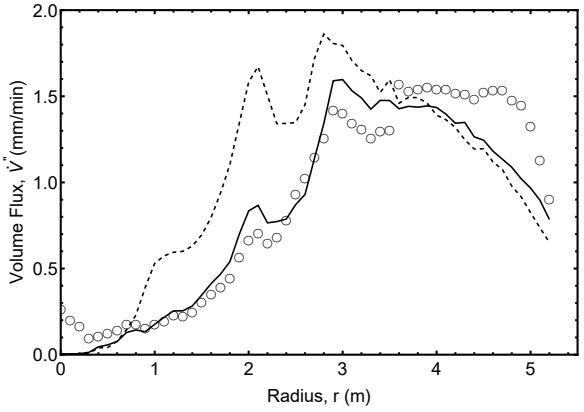

Figure 4.18: Volume flux from the basis nozzle measured 1.5 m below the sprinkler at 3 bar with experimental and model results styled as in Fig. 4.16.

Figures 4.19, 4.21, and 4.23 show the far-field volume flux from the two-stream axisymmetric nozzle operating at pressures of 1, 2, and 3 bar, respectively, while Figs. 4.20, 4.22, and 4.24 show the same results but rescaled for improved visualization of the low volume flux flow from the tine stream. In all cases there is strong agreement between the experimental data and the model, with both the general spatial trends and peak volume flux well captured.

The average difference between the new model and experimental results is higher than in the basis nozzle case, 0.34, 0.82, and 0.86 mm/min for the 1, 2, and 3 bar cases, respectively. Owing to the much higher peak volume flux in these cases, this error is still a small fraction of the peak volume flux, only about 1% of the respective peaks. The average difference between the baseline model and experimental results is, 0.45, 0.87, and 1.47 mm/min for the 1, 2, and 3 bar cases, respectively, higher than with the new model. In these cases both the new and the baseline model equally well capture the volume flux "spike", but the baseline model is less accurate in predicting the volume flux directly beneath the sprinkler. As seen in Fig. 4.15, this portion of the spray consists almost entirely of small drops, which do not travel very far. Because the baseline model does not inject the drops until a radius of $r = 0.4$ m, there is no way for it to accurately capture this flow.

There is strong agreement between the spray dispersion predictions and the measured far-field volume flux for the new spray model. In all cases the new model

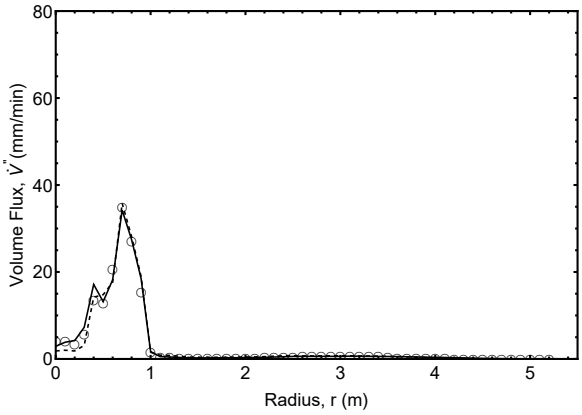

Figure 4.19: Volume flux from the two-stream axisymmetric nozzle measured 1.5 m below the sprinkler at 1 bar with experimental and model results styled as in Fig. 4.16.

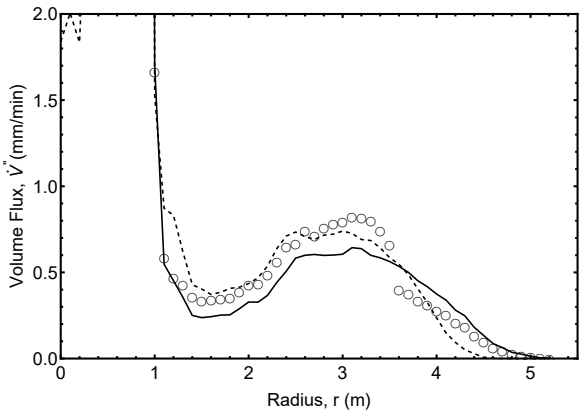

Figure 4.20: Volume flux from the two-stream axisymmetric nozzle measured 1.5 m below the sprinkler at 1 bar with experimental and model results styled as in Fig. 4.16. Rescaled for improved visualization of the flow from the tine stream.

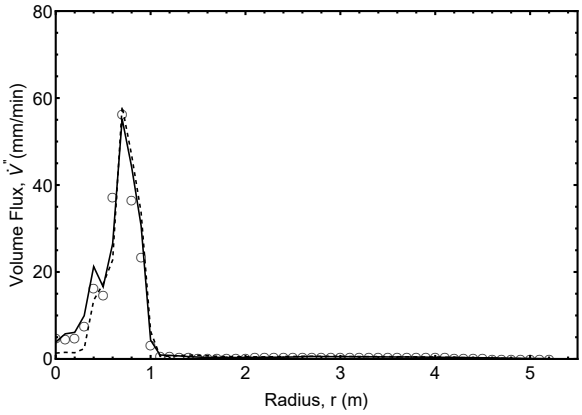

Figure 4.21: Volume flux from the two-stream axisymmetric nozzle measured 1.5 m below the sprinkler at 2 bar with experimental and model results styled as in Fig. 4.16.

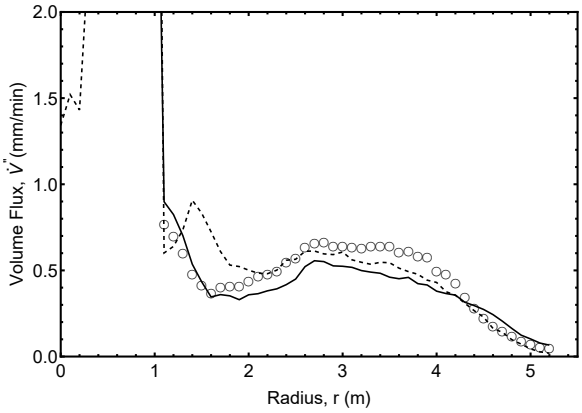

Figure 4.22: Volume flux from the two-stream axisymmetric nozzle measured 1.5 m below the sprinkler at 2 bar with experimental and model results styled as in Fig. 4.16. Rescaled for improved visualization of the flow from the tine stream.

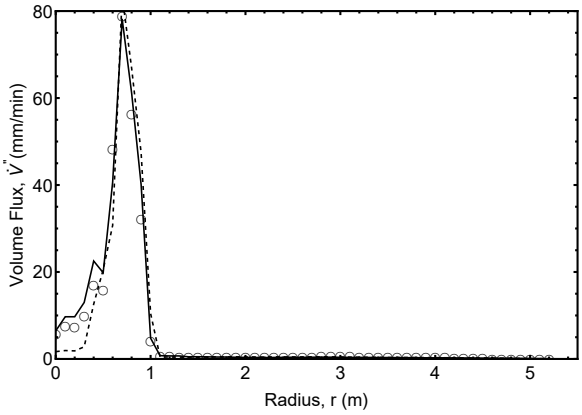

Figure 4.23: Volume flux from the two-stream axisymmetric nozzle measured 1.5 m below the sprinkler at 3 bar with experimental and model results styled as in Fig. 4.16.

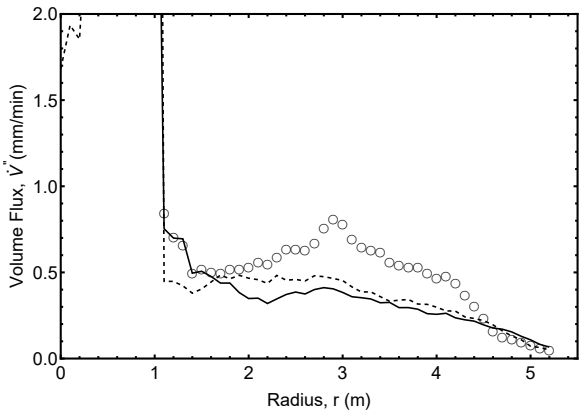

Figure 4.24: Volume flux from the two-stream axisymmetric nozzle measured 1.5 m below the sprinkler at 3 bar with experimental and model results styled as in Fig. 4.16. Rescaled for improved visualization of the flow from the tine stream.

better matches the experimental data than the baseline model. This difference is likely attributable to improved predictions of initial airflow. While there was no experimental measurements made of this airflow, the difference between the induced airflow predictions of the two models are dramatic. The new model, developed in this work, is far more capable of predicting the intense airflow induced locally around a sprinkler head.

The largest fractional deviations of the new model from the measurements occur in regions with low volume flux. This model deficiency is mirrored in experimental and model comparisons of the same injection model in cases by Link et al [17]. In the work by Link, the injection model developed above is used to simulate a spray from a pendant type spray nozzle interacting with a forced air jet. Link notes strong agreement between measurements and model predictions except in areas where volume flux is less than 1 mm/min. This error may be attributable to a statistical effect in the very low volume flux predictions. The number of particles accumulated in this region during the simulation time is very low (less than 100) and these few particles may not be sufficient to accurately represent the flux. Regardless, the current modeling accuracy is promising, and future validation work may help to better clarify the engineering impact of the model deficiency

4.4 Summary

In this chapter a model for the injection of Lagrangian particles into FireFOAM was developed and leveraged to predict the dispersion phase of the Deflection Atomization Dispersion (DAD) framework. In this portion of the work the major contributions consisted of:

1. the development of a novel injection model `DetailedSprinklerInjectionTwo` making use of the initial spray description scheme developed in Chapter 3;

2. and the development of new resolution requirements that provide guidance on the numerical requirements introduced by Lagrangian particle tracking.

The FireFOAM predictions presented show remarkably good agreement with the experimentally measured volume flux for both experimental sprinklers at all three pressures with average error of less than 10% for all cases. The existing framework for Lagrangian particle tracking in FireFOAM has proven to be accurate in predicting spray dispersion. The two chief requirements for CFD sprinkler modeling success are then sufficient numerical resolution and accurate boundary conditions, both of which were addressed in this work.

Several assumptions are made in the modeling of the dispersion of the spray. First, the spray modeled here neglects the possibility of drop to drop interactions. While some drop interactions are possible, due to the dilute nature of the spray they

are unlikely to be significant. Additionally, it is assumed that neither evaporation nor turbulence plays a significant role in the delivered mass flux. These assumptions are reasonable for this particular experimental set up, but would not hold in standard fire calculations.

Chapter 5: Conclusions

In this work, far-field sprays dispersed from two canonical axisymmetric sprinklers were simulated using only sprinkler geometry and injection pressure as inputs. The far-field volume flux error was less than 10% when compared to experimental measurements. This modeling was accomplished within a newly developed Deflection Atomization Dispersion (DAD) framework, outlined in Fig. 1.5. The DAD framework is distinguished by its

1. tightly integrated submodels;
2. robust physics based description of sub-model inputs and outputs;
3. and its harmonization of inputs and outputs with existing high-fidelity spray measurement techniques.

The DAD framework consists of three integrated submodels:

1. a boundary integral method (BIM) deflection sub-model;
2. a linear stability theory atomization sub-model;

3. and a Lagrangian particle injection sub-model for dispersion modeling in FireFOAM.

These sub-models are linked together by connecting inputs and outputs, such that the output of the deflection model is the input for the atomization model and the output for the atomization model is the input for the dispersion model. In this way after inputs for the deflection model are provided, all of the models can be linked together to predict the full fire sprinkler spray.

The primary contributions of this work include:

1. the development of the DAD framework and its submodels;
2. the detailed measurement of two canonical axisymmetric sprinklers at three injection pressures providing validation data for deflection, atomization, and dispersion models;
3. guidance on resolution requirements in computational fluid dynamics (CFD) fire modeling simulations with Lagrangian particles;
4. and the first prediction of the far-field spray entirely from first principles.

The presented work provides a unifying approach, capable of predicting all aspects of sprinkler spray evolution, and has ultimately proven effective in predicting far-field spray properties with high fidelity.

The presented framework also provides a number of opportunities for future work. Expansion of the deflection model can be explored in two directions. The axisymmetric sprinkler as specified can be expanded to explore the impact of a boss (see Fig. 1.2) as well as the impact of angled deflectors, as found in many traditional fire sprinklers. Further expansion away from an axisymmetric design can be made to include the effects of the characteristic azimuthal tine-slot pattern of traditional sprinklers. Recent work in volume of fluid (VOF) modeling has enabled the accurate prediction of volume flux and some spray atomization, but further advances in computing power are necessary to fully resolve atomization. The assumptions of the linear stability atomization model can be further explored through additional experimental observation of the breakup location. Of particular interest is the behavior of ligaments and drops in the moment after breakup, as assumptions about this behavior are core to scaling law assumptions. Lastly, further far-field spray validation data would help to further validate the dispersion model. The current data set only explores quiescent flow over short length scales. Larger canonical experiments that explore the impact of opposed flow, hot plumes, full fires, and ceiling layers would demonstrate the applicability of the model to full fire suppression scenarios.

Appendix A: Sprinkler Properties Input File

```
/*---------------------------------*- C++ -*----------------------------------*/

    sprinkler1
    {
        type detailedSprinklerInjectionTwo;

        lookupTableCoeffs
        {
            tableName       Axi3;
            operatingPressure  43.5; // psig
        }

        SOI             0.0;
        duration        180; //
        parcelsPerSecond 500000;  // per one sprinkler

        positionList
        (
             ( 0  1.6  0 ) //
        );

        direction       ( 0 -1  0);
        armDirection    ( 1  0  0);


        radiusToSprinkler 0.3; // m

        rtiCoeffs
        {
            active                false;
            RTI                   22; // (m s)^0.5  // average of 45-55 (ft s)^0.5
                        C                     0.222; // (m/s)^0.5  // average of
                         ↪  0.7-1.81 (ft / s)^0.5
            initialTemperature    298.15;
            activationTemperature 347.039; // K  // average of 155-165 deg F
```

```
        rtiOutputInterval     200; // output rti data do
         ↪  sprinklerPostProcessing folder every n time steps

                    // to convert RTI from (ft s )^0.5 to (m s)^0.5 square
                     ↪  the value, multiply by 0.3048, and take the sqrt
                    // to convert C from (ft / s)^0.5 to (m/s)^0.5 square the
                     ↪  value, multiply by 0.3048, and take the sqrt
    }



    // begin section not used anywhere
        massTotal       -1;
        parcelBasisType mass;
        massFlowRate 0;
    // end section not used anywhere


}
```

Appendix B: Initial Spray Properties Input File

```
/*--------------------------------*- C++ -*----------------------------------*\
| =========                 |                                                 |
| \\      /  F ield         | OpenFOAM: The Open Source CFD Toolbox           |
|  \\    /   O peration     | Version:  dev                                   |
|   \\  /    A nd           | Web:      www.OpenFOAM.org                      |
|    \\/     M anipulation  |                                                 |
\*---------------------------------------------------------------------------*/
FoamFile
{
    version     2.0;
    format      ascii;
    class       dictionary;
    location    "constant";
    object      sampleSprinklerDict;
}
// * * * * * * * * * * * * * * * * * * * * * * * * * * * * * * * * * * * * * //

sprinkler   Axi1;
kFactor   5.6; // Imperial units [gpm/psi^0.5]
radius     0.4; // m, measurement location (not necessarily injeciton location)
nEle        10;
nAzi        18;

orientation pendent;

pressures
 {
    p14.5
    {
        pressure 14.5; // psig

        phi // azimuthal (deg)
        List<scalar>
        180
                  (
                  0 0 0 0 0 0 0 0 0 0
```

```
20 20 20 20 20 20 20 20 20 20
40 40 40 40 40 40 40 40 40 40
60 60 60 60 60 60 60 60 60 60
80 80 80 80 80 80 80 80 80 80
100 100 100 100 100 100 100 100 100 100
120 120 120 120 120 120 120 120 120 120
140 140 140 140 140 140 140 140 140 140
160 160 160 160 160 160 160 160 160 160
180 180 180 180 180 180 180 180 180 180
200 200 200 200 200 200 200 200 200 200
220 220 220 220 220 220 220 220 220 220
240 240 240 240 240 240 240 240 240 240
260 260 260 260 260 260 260 260 260 260
280 280 280 280 280 280 280 280 280 280
300 300 300 300 300 300 300 300 300 300
320 320 320 320 320 320 320 320 320 320
340 340 340 340 340 340 340 340 340 340
);

theta // elevation (deg)
List<scalar>
180
(
0 10 20 30 40 50 60 70 80 90
0 10 20 30 40 50 60 70 80 90
0 10 20 30 40 50 60 70 80 90
0 10 20 30 40 50 60 70 80 90
0 10 20 30 40 50 60 70 80 90
0 10 20 30 40 50 60 70 80 90
0 10 20 30 40 50 60 70 80 90
0 10 20 30 40 50 60 70 80 90
0 10 20 30 40 50 60 70 80 90
0 10 20 30 40 50 60 70 80 90
0 10 20 30 40 50 60 70 80 90
0 10 20 30 40 50 60 70 80 90
0 10 20 30 40 50 60 70 80 90
0 10 20 30 40 50 60 70 80 90
0 10 20 30 40 50 60 70 80 90
0 10 20 30 40 50 60 70 80 90
0 10 20 30 40 50 60 70 80 90
0 10 20 30 40 50 60 70 80 90
);

volFlux // L/m2/s
List<scalar>
180
(
210.9 66.2 27.5 0.2 0. 7.2 573.5 142.2 12.9 6.2
210.9 66.2 27.5 0.2 0. 7.2 573.5 142.2 12.9 6.2
```

```
210.9 66.2 27.5 0.2 0. 7.2 573.5 142.2 12.9 6.2
210.9 66.2 27.5 0.2 0. 7.2 573.5 142.2 12.9 6.2
210.9 66.2 27.5 0.2 0. 7.2 573.5 142.2 12.9 6.2
210.9 66.2 27.5 0.2 0. 7.2 573.5 142.2 12.9 6.2
210.9 66.2 27.5 0.2 0. 7.2 573.5 142.2 12.9 6.2
210.9 66.2 27.5 0.2 0. 7.2 573.5 142.2 12.9 6.2
210.9 66.2 27.5 0.2 0. 7.2 573.5 142.2 12.9 6.2
210.9 66.2 27.5 0.2 0. 7.2 573.5 142.2 12.9 6.2
210.9 66.2 27.5 0.2 0. 7.2 573.5 142.2 12.9 6.2
210.9 66.2 27.5 0.2 0. 7.2 573.5 142.2 12.9 6.2
210.9 66.2 27.5 0.2 0. 7.2 573.5 142.2 12.9 6.2
210.9 66.2 27.5 0.2 0. 7.2 573.5 142.2 12.9 6.2
210.9 66.2 27.5 0.2 0. 7.2 573.5 142.2 12.9 6.2
210.9 66.2 27.5 0.2 0. 7.2 573.5 142.2 12.9 6.2
210.9 66.2 27.5 0.2 0. 7.2 573.5 142.2 12.9 6.2
210.9 66.2 27.5 0.2 0. 7.2 573.5 142.2 12.9 6.2
210.9 66.2 27.5 0.2 0. 7.2 573.5 142.2 12.9 6.2
210.9 66.2 27.5 0.2 0. 7.2 573.5 142.2 12.9 6.2
210.9 66.2 27.5 0.2 0. 7.2 573.5 142.2 12.9 6.2
210.9 66.2 27.5 0.2 0. 7.2 573.5 142.2 12.9 6.2
)
;

dv50 // mm
List<scalar>
180
(
1.46 1.46 1.46 1.46 1.46 1.46 1.46 1.46 1.46 1.46
1.46 1.46 1.46 1.46 1.46 1.46 1.46 1.46 1.46 1.46
1.46 1.46 1.46 1.46 1.46 1.46 1.46 1.46 1.46 1.46
1.46 1.46 1.46 1.46 1.46 1.46 1.46 1.46 1.46 1.46
1.46 1.46 1.46 1.46 1.46 1.46 1.46 1.46 1.46 1.46
1.46 1.46 1.46 1.46 1.46 1.46 1.46 1.46 1.46 1.46
1.46 1.46 1.46 1.46 1.46 1.46 1.46 1.46 1.46 1.46
1.46 1.46 1.46 1.46 1.46 1.46 1.46 1.46 1.46 1.46
1.46 1.46 1.46 1.46 1.46 1.46 1.46 1.46 1.46 1.46
1.46 1.46 1.46 1.46 1.46 1.46 1.46 1.46 1.46 1.46
1.46 1.46 1.46 1.46 1.46 1.46 1.46 1.46 1.46 1.46
1.46 1.46 1.46 1.46 1.46 1.46 1.46 1.46 1.46 1.46
1.46 1.46 1.46 1.46 1.46 1.46 1.46 1.46 1.46 1.46
1.46 1.46 1.46 1.46 1.46 1.46 1.46 1.46 1.46 1.46
1.46 1.46 1.46 1.46 1.46 1.46 1.46 1.46 1.46 1.46
1.46 1.46 1.46 1.46 1.46 1.46 1.46 1.46 1.46 1.46
1.46 1.46 1.46 1.46 1.46 1.46 1.46 1.46 1.46 1.46
1.46 1.46 1.46 1.46 1.46 1.46 1.46 1.46 1.46 1.46
1.46 1.46 1.46 1.46 1.46 1.46 1.46 1.46 1.46 1.46
)
;

velMag // m/s
List<scalar>
180
(
13.8 13.8 13.8 13.8 13.8 13.8 13.8 13.8 13.8 13.8
13.8 13.8 13.8 13.8 13.8 13.8 13.8 13.8 13.8 13.8
13.8 13.8 13.8 13.8 13.8 13.8 13.8 13.8 13.8 13.8
```

```
13.8 13.8 13.8 13.8 13.8 13.8 13.8 13.8 13.8 13.8
13.8 13.8 13.8 13.8 13.8 13.8 13.8 13.8 13.8 13.8
13.8 13.8 13.8 13.8 13.8 13.8 13.8 13.8 13.8 13.8
13.8 13.8 13.8 13.8 13.8 13.8 13.8 13.8 13.8 13.8
13.8 13.8 13.8 13.8 13.8 13.8 13.8 13.8 13.8 13.8
13.8 13.8 13.8 13.8 13.8 13.8 13.8 13.8 13.8 13.8
13.8 13.8 13.8 13.8 13.8 13.8 13.8 13.8 13.8 13.8
13.8 13.8 13.8 13.8 13.8 13.8 13.8 13.8 13.8 13.8
13.8 13.8 13.8 13.8 13.8 13.8 13.8 13.8 13.8 13.8
13.8 13.8 13.8 13.8 13.8 13.8 13.8 13.8 13.8 13.8
13.8 13.8 13.8 13.8 13.8 13.8 13.8 13.8 13.8 13.8
13.8 13.8 13.8 13.8 13.8 13.8 13.8 13.8 13.8 13.8
13.8 13.8 13.8 13.8 13.8 13.8 13.8 13.8 13.8 13.8
13.8 13.8 13.8 13.8 13.8 13.8 13.8 13.8 13.8 13.8
13.8 13.8 13.8 13.8 13.8 13.8 13.8 13.8 13.8 13.8
13.8 13.8 13.8 13.8 13.8 13.8 13.8 13.8 13.8 13.8
)
;

gamma //
List<scalar>
180
(
2.40 2.40 2.40 2.40 2.40 2.40 2.40 2.40 2.40 2.40
2.40 2.40 2.40 2.40 2.40 2.40 2.40 2.40 2.40 2.40
2.40 2.40 2.40 2.40 2.40 2.40 2.40 2.40 2.40 2.40
2.40 2.40 2.40 2.40 2.40 2.40 2.40 2.40 2.40 2.40
2.40 2.40 2.40 2.40 2.40 2.40 2.40 2.40 2.40 2.40
2.40 2.40 2.40 2.40 2.40 2.40 2.40 2.40 2.40 2.40
2.40 2.40 2.40 2.40 2.40 2.40 2.40 2.40 2.40 2.40
2.40 2.40 2.40 2.40 2.40 2.40 2.40 2.40 2.40 2.40
2.40 2.40 2.40 2.40 2.40 2.40 2.40 2.40 2.40 2.40
2.40 2.40 2.40 2.40 2.40 2.40 2.40 2.40 2.40 2.40
2.40 2.40 2.40 2.40 2.40 2.40 2.40 2.40 2.40 2.40
2.40 2.40 2.40 2.40 2.40 2.40 2.40 2.40 2.40 2.40
2.40 2.40 2.40 2.40 2.40 2.40 2.40 2.40 2.40 2.40
2.40 2.40 2.40 2.40 2.40 2.40 2.40 2.40 2.40 2.40
2.40 2.40 2.40 2.40 2.40 2.40 2.40 2.40 2.40 2.40
2.40 2.40 2.40 2.40 2.40 2.40 2.40 2.40 2.40 2.40
)
;

rbu // m
List<scalar>
180
(
0.147 0.147 0.147 0.147 0.147 0.147 0.147 0.147 0.147 0.147
0.147 0.147 0.147 0.147 0.147 0.147 0.147 0.147 0.147 0.147
0.147 0.147 0.147 0.147 0.147 0.147 0.147 0.147 0.147 0.147
0.147 0.147 0.147 0.147 0.147 0.147 0.147 0.147 0.147 0.147
```

```
                0.147 0.147 0.147 0.147 0.147 0.147 0.147 0.147 0.147 0.147
                0.147 0.147 0.147 0.147 0.147 0.147 0.147 0.147 0.147 0.147
                0.147 0.147 0.147 0.147 0.147 0.147 0.147 0.147 0.147 0.147
                0.147 0.147 0.147 0.147 0.147 0.147 0.147 0.147 0.147 0.147
                0.147 0.147 0.147 0.147 0.147 0.147 0.147 0.147 0.147 0.147
                0.147 0.147 0.147 0.147 0.147 0.147 0.147 0.147 0.147 0.147
                0.147 0.147 0.147 0.147 0.147 0.147 0.147 0.147 0.147 0.147
                0.147 0.147 0.147 0.147 0.147 0.147 0.147 0.147 0.147 0.147
                0.147 0.147 0.147 0.147 0.147 0.147 0.147 0.147 0.147 0.147
                0.147 0.147 0.147 0.147 0.147 0.147 0.147 0.147 0.147 0.147
                0.147 0.147 0.147 0.147 0.147 0.147 0.147 0.147 0.147 0.147
                0.147 0.147 0.147 0.147 0.147 0.147 0.147 0.147 0.147 0.147
                0.147 0.147 0.147 0.147 0.147 0.147 0.147 0.147 0.147 0.147
                0.147 0.147 0.147 0.147 0.147 0.147 0.147 0.147 0.147 0.147
                );

        sigRbu // m
        List<scalar>
        180
                (
                0.061 0.061 0.061 0.061 0.061 0.061 0.061 0.061 0.061 0.061
                0.061 0.061 0.061 0.061 0.061 0.061 0.061 0.061 0.061 0.061
                0.061 0.061 0.061 0.061 0.061 0.061 0.061 0.061 0.061 0.061
                0.061 0.061 0.061 0.061 0.061 0.061 0.061 0.061 0.061 0.061
                0.061 0.061 0.061 0.061 0.061 0.061 0.061 0.061 0.061 0.061
                0.061 0.061 0.061 0.061 0.061 0.061 0.061 0.061 0.061 0.061
                0.061 0.061 0.061 0.061 0.061 0.061 0.061 0.061 0.061 0.061
                0.061 0.061 0.061 0.061 0.061 0.061 0.061 0.061 0.061 0.061
                0.061 0.061 0.061 0.061 0.061 0.061 0.061 0.061 0.061 0.061
                0.061 0.061 0.061 0.061 0.061 0.061 0.061 0.061 0.061 0.061
                0.061 0.061 0.061 0.061 0.061 0.061 0.061 0.061 0.061 0.061
                0.061 0.061 0.061 0.061 0.061 0.061 0.061 0.061 0.061 0.061
                0.061 0.061 0.061 0.061 0.061 0.061 0.061 0.061 0.061 0.061
                0.061 0.061 0.061 0.061 0.061 0.061 0.061 0.061 0.061 0.061
                0.061 0.061 0.061 0.061 0.061 0.061 0.061 0.061 0.061 0.061
                0.061 0.061 0.061 0.061 0.061 0.061 0.061 0.061 0.061 0.061
                0.061 0.061 0.061 0.061 0.061 0.061 0.061 0.061 0.061 0.061
                0.061 0.061 0.061 0.061 0.061 0.061 0.061 0.061 0.061 0.061
                0.061 0.061 0.061 0.061 0.061 0.061 0.061 0.061 0.061 0.061
                0.061 0.061 0.061 0.061 0.061 0.061 0.061 0.061 0.061 0.061
                0.061 0.061 0.061 0.061 0.061 0.061 0.061 0.061 0.061 0.061
                0.061 0.061 0.061 0.061 0.061 0.061 0.061 0.061 0.061 0.061
                0.061 0.061 0.061 0.061 0.061 0.061 0.061 0.061 0.061 0.061
                0.061 0.061 0.061 0.061 0.061 0.061 0.061 0.061 0.061 0.061
                0.061 0.061 0.061 0.061 0.061 0.061 0.061 0.061 0.061 0.061
                );

         }
}
```

Appendix C: Lagrangian Particle Tracking in FireFOAM

After their injection in FireFOAM each Lagrangian particle evolves by a Lagrangian particle tracking method. Lagrangian particle tracking follows a particle then computes its state vector, including variables such as its position over time, conserving mass, momentum, and energy. The particles injected are subject to the same forces as a real sprinkler spray: gravity, drag, collision, evaporation, heat transfer, and turbulence. Each of these operations is handled by various FireFOAM submodels. For the purposes of modeling a sprinkler spray, only gravity, drag, and evaporation are treated, and the remaining changes are neglected due to minimal impact.

The most fundamental operation of particle tracking is recording the location of the particles. This includes the "What-Cell-Am-I-In" functionality [61]. Particles have an explicit Lagrangian position but must also be located in a Eulerian cell. This is necessary for the particles to interact with the surrounding gas phase, which is represented as a Eulerian field. There are two algorithms for tracking particles, which Karrholm refers to as the Lose-Find and the Face-To-Face algorithms [54].

The Lose-Find algorithm proceeds according to the following sequence:

1. Update the particle characteristics using the various sub-models
2. Move the particle based on the particle velocity and the current simulation time step
3. Locate the particle in a specific Eulerian cell
4. Add mass, momentum, and energy to the Eulerian cell the particle is now in through use of the sub-models.

If the time step is small enough to ensure that no particle moves through more than one Eulerian cell, then the Lose-Find algorithm works well. If Eulerian cells are sufficiently small and particle velocity is sufficiently large, the particle can "skip" cells [54]. Therefore, the particle only transfers mass, momentum, and energy to the cell it is in at the end of the time step.

A newer model, Face-to-Face tracking, eliminates this problem. Face-To-Face tracking proceeds according to the following sequence [54]:

1. Move the particle until it reaches a cell boundary or for the entire simulation time step if it remains in the same cell
2. If the particle changes cells, calculate the time it took to move out of the first cell, and update the particle characteristics
3. Add the mass, momentum, and energy change to the Eulerian cell that the particle was in.

4. If the particle still has time left to move, repeat.

Particles tracked by Face-To-Face tracking cannot "skip" cells, which improves the predictions of transfer of mass, momentum, and energy.

The `particleForces` sub-model controls the motion of a Lagrangian particle. This motion is governed by Newton's second law,

$$\frac{\partial \vec{p_i}}{\partial t} = \vec{F_i}, \tag{C.1}$$

where $\vec{p_i}$ is the momentum of a single Lagrangian particle and $\vec{F_i}$ is the force acting on the same particle. The full equation describing force on a particle is the Basset-Boussinesq-Oseen (BBO) equation. The BBO equation contains the effects of particle mass, pressure, Basset force, Magnus effect, Saffman force, and Faxen force [54]. Most of these forces may be neglected for sprinkler spray because they have only minimal impact. The forces of chief importance are the gravitational and spherical drag forces.

When accounting solely for spherical drag and gravity, Eq. (C.1) can be rewritten as

$$\frac{\partial \vec{U_i}}{\partial t} = -\frac{3}{4}\frac{\rho_a}{\rho_w}\frac{1/d_i}{C}_D \left(\vec{U_i} - \vec{U_a}\right) |\vec{U_i} - \vec{U_a}| + \vec{g}, \tag{C.2}$$

where $\vec{U_i}$ is the particle velocity, ρ_a is the gas phase density, ρ_w is the particle density, d_i is the particle diameter, C_D is the drag coefficient, $\vec{U_a}$ is the continuous phase

velocity, and $\vec{g}$ is the gravitational vector [54].

The drag coefficient, C_D, is represented by the piecewise equation

$$C_D = \begin{cases} \frac{24}{Re_i}\left(1 + \frac{Re_i^{2/3}}{6}\right) & Re_i < 1000 \\ 0.424 & Re_i \geq 1000, \end{cases} \tag{C.3}$$

where Re_i is the particle Reynolds number relative to the local gas phase velocity.

Lagrangian particles move according this equation during each computational time step. The gas phase momentum in the local cell is also updated to reflect the particles influence on the gas phase by

$$\frac{\partial \vec{U_a}}{\partial t} = \frac{m_i}{m_a}\frac{3}{4}\frac{\rho_a}{\rho_w}\frac{1/d_i}{C}_D\left(\vec{U_i} - \vec{U_a}\right)|\vec{U_i} - \vec{U_a}|, \tag{C.4}$$

where m_i is the mass of the particle and m_a is the mass of the gas phase cell. Here the change in the gas phase momentum is equal and opposite to the change in the momentum of the particle.

The `phaseChange` model in FireFOAM handles the evaporation of the particle, including both mass transfer and enthalpy transfer. There are three different phase change models implemented in FireFOAM.

- `noPhaseChange`: The default phase change model in which there is no evaporation.

- `liquidEvaporation`: Liquid evaporation model using the ideal gas law assumption.

- `liquidEvaporationBoil`: Similar to liquidEvaporation, but includes a boiling model based on work by Zuo [62].

Both models of evaporation are based on work by Spalding [63].

In the `liquidEvaporation`, model mass transfer is given by

$$\frac{\partial m_i}{\partial t} = d_i \pi Sh_i \rho_a D_{ab} \left(Y_s - Y_\infty\right), \tag{C.5}$$

where d_i is the particle diameter, Sh_i is the particle Sherwood number, given as $Sh = 2 + Re_i^{1/2} Pr_a^{1/3}$, ρ_a is the density of the gas phase, D_{ab} is the binary diffusivity of the particle species into the gas phase, Y_s is the mass fraction of the particle species at the surface of the particle, and Y_∞ is the mass fraction of the particle species in the gas phase. Here the binary diffusivity, D_{ab}, is evaluated at the surface temperature and liquid vapor pressure. The mass fraction at the surface is calculated as a ratio of the saturation pressure of the liquid at surface temperature to the local total pressure.

Recognizing that the mass of the drop may be rewritten in terms of diameter, this equation may be rewritten as the D-Squared Law,

$$\frac{\partial d_i^2}{\partial t} = -\frac{4Sh\ D_{ab}\ \rho_a}{\rho_w} \left(Y_s - Y_\infty\right). \tag{C.6}$$

As the Sherwood number, Sh, is nearly always approximately 2, this result converges to the result given by Fick's law in Crowe [64]. This model is only intended for cases in which there is limited bulk flow (or mass transfer occurs primarily by diffusion) and where the particle is below the boiling temperature. Both of these assumptions are poor for a sprinkler spray interacting with a fire.

The second evaporation model, `liquidEvaporationBoil` is based on work by Zuo and is better suited for sprinkler sprays [62]. Drop evaporation is separated into two processes, "evaporation" and "boiling". If the saturation pressure, as calculated from Clausius-Clapeyron, is less than 99.9% of the gas phase pressure, a drop is considered to be evaporating. Mass transfer is then calculated as

$$\frac{\partial m_i}{\partial t} = d_i \pi Sh_i \rho_a D_{ab} ln\left(1 + B\right), \tag{C.7}$$

where B, is the mass transfer number given by

$$B = \left(X_s - X_\infty\right) / \left(1 - X_s\right). \tag{C.8}$$

Here X_s is the surface molar fraction calculated by Raoult's law as $X_s = (p_s at(T_s))/p$, where $p_s at$ is the saturation pressure, T_s is the temperature of the surface, and p is the gas phase pressure. Converting again to the "D-Squared Law"

$$\frac{\partial d_i^2}{\partial t} = -\frac{4Sh\ D_{ab}\ \rho_a}{\rho_w} ln(1+B). \tag{C.9}$$

For both `liquidEvaporation` and `liquidEvaporationBoil`, the D-Squared Law shows that the square of the drop diameter changes linearly with time in a constant environment.

Bibliography

[1] G. Grant, J. Brenton, and D. Drysdale. Fire suppression by water sprays. *Progress in Energy and Combustion Science*, pages 79–130, 2000.

[2] A. W. Marshall. Unraveling fire suppression sprays. In *Fire Safety Science - Proceedings of the Tenth International Symposium*, pages 61–75. International Association for Fire Safety Science, 2011.

[3] S. Jordan and A. W. Marshall. Spatially-Resolved Spray Measurements and their Implications. *Fire Technology*, 2016.

[4] N. Ren. *Advances in Characterizing Fire Sprinkler Sprays*. Phd thesis, University of Maryland, 2010.

[5] J. Widmann, D. Sheppard, and R. Lueptow. Non-intrusive measurements in fire sprinkler sprays. *Fire Technology*, 2001.

[6] D. Sheppard and R.M. Lueptow. 'Characterization of Fire Sprinkler Sprays using Particle Image Velocimetry. *Atomization and Sprays*, 15(3):341–362, 2005.

[7] N. Ren, H. Baum, and A. W. Marshall. A comprehensive methodology for characterizing sprinkler sprays. *Proceedings of the Combustion Institute*, 33:2547–2554, 2011.

[8] K. McGrattan, S. Hostikka, R. McDermott, , J. Floyd, C. Weinschenk, and K. Overholt. Fire Dynamics Simulator Technical Reference Guide Volume 1: Mathematical Model. Technical report, National Institute of Standards and Technology, Gaithersburg, Maryland, USA.

[9] FM Global, FireFOAM. available at: https://github.com/fireFoam-dev.

[10] S. Subramaniam. Lagrangian – Eulerian methods for multiphase flows. *Progress in Energy and Combustion science*, 39(2-3):215–245, 2012.

[11] X. Zhou, S. P. D'Aniello, and H.Z. Yu. Spray characterization measurements of a pendent fire sprinkler. *Fire Safety Journal*, 54:36–48, 2012.

[12] T. M. Myers, H. Baum, , and A. W. Marshall. A free-surface model of a jet impinging on a sprinkler head. In *Proceedings of the Eleventh International Symposium for Fire Safety Science.*, Christchurch, New Zealand, 2014.

[13] K. Meredith. VOF Modeling of Fire Sprinkler Spray Patternation. In *FM Global Open Source CFD Fire Modeling Workshop*, Norwood, Massachusetts, USA, 2015.

[14] N. Ren and A. W. Marshall. Characterizing the initial spray from large Weber number impinging jets. *International Journal of Multiphase Flow*, 58:205–213, 2014.

[15] Y Wang, Meredith K., X Zhou, P Chatterjee, Y Xin, Chaos M., N Ren, and S Dorofeev. Numerical Simulation of Sprinkler Suppression of Rack Storage Fires. *Fire Safety Science - Proceedings of the Eleventh International Symposium*, 11:1170–1183, 2014.

[16] T. M. Myers and A. W. Marshall. A description of the initial fire sprinkler spray. *Fire Safety Journal*, Vol. 84:pp. 1–7, 2016.

[17] E. Link, T. Myers, A. Trouve, and A. Marshall. Measurements of Spray-Plume Interactions for Model Validation. 2017.

[18] J. M. Prahl and B. Wendt. Discharge distribution performance for an axisymmetric model of a fire sprinkler head. *Fire Saftey Journal*, Vol. 14:pp. 101–111, 1988.

[19] National Fire Protection Association. *Fire Protection Handbook*. 20th edition edition, 2008.

[20] C. W. Hirt and B. D. Nichols. Volume of fluid (vof) method for the dynamics of free boundaries. *Journal of Computational Physics*, Vol. 39:pp. 201–225, 1979.

[21] G. Baker. Bit for free surface flows. In M. H. Wen, editor, *Boundary Element Methods in Engineering and Sciences*, pages 283–323. Imperial College Press, London, 2011.

[22] W. Schach. Umlenkung eines kriesfoermignen fluessigkeitsstrahes an einer eben platte senkrecht zur stroemunsrichtung. *Ing. Arch.*, Vol. 6:pp. 51–59, 1935.

[23] Reich. Deflection of a free liquid jet on a flat plate perpendicular to the floor direction. *VDI Research Journal.*, Vol. 290, 1926.

[24] J H Lienhard. Impingement cooling with free-surface liquid jets, 2006.

[25] J. H. Lienhard. Velocity Coefficients For Free Jets From Sharp-Edged Orifices. *Journal of Fluids Engineering*, Vol. 106:pp. 13–17, 1984.

[26] G. K. Batchelor and A. E. Gill. Analysis of the stability of axisymmetric jets, 1962.

[27] V. Sladek, J. Sladek, and M. Tanaka. Numerical integration of logarithmic and nearly logarithmic singularity in BEMs. *Applied Mathematical Modelling*, 25(11):901–922, 2001.

[28] G. Xie, J. Zhang, X. Qin, and G. Li. New variable transformations for evaluating nearly singular integrals in 2D boundary element method. *Engineering Analysis with Boundary Elements*, 35(6):811–817, 2011.

[29] J.P. Bardhan, M.D. Altman, D. J. Willis, S.M. Lippow, B. Tidor, and J.K. White. Numerical integration techniques for curved-element discretizations of molecule-solvent interfaces. *Journal of Chemical Physics*, 127(1), 2007.

[30] Wolfram Language and System Documentation. Nintegrate integration rules. Technical report.

[31] C. Pozrikidis. *A Practical Guide to Boundary Element Methods*. CRC Press, 2002.

[32] F. Savart. *Ann. Chim. Phys.*, 1931.

[33] Weber. Zum zerfall eines flüssigkeitsstrahles. *angew. Math Mech*, 1931.

[34] W. W. Hagerty and J. F.. Shea. A Study of Stability of Plane Fluid Sheets. *Journal of Applied Physics*, Vol. 22:pp. 509–514, 1955.

[35] Rayleigh. On the Capillary Phenomena of Jets. *Proceedings of the Royal Society of London*, Vol. 29:pp. 71–97, 1879.

[36] N. Dombrowski, D. Hasson, and D.E. Ward. Some Aspect of Liquid Flow through Fan Spray Nozzles. *Chemical Engineering Science*, Vol. 12:pp. 35–50, 1959.

[37] N. Dombrowski and P.C. Hooper. The Effect of Ambient Density on Drop Formation in Sprays. *Chemical Engineering Science*, Vol. 17:pp. 291–305, 1962.

[38] N. Dombrowski and P.C. Hooper. The Aerodynamic Instability and Disintegration of Viscous Liquid Sheets. *Chemical Engineering Science*, Vol. 18:pp. 203–214, 1963.

[39] C. Clanet and E. Villermaux. The life of a smooth liquid sheet. *Journal of Fluid Mechanics*, Vol. 462:pp. 307–340, 2002.

[40] E. Villermaux and C. Clanet. Life of a flapping liquid sheet. *Journal of Fluid Mechanics*, Vol. 462:pp. 341–363, 2002.

[41] F.A. Williams. Spray Combustion and Atomization. *Physics of Fluids*, 1(6):541–545, 1958.

[42] S. Subramaniam. Statistical modeling of sprays using the droplet distribution function. *Physics of Fluids*, 13(3):624–642, 2001.

[43] S. Balachandar. A scaling analysis for point-particle approaches to turbulent multiphase flows. *International Journal of Multiphase Flow*, 35(9):801–810, 2009.

[44] H.Z. Yu. Investigation Of Spray Patterns Of Selected Sprinklers With The Fmrc Drop Size Measuring System. In *Fire Safety Science*, volume 1, pages 1165–1176. International Association for Fire Safety Science, 1986.

[45] Di Wu, Delphine Guillemin, and André W. Marshall. A modeling basis for predicting the initial sprinkler spray. *Fire Safety Journal*, 42(4):283–294, 2007.

[46] G. D. Crapper, N. Dombrowski, and G. a. D. Pyott. Large Amplitude Kelvin-Helmholtz Waves on Thin Liquid Sheets. *Proceedings of the Royal Society A: Mathematical, Physical and Engineering Sciences*, 342(1629):209–224, 1975.

[47] E. Ibrahim and T. R. McKinney. Injection characteristics of non-swirling and swirling annular liquid sheets. *Proceedings of the Institution of Mechanical Engineers, Part C: Journal of Mechanical Engineering Science*, Vol. 220(2):pp. 203–214, February 2006.

[48] S. Vilfayeau. *Large Eddy Simulation of Fire Extinction Phenomena*. Phd thesis, University of Maryland, 2015.

[49] R. Alpert. Numerical Modeling of the Interaction Between Automatic Sprinkler Sprays and Fire Plumes. *Fire Safety Journal*, 9(2):157–163, 1985.

[50] Soonil Nam. Numerical simulation of the penetration capability of sprinkler sprays. 32, 1999.

[51] Kevin McGrattan, Simo Hostikka, Randall McDermott, Jason Floyd, Craig Weinschenk, and Kristopher Overholt. Fire Dynamics Simulator, User's Guide, Sixth Edition. Technical report, NIST, Gaithersburg, Maryland, USA, 2013.

[52] Tarek Beji, Setareh Ebrahim Zadeh, Georgios Maragkos, and Bart Merci. Influence of the particle injection rate, droplet size distribution and volume flux angular distribution on the results and computational time of water spray CFD simulations. *Fire Safety Journal*, (January):1–10, 2017.

[53] H. C. Mongia, R. S. Reynolds, and R. Srinivasan. Multidimensional gas turbine combustion modeling Applications and limitations. *AIAA Journal*, 24(6):890–904, 1986.

[54] F.P. Karrholm. *Numerical Modelling of Diesel Spray Injection , Turbulence Interaction and Combustion*. PhD thesis, Chalmers University of Technology, 2008.

[55] M Boivin, O Simonin, and K D Squires. On the prediction of gas-solid flows wit two-way coupling using large eddy simulation. *Phys. Fluids*, 12(2000), 2000.

[56] Thomas G. Almeida and Farhad A. Jaberi. Large-eddy simulation of a dispersed particle-laden turbulent round jet. *International Journal of Heat and Mass Transfer*, 51(3-4):683–695, 2008.

[57] A. O. Amsden. KIVA-II: A Computer Program for Chemically Reactive Flows with Sprays, Tech. Rep. LA–11560– MS. Technical report, Los Alamos National Laboratory, 1989.

[58] Stephen J Jordan, Noah L Ryder, Juraj Repcik, and Andre W Marshall. Spatially-resolved spray measurements and their implications. *Fire Safety Journal*, 91(February):723–729, 2017.

[59] L. Iannantuoni, D. Ettorre, G. Manzini, and L. Araneo. Validation and Assessment of a Water Mist Multi-hole Nozzle Model for Fire Simulations. *Fire Technology*, 50(3):505–524, 2013.

[60] C. Do. *Stream-Wise Discharge Characteristics of Pendant Sprinkler Sprays*. Master's thesis, University of Maryland, 2009.

[61] N.P. Nordin. *Complex chemistry modeling of diesel spray combustion*. PhD thesis, Chalmers University of Technology, 2001.

[62] B. Zuo, M. Gomes, and C. J. Rutland. Studies of Superheated Fuel Spray Structures and Vaporization in GDI engines. *International Journal of Engine Research*, 1(4):321–336, 2000.

[63] D. B. Spalding and R. W. Bain. *Convective Mass Transfer*, volume 32. 1965.

[64] C. Crowe, M. Sommerfeld, and Y. Tsuji. *Multiphase Flows with Droplets and Particles*. CRC Press, 2011.